Similitudes and sensitivities as contributions to scaling laws in machine acoustics

Ähnlichkeitsanalysen und Sensitivitätsanalysen als Beiträge zu Modellgesetzen in der Maschinenakustik

Vom Fachbereich Maschinenbau an der
Technischen Universität Darmstadt
zur Erlangung des akademischen Grades eines
Doktor-Ingenieurs (Dr.-Ing.)
genehmigte

DISSERTATION

von
Christian Adams, M.Sc.
aus Andernach

1. Gutachter:	Prof. Dr.-Ing. Tobias Melz
2. Gutachter:	Prof. Dr.-Ing. Steffen Marburg
Tag der Einreichung:	21.01.2019
Tag der mündlichen Prüfung:	20.05.2019

Darmstadt 2019

D 17

Similitudes and sensitivities as contributions to scaling laws in machine acoustics
Ähnlichkeitsanalysen und Sensitivitätsanalysen als Beiträge zu Modellgesetzen in der Maschinenakustik

1. Gutachter:	Prof. Dr.-Ing. Tobias Melz
2. Gutachter:	Prof. Dr.-Ing. Steffen Marburg
Tag der Einreichung:	21.01.2019
Tag der mündlichen Prüfung:	20.05.2019

Darmstadt 2019 – D 17

URN: urn:nbn:de:tuda-tuprints-87264
URL: https://tuprints.ulb.tu-darmstadt.de/id/eprint/8726

Das Dokument wird bereitgestellt von tuprints,
E-Publishing-Service der TU Darmstadt
http://tuprints.ulb.tu-darmstadt.de
tuprints@ulb.tu-darmstadt.de

Vorwort

Die vorliegende Dissertation verfasste ich im Rahmen meiner Tätigkeit als wissenschaftlicher Mitarbeiter am Fachgebiet Systemzuverlässigkeit, Adaptronik und Maschinenakustik SAM der Technischen Universität Darmstadt. Meinem Doktorvater, Herrn Prof. Dr.-Ing. Tobias Melz, danke ich herzlich für die Betreuung meiner Promotion. Meine Forschung konnte ich stets nach meinen Interessen gestalten, was mich sowohl fachlich als auch persönlich voran gebracht hat. Herrn Prof. Dr.-Ing. Steffen Marburg von der Technischen Universität München danke ich für das Zweitgutachten sowie für interessante und anregende Gespräche während Konferenzen und darüber hinaus. Weiterhin möchte ich Herrn Dr.-Ing. Joachim Bös sehr herzlich danken. Er hatte für meine Anliegen stets ein offenes Ohr. Die zahlreichen Gespräche mit ihm waren für mich immer eine inspirierende Quelle, um meine Forschung voranzubringen.

Meine Promotion wäre ohne die Unterstützung durch Andere in dieser Form nicht gelungen. An erster Stelle trugen meine Kollegen vom Fachgebiet SAM durch interessante Diskussionen, wertvolle Denkanstöße und eine sehr angenehme Arbeitsatmosphäre zum Gelingen meiner Promotion bei. Die von mir untersuchte Getriebebaureihe wurde von der SEW-EURODRIVE GmbH & Co KG zur Verfügung gestellt. Insbesondere gaben mir Herr Dr.-Ing. Konstantin Völker und Herr Markus Lutz wertvolle Hinweise zur Weiterentwicklung der Modellgesetze im Hinblick auf Baukästen. Herr PD Dr. rer. nat. habil. Jürgen Bär von der Universität der Bundeswehr München hat die Materialparameter (E, μ, ρ) der von mir untersuchten Rechteckplatten gemessen. Dr.-Ing. Joachim Bös, Dr.-Ing. Uwe Niedermayer und Philipp Neubauer gaben mir wertvolle Hinweise zur Verbesserung der vorliegenden Dissertation. Diese Unterstützung schätze ich sehr und bedanke mich dafür sehr herzlich.

Schließlich danke ich meinen Freunden und meiner Familie für ihre beständige Unterstützung. Insbesondere haben meine Eltern Inge und Hans-Werner mich stets ermutigt. Sha Yang (杨莎) danke ich für ihre liebevolle Unterstützung und Nachsicht während einer sehr geschäftigen Zeit.

Darmstadt im Juni 2019 Christian Adams

Abstract

Noise and vibration engineering faces increasing demands of customers such as noise limits or comfort issues and also requires cost-efficient and adaptable design engineering methods due to shorter product life cycles. Taking advantage of similitudes of designs can address these needs by using scaled prototypes in experimental investigations or by designing size ranges and kits. However, a reliable prognosis of noise and vibration of an original design requires scaling laws that transfer the measurement results from the scaled prototype to the original design or from one design to another one within a size range. Similitude analysis lacks efficient and straightforward methods to derive scaling laws, thus, contradicting the demand for cost-efficient design engineering methods. Furthermore, scaling laws are often limited to complete similitude conditions such as equal damping values of the scaled prototype and of the original design or perfect geometrical similitude of a size range, which are hardly fulfilled in practice.

This thesis aims at developing a procedure to straightforwardly derive scaling laws of mechanical structures by combining similitude analysis with sensitivity analysis, which determines the effect of design parameters on the vibration behavior of a mechanical structure. From this, the noise and vibration behavior of mechanical structures can be predicted even if incomplete similitude conditions persist. Similitude analysis and sensitivity analysis methods are first illustrated by potential applications in noise and vibration engineering using a double mass oscillator as a comprehensible example of a mechanical structure. A new scaling method is developed that combines similitude analyses with sensitivity analyses. This allows for deriving scaling laws, which incorporate sensitivities as coefficients. The scaling laws of rectangular plates in complete similitude are directly derived from analytical and finite element calculations for global and local vibration responses such as surface-averaged frequency response functions or vibration velocities at a local receiver point. These scaling laws match those derived from state-of-the-art similitude analysis methods, which verifies the new scaling method. Applying the new scaling method to plate-like structures in complete similitude demonstrates that scaling laws can be straightforwardly derived, whereas state-of-the-art similitude analysis methods would be too time-

consuming. The scaling laws derived from the new scaling method accurately predict the vibration responses of scaled structures using the vibration responses of an original structure, which are obtained from numerical calculations or experimental measurements. The new scaling method even replicates the vibration responses of structures in geometrically incomplete similitude sufficiently well by using another scaled structure, which is in complete similitude to the original structure. In order to assess the accuracy of the scaled vibration responses an error measure is developed and validated in a-posteriori analyses. Finally, a size range of gear boxes in geometrically incomplete similitude demonstrates that the natural frequencies of an entire size range can be predicted with a sufficient accuracy by the new scaling method. The new scaling method can be enhanced towards kits since the natural frequencies of the gear boxes with various lumped masses attached can be replicated sufficiently well.

Zusammenfassung

Einerseits muss die Maschinenakustik in modernen Produktentwicklungsprozessen Kundenanforderungen wie strengeren Akustikgrenzwerten oder steigenden Komfortansprüchen genügen und andererseits müssen die Produktentwicklungsmethoden aufgrund kürzerer Produktlebenszyklen und höherer Produktflexibilität möglichst kosteneffizient und flexibel eingesetzt werden. Diese Anforderungen an die Maschinenakustik können durch Ähnlichkeitsbetrachtungen erfüllt werden, indem Messungen an skalierten Prototypen durchgeführt oder Baureihen und Baukästen entwickelt werden. Allerdings benötigen solche Ähnlichkeitsbetrachtungen Modellgesetze, mit denen die Messergebnisse eines skalierten Prototypen auf die Originalkonstruktion oder von einem Grundentwurf auf die Folgeentwürfe einer Baureihe übertragen werden können. Solche Modellgesetze lassen sich bislang nur mit erhöhtem Aufwand ermitteln, so dass Modellgesetze in der Maschinenakustik heute nur selten angewendet werden oder auf vollständige Ähnlichkeit beschränkt sind. Vollständige Ähnlichkeit, z. B. gleiche Dämpfung des skalierten Prototyps und der Originalkonstruktion oder vollständige geometrische Ähnlichkeit einer Baureihe, lässt sich aufgrund praktischer Randbedingungen in der Regel nicht realisieren.

Ziel dieser Arbeit ist es, eine neue Skalierungsmethode zu entwickeln, mit der akustische Modellgesetze effizient hergeleitet werden können, wobei auch bei unvollständiger Ähnlichkeit eine Abschätzung des akustischen Verhaltens der Originalkonstruktion auf Basis von skalierten Prototypen ermöglicht werden soll. Dazu werden Ähnlichkeitsanalysen mit Sensitivitätsanalysen kombiniert. Am Beispiel eines Zweimassenschwingers wird gezeigt, dass sich beide Methoden komplementär ergänzen können. Die neue Skalierungsmethode verwendet die Sensitivitäten als Koeffizienten für die Modellgesetze, die auf Ähnlichkeitsbetrachtungen basieren. Zunächst wird für vollständig ähnliche Rechteckplatten gezeigt, dass die mit der neuen Skalierungsmethode hergeleiteten Modellgesetze für globale und lokale akustische Zielfunktionen, z. B. oberflächengemittelte Übertragungsfunktionen oder lokale Schwinggeschwindigkeiten, mit denen klassischer Ähnlichkeitsanalysen übereinstimmen, so dass die entwickelte Skalierungsmethode verifiziert werden kann. Darüber hinaus lassen sich mit der entwickelten Skalierungsmethode Modellgesetze plattenähnlicher Struk-

turen herleiten, bei denen klassische Ähnlichkeitsanalysen aufgrund des hohen Aufwands nicht mehr zielführend wären. Mithilfe der Modellgesetze können akustische Zielfunktionen von Rechteckplatten und plattenähnlichen Strukturen, die sowohl aus numerischen Berechnungen als auch aus experimentellen Untersuchungen ermittelt werden, mit hoher Genauigkeit auf skalierte Strukturen übertragen werden, sofern die skalierten Strukturen und die Originalstruktur vollständig ähnlich sind. Globale und lokale akustische Zielfunktionen von geometrisch unvollständig ähnlichen Rechteckplatten können mit für Ingenieursanwendungen ausreichender Genauigkeit auf skalierte Rechteckplatten übertragen werden, indem anstelle der geometrisch unvollständig ähnlichen Rechteckplatte eine weitere, vollständig ähnliche Rechteckplatte für die Skalierung verwendet wird. Um die Genauigkeit der Skalierung zu bewerten, wird eine Bewertungsgröße entwickelt und in a-posteriori-Analysen validiert. Abschließend wird am Beispiel der Skalierung der Eigenfrequenzen einer geometrisch unvollständig ähnlichen Getriebebaureihe gezeigt, dass sich die entwickelte Skalierungsmethode auch auf Probleme in der industriellen Praxis anwenden lässt. Auch können die Eigenfrequenzen der Getriebebaureihe in Abhängigkeit von einer angebrachten Punktmasse skaliert werden, so dass die neue Skalierungsmethode auch im Hinblick auf Baukästen erweitert werden kann.

Contents

1 Introduction

Noise and vibration engineering faces demands of customers such as noise limits or comfort issues. Shorter product life cycles and increased flexibility of machine designs require time-efficient, cost-efficient, and adaptable design engineering methods. These needs are commonly addressed by cost-efficient design engineering methods such as

- designing size ranges and kits [1–3],[1]
- using small-scaled models in experimental investigations [4], or
- taking advantage of synergies across several product development projects.

All three approaches benefit from the fact that the machine designs are similar up to a certain extent. Figure 1.1 illustrates a size range of gear boxes. The gear boxes have a similar design, but their geometrical dimensions are scaled. Instead of analyzing each gear box of the size range, e.g., measuring the vibrations, it is more efficient to analyze only one reference gear box and to scale-up (or scale-down) the analysis results from that reference gear box to the other gear boxes of the size range.

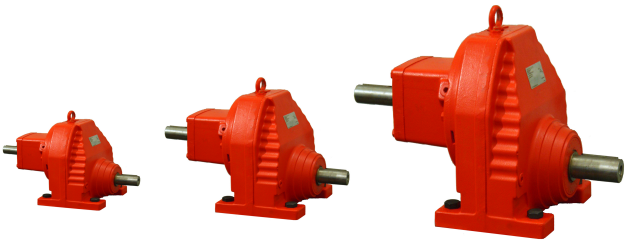

Figure 1.1: example of a size range of gear boxes

[1] [3] is an English summary of the original papers [1, 2] in German language.

Such a scale-up (or scale-down) requires the scaling laws of the gear boxes to be known. The scaling laws can be derived from a *similitude analysis* [4]. However, similitude analysis methods are too time-consuming in practical design engineering and are often limited to complete similitude conditions, e.g., all geometrical dimensions are scaled by the same factor. Machine designs such as the size range of gear boxes are usually incompletely similar, i.e., the geometrical dimensions are scaled by different factors. Consequently, practical design engineering can only benefit from scaling laws if they can efficiently be derived and if analysis results can be scaled under incomplete similitude conditions as well.

The aim of this thesis is to contribute to scaling laws for analyses in vibroacoustics and machine acoustics. A method to efficiently derive scaling laws is developed and validated for complete similitude conditions. This method combines similitude analysis with *sensitivity analysis*. Sensitivity analysis investigates the effect of input parameters of a system on its output parameters [5]. It is shown that scaling laws can efficiently be derived by combining similitude analysis and sensitivity analysis. The proposed scaling method is extended to incomplete similitude conditions and validated for several structures,[2] e.g., vibrating plates and shells as well as the gear boxes of the size range shown in Figure 1.1.

Section 1.1 motivates the topic and proposes three research hypotheses of this thesis. Section 1.2 defines terms that are used throughout the thesis. Particularly, the term *model* is properly defined since it is used with different meanings in similitude analysis and sensitivity analysis. This includes the definition of common engineering model types. Section 1.3 outlines the content of the subsequent chapters.

[2] See Section 1.2 for a proper definition of the term *structure*.

1.1 Scope

On the one hand, available similitude analysis methods are used manually in order to derive scaling laws, i.e., the governing equations are written down by hand and a similitude analysis is performed by transforming the governing equations manually. Applying scaling laws is an uncertain extrapolation. Particularly, some amount of inaccuracy needs to be accepted under incomplete similitude conditions. On the other hand, provided that scaling laws are known the main benefits for vibroacoustic analyses are

- *Vibroacoustic analyses of size ranges*: The vibroacoustic responses of an entire size range are predicted by transferring the vibroacoustic responses of one reference structure to the scaled structures of the size range.
- *Prototype testing*: The vibroacoustic responses of an original structure are estimated based on measurements of a scaled structure. For example, large structures are scaled down to fit the laboratory scale.
- *Project synergies*: The vibroacoustic responses of a new structure are estimated based on available vibroacoustic responses of an existing (similar) structure. For example, a first estimate of the vibroacoustic responses can be used to optimize a new structure during early product development process stages.

In order to profit from these benefits, new methods to efficiently derive scaling laws are needed, particularly for scaling vibroacoustic responses under incomplete similitude conditions. Furthermore, measures that determine the accuracy of scaling laws and scaled vibroacoustic responses are needed to control the uncertainty of scaled vibration responses.

This thesis contributes to efficiently derive scaling laws by combining similitude analysis with sensitivity analysis, and a new scaling method is proposed. Four consecutive steps are necessary to elaborate the new scaling method as illustrated in Figure 1.2. In the first step, the *potential analysis*, it is shown that similitude analysis and sensitivity analysis can actually be combined and that both methods actually benefit from each other. Both methods are applied to a double mass oscillator and possible links between both methods are elaborated. The double mass oscillator is considered a comprehensible test structure for the purpose of the potential analysis.

step	main tasks	test structures
I. potential analysis	- apply similitude analysis methods - apply sensitivity analysis methods - elaborate possible links of the methods	double mass oscillator
II. method development	- combine similitude analysis and sensitivity analysis - verify and validate scaling laws - propose a-posteriori measures for complete similitude conditions	plates and a plate-like structure in complete similitude
III. method enhancement	- enhance proposed scaling method to incomplete similitude conditions - validate scaling laws - propose a-posteriori measures for the accuracy of the scaling laws	plates in incomplete similitude
IV. method application	- apply proposed scaling method to size range of gear boxes - validate scaling laws - assess scaling laws by the proposed a-posteriori measures	size range of gear boxes

Figure 1.2: overview of the four consecutive steps to develop a new scaling method in this thesis

The second step, the *method development*, proposes the new scaling method that combines similitude analysis with sensitivity analysis. It is verified that scaling laws of rectangular plates derived by the proposed scaling method are identical to those from literature. During the validation it is shown that the derived scaling laws scale the vibration responses of rectangular plates and a plate-like structure sufficiently well. A-posteriori measures are proposed to assess whether the scaled structures are actually in complete similitude to the reference structure. The third step, the *method enhancement*, enhances the proposed scaling method to geometrically incomplete similitude conditions. Scaling laws for rectangular plates in geometrically incomplete similitude are derived and validated by comparing scaled vibration responses of the proposed scaling method with those of a scaling method from literature. In order to assess the accuracy of the scaled vibration responses an a-posteriori accuracy measure is proposed. The fourth step, the *method application*, illustrates how the proposed scaling method can be applied to the size range of gear boxes shown in Figure 1.1. This demonstrates that the proposed scaling method can be used to investigate vibroacoustic responses of entire size ranges in practical design engineering.

In summary, this thesis proposes three research hypotheses:

1. Similitude analysis and sensitivity analysis can be combined to directly derive scaling laws. The proposed scaling method benefits from the synergies of similitude analysis and sensitivity analysis. The proposed

scaling method is more efficient than existing scaling methods since the scaling laws can be directly derived from a sensitivity analysis without prior knowledge of the scaling behavior.

2. The proposed scaling method is enhanced to scale the vibration responses of rectangular plates under geometrically incomplete similitude conditions. The scaled vibration responses are not exact, but sufficiently accurate.

3. The accuracy of scaled vibration responses can be assessed by a-posteriori measures that
   - determine whether complete similitude conditions persist and
   - estimate the accuracy of the scaled vibration responses with respect to vibration responses from numerical simulations or experimental measurements.

1.2 Definitions

This section defines the terms *structure*, *model* (including common model types for engineering), *simulation*, *verification*, and *validation* as they are connoted in this thesis. Particularly, similitude analysis and sensitivity analysis use the term model with different meanings. Thus, the term model needs to be properly defined for this thesis. Note that the terms *similitude analysis* and *sensitivity analysis* are defined in Chapter 2.

Structure is an umbrella term for mechanical objects that are subject to mechanical vibrations. For example, one gear box of the size range of gear boxes (see Figure 1.1) is a structure.

In similitude analysis a model can be defined according to MURPHY [6, p. 57]:

> *A model is a device which is so related to a physical system that observations on the model may be used to predict accurately the performance of the physical system in the desired respect.*

For example, the vibration responses of one reference gear box of the size range in Figure 1.1 are measured and transferred to the other gear boxes. The reference gear box is the model of the other gear boxes in the sense of MURPHY'S model definition. Due to the similitude of the reference gear box and the other gear boxes it is possible to accurately predict their vibration responses [6].

In sensitivity analysis a model can be defined according to SALTELLI [5, p. 3]:

> *Models (...) approximate or mimic systems and processes of different natures (e.g. physical, environmental, social, or economic), and of varying complexity.*

This definition is based on a more formal modeling process, where modeling is defined as translating from one formalism to another one [7]. For example, a mathematical model of a gear box is a model in the sense of SALTELLI'S model definition. Thus, models describe the investigated structure by governing equations in order to reduce its complexity [5, p. 3]. Models will be used for both purposes in this thesis. Governing equations are used to calculate vibrations of structures and scaling laws are used to predict vibration responses of scaled structures. The following definition of the term model is used in this thesis since it addresses both aspects:

A **model** is a representative of a related original structure that accurately describes, approximates, or predicts the behavior of the structure in a desired manner.

In design engineering, modeling is a bottom-up process. Models are deduced either by building an experimental setup (referred to as *experimental models*) or by deriving governing equations (referred to as *virtual models*). Using these models, i.e., performing measurements or solving governing equations, is referred to as *experimental simulation* or *virtual simulation*, respectively. A model that represents how changes of a model input affects the model output are referred to as *meta-models*. Scaling laws are meta-models that represent the scaling behavior of a model based on similitude theory.

A **verification** shows whether the proposed scaling method leads to correct scaling laws. For example, scaling laws are derived from the proposed scaling method and are compared with scaling laws from literature.

A **validation** analyzes whether the (verified) scaling laws are able to predict the vibration responses of scaled structures in the desired manner. Validation uses several measures to assess the accuracy of the scaled vibration responses.

1.3 Outline

The subsequent chapters are organized as follows: The fundamentals of machine acoustics, relevant to this thesis, as well as the fundamentals of similitude analysis and sensitivity analysis are reported in Chapter 2. The sections on similitude analysis and sensitivity analysis include a literature review, where applications of these methods in vibroacoustics are described. Chapter 3 applies similitude analysis and sensitivity analysis methods to a double mass oscillator. It is shown that both methods can actually be combined and that they can benefit from their synergies. In Chapter 4 a new scaling method is proposed that combines similitude analysis and sensitivity analysis. The scaling laws are derived for complete similitude conditions. They are verified and validated for rectangular plates and for a plate-like structure. In Chapter 5 the method is extended to geometrically incomplete similitude conditions. It is shown that the vibration responses of plates in geometrically incomplete similitude can be scaled with sufficient accuracy. A-posteriori measures are developed in order to determine the limits of the proposed scaling method. Finally, the method is applied to the size range of gear boxes shown in Figure 1.1. Chapter 6 summarizes the scaling method developed in this thesis and discusses the main results based on the research hypotheses posed in Section 1.1. Remarks on future research are made and further developments of the proposed scaling method are outlined.

2 Fundamentals

This chapter introduces the fundamentals of machine acoustics (Section 2.1), similitude analysis (Section 2.2), and sensitivity analysis (Section 2.3). Sections 2.2 and 2.3 also review literature on similitude analysis and sensitivity analysis in vibroacoustics, respectively. A summary of the literature review is given in Section 2.4.

2.1 Fundamentals of machine acoustics

Machine acoustics is a discipline of vibroacoustics that aims at noise and vibration control of machinery. Dynamic forces due to the machine operation cause the machine structure to vibrate. Vibrations at frequencies that are within the audible frequency range (20 Hz to 20 000 Hz) are referred to as structure borne sound [8]. Section 2.1.1 introduces virtual models to calculate the vibrations of structures. In particular, a virtual model to calculate the vibrations of rectangular plates is derived since machine housings often consist of plates, plate-like structures, or assemblies of plates that cause airborne noise [8]. Airborne noise induced by structure borne sound is also referred to as *indirect noise* [9]. Section 2.1.2 introduces the fundamental equation of machine acoustics, which describes indirect noise generation.

2.1.1 Virtual models for structural vibrations

The vibrations of continuous mechanical structures are given by the wave equation

$$\frac{\partial^2 \mathbf{u}}{\partial \tau^2} - c^2 \Delta \mathbf{u} = \mathbf{f}, \tag{2.1}$$

where $\mathbf{u}$, $\mathbf{f}$, c, and τ denote the displacements, the external loads (per unit mass), the wave propagation speed, and the time, respectively. Equation (2.1) is a partial differential equation and closed form solutions exist only for few simple structures, e.g., vibrating thin plates. Vibration problems of more complex structures, e.g., gear boxes, have to be solved numerically. Equation (2.1) is

rewritten into a second order ordinary differential equation with a finite number of degrees of freedom

$$\mathbf{M}\ddot{\mathbf{u}} + \mathbf{D}\dot{\mathbf{u}} + \mathbf{K}\mathbf{u} = \mathbf{F}, \tag{2.2}$$

where **M**, **D**, **K**, and **F** are the mass matrix, the damping matrix, the stiffness matrix, and the load vector, respectively. The dots indicate time derivatives. Equation (2.2) is obtained from the finite element method (FEM). Transforming Eq. (2.2) into the frequency domain leads to a system of linear equations, which can efficiently be solved [10]. The strength of the FEM is that it can deal with complex geometries such as gear boxes. Fundamentals of the FEM are described in [10].

Many noise and vibration issues are related to vibrations of plate and shell structures such as car bodies or aircraft fuselages. The KIRCHHOFF-LOVE theory describes vibrations of thin shells [11, 12], while the MINDLIN-REISSNER theory describes vibrations of moderately thick shells [13, 14]. Shells can be considered thin if their length and width dimensions are much larger than their thickness.[1] The vibrations of thin shells are calculated from analytical governing equations that are derived from Eq. (2.1) using appropriate boundary conditions. The vibrations of moderately thick shells are calculated from Eq. (2.2) using FEM, since C^0-continuity of the displacement functions suffices for MINDLIN-REISSNER theory [10]. Considering the free vibrations, i.e., $\mathbf{f} = 0$, in transverse direction u_z Eq. (2.1) yields [15]

$$\Delta^2 u_z + \frac{\rho t}{B}\frac{\partial^2 u_z}{\partial \tau^2} = 0, \tag{2.3}$$

where ρ and t denote the mass density and the plate thickness, respectively. The flexural stiffness B reads

$$B = \frac{E t^3}{12(1-\mu^2)}, \tag{2.4}$$

[1] Section 4.2.3 proposes a more precise definition in terms of a length (or width) to thickness ratio, which is relevant for the application of scaling laws.

where E and μ are the material's YOUNG's modulus and POISSON's ratio, respectively. Assuming time-harmonic displacements, the natural frequencies can be obtained from the eigenvalue equation

$$\left(\Delta^2 - \frac{\rho t \omega^2}{B}\right) U = 0, \tag{2.5}$$

where ω denotes the angular frequency and U are the eigenvectors (or mode shapes) [15]. Considering a rectangular plate as shown in Figure 2.1 with all edges simply supported, its natural frequencies and mode shapes read

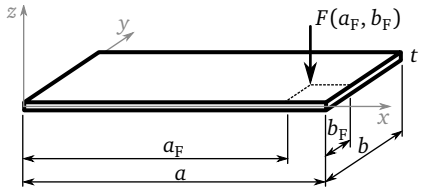

Figure 2.1: simply supported rectangular plate excited by a single point force

$$f_{m,n} = \frac{\omega_{m,n}}{2\pi} = \frac{\pi}{2} t \sqrt{\frac{E}{12\rho\,(1-\mu^2)}} \left(\left(\frac{m}{a}\right)^2 + \left(\frac{n}{b}\right)^2\right) \tag{2.6}$$

and

$$U_{m,n} = \hat{u}_{m,n} \sin\left(\frac{\pi x}{a}\right) \sin\left(\frac{\pi y}{b}\right) \tag{2.7}$$

with m and n being the number of half-waves in x- and y-direction, respectively, and $\hat{u}_{m,n}$ being the amplitude coefficients [15]. The forced vibration velocities due to a dynamic excitation force $F\,(a_\mathrm{F},\, b_\mathrm{F})$, see Figure 2.1, is given by the superposition of modes. Taking the time derivative of the displacements yields the vibration velocities

$$\begin{aligned} \underline{\tilde{v}}(x,y) = \frac{2\tilde{F}\mathrm{i}f}{\pi\rho abt} \sum_{m=1}^{\infty}\sum_{n=1}^{\infty} & \frac{\sin\left(\frac{m\pi a_\mathrm{F}}{a}\right)\sin\left(\frac{n\pi b_\mathrm{F}}{b}\right)}{f_{m,n}^2 - f^2 + \mathrm{i}\eta f_{m,n}^2} \\ & \cdot \sin\left(\frac{m\pi x}{a}\right)\sin\left(\frac{n\pi y}{b}\right), \end{aligned} \tag{2.8}$$

where f is the frequency of excitation and η denotes the material loss factor [8]. The underscore indicates complex variables and the tilde denotes the root mean square (RMS). Note that the frequency dependence of $\underline{\tilde{v}}(x, y)$ is omitted in Eq. (2.8) and it will be omitted for convenience hereafter as well. The spatial mean squared vibration velocity reads

$$\overline{\tilde{v}^2} = \frac{1}{S} \int_S \left| \underline{\tilde{v}}(x, y) \right|^2 \mathrm{d}S. \tag{2.9}$$

Dividing Eq. (2.9) by $\tilde{F}^2$ and multiplying by the surface area S yields the so-called mean squared transfer admittance (MSTA)

$$Sh_{\mathrm{T}}^2 = S \frac{\overline{\tilde{v}^2}}{\tilde{F}^2}. \tag{2.10}$$

The excitation position $(a_{\mathrm{F}}, b_{\mathrm{F}})$ is inserted for x and y in Eq. (2.8), the mean squared velocity is obtained from Eq. (2.9) and inserted into Eq. (2.10). The surface area of a rectangular plate equals $S = ab$. Thus, the MSTA of the simply supported rectangular plate yields

$$Sh_{\mathrm{T}}^2 = \frac{f^2}{\pi^2 \rho^2 t^2 ab} \sum_{m=1}^{\infty} \sum_{n=1}^{\infty} \frac{\sin^2\left(\frac{m\pi a_{\mathrm{F}}}{a}\right) \sin^2\left(\frac{n\pi b_{\mathrm{F}}}{b}\right)}{\left(f_{m,n}^2 - f^2\right)^2 + \eta^2 f_{m,n}^4}. \tag{2.11}$$

Eq. (2.11) is used in Section 4.2 to derive scaling laws for the MSTA of a vibrating rectangular plate.

2.1.2 The fundamental equation of machine acoustics

The MSTA, e.g., for thin rectangular plates given by Eq. (2.11), is linked to the radiated sound power by the fundamental equation of machine acoustics [16]

$$P = \tilde{F}^2 Sh_{\mathrm{T}}^2 \sigma \rho_{\mathrm{a}} c_{\mathrm{a}}, \tag{2.12}$$

with P, σ, and $\rho_a c_a$ being the sound power, the radiation efficiency, and the acoustic impedance, respectively. ρ_a is the air's density and c_a is the speed of sound in air. Inserting Eq. (2.10) into Eq. (2.12) yields

$$P = \overline{\tilde{v}^2} S \sigma \rho_a c_a. \tag{2.13}$$

Solving Eq. (2.13) for the radiation efficiency yields

$$\sigma = \frac{P}{\overline{\tilde{v}^2} S \rho_a c_a}. \tag{2.14}$$

The radiation efficiency describes the share of structure borne sound power that is radiated as airborne sound power [17]. It is rather a property of the entire vibroacoustic system than of the vibrating structure itself [8]. The radiation efficiency can be obtained from experimental simulations by sound power measurements and vibration velocity measurements [9] or from the radiation resistance matrix obtained from virtual simulations [18].

2.2 Similitude methods and the fundamentals of scaling laws

Two physical systems are in similitude if they are described by the same governing equations and if their input and output parameters have equal relations [6]. The governing equations of each physical system can be written in a general functional format [19]

$$\mathfrak{f}(Q_1, Q_2, \ldots, Q_i, \ldots Q_N) = 0, \tag{2.15}$$

where $\mathfrak{f}$ denotes any functional and Q_i are quantities that fully characterize the physical system such as geometrical dimensions, material properties, time, or displacements. The total number of quantities is denoted by N. Providing that two physical systems are similar (referred to as *being in similitude*) the quantities Q_i must be homologous, which is the case if each quantity of one physical system can be allocated to a quantity of the other physical system. Homologous quantities do not necessarily have the same value. Providing homology of the quantities Q_i, Eq. (2.15) still holds for nonlinear physical systems [4].

In similitude theory the two physical systems are often referred to as *model* and *prototype*. This thesis uses the following terms to avoid confusion with the term model defined in Section 1.2:

- *parent*: physical system with known behavior that is used for prediction,
- *replica*: physical system with unknown behavior that is predicted.

The parent and the replica can be described by the general functionals $\mathfrak{f}^{(\mathrm{p})}$ and $\mathfrak{f}^{(\mathrm{r})}$, respectively. Their ratio is defined to be their *scaling factor*[2]

$$\phi_{\mathfrak{f}} = \frac{\mathfrak{f}^{(\mathrm{r})}}{\mathfrak{f}^{(\mathrm{p})}}, \tag{2.16}$$

where the quantities $Q_i^{(\mathrm{p})}$ and $Q_i^{(\mathrm{r})}$ are homologous [20]. If all quantities Q_i are homologous, the parent and the replica are in *complete similitude*. Otherwise they are in *incomplete similitude*. Complete similitude is often too restrictive in practical design engineering, e.g., size ranges are usually in incomplete similitude. Incomplete similitude is also referred to as *distorted similitude* [6].

Similitude theory distinguishes three types of similitude [4]:

- *geometrical similitude* requires that all length ratios of the parent and of the replica are equal.
- *kinematic similitude* requires that all length ratios and the time ratio of the parent and of the replica are equal, i.e., the velocities are homologous.
- *dynamic similitude* requires that all length ratios, the time ratio, and all force ratios of the parent and of the replica are equal.

Vibrating structures are in dynamic similitude if their mode shapes are in the same order and if they have equal damping [21, 22].

Similitude theory is introduced in several textbooks [4, 6, 20, 23–25] and possible applications are exemplified. Coutinho [26] reviews similitude analysis methods in structural engineering including vibroacoustics. Three different similitude analysis methods are used in vibroacoustics to derive scaling laws:

[2] $\phi_{\mathfrak{f}} > 1$ is a scale-up, $\phi_{\mathfrak{f}} < 1$ is a scale-down, and if $\phi_{\mathfrak{f}} = 1$ the replica equals the parent.

- dimensional analysis (DA),
- similitude theory applied to governing equations (STAGE),
- similitude and asymptotic models for structural-acoustic research and applications (SAMSARA) [26].

DA and STAGE are introduced in [4, 6, 20, 23–25]. They apply to various engineering problems, while SAMSARA has been exclusively developed for vibroacoustic analyses. DA, STAGE, and SAMSARA are introduced in the subsequent sections and literature on their applications in vibroacoustics is reviewed.

2.2.1 Dimensional analysis

DA aims at finding a set of dimensionless quantities that are invariant when a physical system is scaled. If Eq. (2.15) is complete, i.e., it contains all relevant quantities of a physical system, it can be reduced to

$$\mathfrak{f}\left(\Pi_1, \Pi_2, \ldots, \Pi_j, \ldots \Pi_{N-K}\right) = 0, \tag{2.17}$$

where Π_j are dimensionless products of the quantities $Q_1, Q_2, \ldots, Q_N$ and K is the number of fundamental dimensions. This is known as BUCKINGHAM'S Π-theorem of the similitude theory [19]. It is based on the fact that equations must be dimensionally homogeneous. The fundamental dimensions are independent dimensions that need to be chosen. The dimensions of all quantities Q_i are expressed in terms of these fundamental dimensions. In vibroacoustics the fundamental dimensions are usually MLT ($K = 3$), i.e., mass (dimension M), length (dimension L), and time (dimension T) are fundamental dimensions. The dimensions of all other quantities, e.g., force (dimension MLT^{-2}), are derived from the fundamental dimensions [4].[3] The Π-products are derived by combining the quantities Q_i to a dimensionless product

$$\Pi_j = \prod_{i=1}^{N} Q_i^{\alpha_{i,j}}, \tag{2.18}$$

[3] Note that *dimension* and *unit* are not identical. The dimension is the inherent property of a quantity Q_i (e.g., dimension of a length), whereas the unit depends on the selected unit system (length in meters, feet, etc.).

where $j = 1,\ 2, \ldots, N-K$. The powers $\alpha_{i,j}$ are obtained by solving the set of linear equations

$$\sum_{i=1}^{N} \alpha_{i,j} = 0. \tag{2.19}$$

Inserting the powers $\alpha_{i,j}$ calculated from Eq. (2.19) into Eq. (2.18) yields dimensionless Π-products. The Π-products can be obtained only if the number of quantities is larger than the number of fundamental units. Equation (2.19) is then under-determined and the set of Π-products is ambiguous. Thus, several sets of Π-products exist for the same physical system [4, 6, 20, 23]. For simple physical systems, e.g., a single mass oscillator, BAKER suggests to directly deduce Π-products from Eq. (2.15) by trial [4, p. 19 et seq.]. Within the *method of repeating variables* [24, p. 124] arbitrary values for a number of $N-K$ powers $\alpha_{i,j}$ are chosen, Eq. (2.19) is solved for the remaining powers $\alpha_{i,j}$, and a Π-product is calculated from Eq. (2.18). This procedure is repeated until $N-K$ Π-products have been obtained [6, 20, 24]. A systematic approach to calculate Π-products is shown in [4, 20, 23]. The powers $\alpha_{i,j}$ are written into a so-called dimension matrix, which reads

$$\begin{array}{c} \\ \mathsf{M} \\ \mathsf{L} \\ \mathsf{T} \end{array} \begin{array}{c} \begin{array}{cccc} Q_1 & Q_2 & \cdots & Q_N \end{array} \\ \begin{pmatrix} \alpha_{1,1} & \alpha_{1,2} & \cdots & \alpha_{1,N} \\ \alpha_{2,1} & \alpha_{2,2} & \cdots & \alpha_{2,N} \\ \alpha_{3,1} & \alpha_{3,2} & \cdots & \alpha_{3,N} \end{pmatrix} \end{array} \tag{2.20}$$

in case of MLT being fundamental dimensions. By using GAUSSIAN elimination, Eq. (2.20) can be transformed into a matrix that is composed of an identity matrix and a sub-matrix

$$\begin{array}{c} \\ \mathsf{M} \\ \mathsf{L} \\ \mathsf{T} \end{array} \begin{array}{c} \begin{array}{ccccccc} Q'_{1,\mathrm{f}} & Q'_{2,\mathrm{f}} & Q'_{3,\mathrm{f}} & Q'_{1,\mathrm{b}} & Q'_{2,\mathrm{b}} & \cdots & Q'_{N-K,\mathrm{b}} \end{array} \\ \begin{pmatrix} 1 & 0 & 0 & \alpha'_{1,1} & \alpha'_{1,2} & \cdots & \alpha'_{1,N-K} \\ 0 & 1 & 0 & \alpha'_{2,1} & \alpha'_{2,2} & \cdots & \alpha'_{2,N-K} \\ 0 & 0 & 1 & \alpha'_{3,1} & \alpha'_{3,2} & \cdots & \alpha'_{3,N-K} \end{pmatrix}. \end{array} \tag{2.21}$$

The transformed quantities and powers are indicated by the prime symbol $(\cdot)'$. The transformed quantities that belong to the identity matrix are referred to as *free* quantities (labeled by subscript f) and those that belong to the sub-matrix

are referred to as *bounded* quantities (labeled by subscript b). According to [23] the Π-products can be calculated from

$$\Pi_j = \frac{Q'_{j,\mathrm{b}}}{\prod_{i=1}^{K} \left(Q'_{i,\mathrm{f}}\right)^{\alpha'_{i,j}}}. \tag{2.22}$$

Although the Π-products can systematically be calculated, DA lacks a validation procedure that interprets the Π-products from a physical point of view. Usually DA requires several iterations until a valid set of Π-products is derived [24]. The scaling laws are derived from the Π-products by introducing the scaling factors [4, 6]

$$\phi_{Q_i} = \frac{Q_i^{(\mathrm{r})}}{Q_i^{(\mathrm{p})}}. \tag{2.23}$$

In structural engineering, scaling laws based on DA are often used to scale-up measurement results of laboratory tests [26]. Particularly, structural vibrations of large structures such as spacecrafts [27] or gantry cranes [28] as well as building structures subject to earthquakes [29] are studied on laboratory scales. The scaling laws of vibrating structures and of the acoustic intensity of a cavity are derived by MURPHY [6] for complete similitude conditions. Scaling laws for incomplete similitude conditions drop the invariance of those Π-products that are negligible for the desired purpose [27]. In order to distinguish between important and negligible Π-products KITTIRUNGSI proposes an energy-based measure to select the important Π-products of a quarter car suspension system [30].

2.2.2 Similitude theory applied to governing equations

STAGE is introduced in the textbooks [4, 24, 25]. Consider the governing equation of a parent

$$\mathfrak{f}^{(\mathrm{p})}\left(Q_1^{(\mathrm{p})}, Q_2^{(\mathrm{p})}, \ldots, Q_N^{(\mathrm{p})}\right) = 0. \tag{2.24}$$

A replica must fulfill the same governing equation, i.e.,

$$\mathfrak{f}^{(\mathrm{r})}\left(Q_1^{(\mathrm{r})}, Q_2^{(\mathrm{r})}, \ldots, Q_N^{(\mathrm{r})}\right) = 0. \tag{2.25}$$

Provided that the parent and the replica are in similitude, Eqs. (2.24) and (2.25) are proportional [20]. Defining scaling factors in analogy to Eq. (2.23) and inserting them into Eq. (2.24) yields the dimensionless equation

$$\mathfrak{f}\left(\phi_{Q_1}, \phi_{Q_2}, \ldots, \phi_{Q_N}\right) = 0. \tag{2.26}$$

However, the dimensionality of Eq. (2.26) equals that of Eq. (2.24). In contrast, the dimensionality in DA is reduced by the number of fundamental dimensions, see Eq. (2.17). The scaling laws can be derived from Eq. (2.26) without solving it [4]. STAGE yields unique and valid scaling laws, while scaling laws from DA are ambiguous and several DA are necessary until valid scaling laws are derived. Consequently, STAGE is more common in vibroacoustic analyses. Literature on scaling laws for vibroacoustic analyses focuses on vibrating thin shells. Nevertheless, a few approaches to scaling laws for machine noise and vibrations are discussed in literature as well.

Soedel [31] derives scaling laws for in-plane and flexural vibrations of thin shells. A flat plate is found to be still in complete similitude, although the lengths are scaled by a different factor than the thickness. Wu applies STAGE to vibrating rectangular plates with simply supported edges in complete similitude that are subject to one dynamic point force [32], one moving point force [33], and several moving point forces [34]. Rezaeepazhand and Simitses investigate complete and incomplete similitudes of vibrating plates [35, 36] and circular cylindrical shells [37] made from fiber-reinforced plastics. Besides geometrically incompletely similar shells [37], the material properties such as number of plies [36, 37] and stacking sequence [37] are considered for the scaling laws as well. Cheng [38] uses STAGE to derive scaling laws for a vibrating rectangular plate coupled to an acoustic cavity, where complete similitude is considered. Torkamani [39] derives scaling laws for the free vibrations of geometrically completely similar stiffened cylindrical shells including experimental simulations to validate the scaling laws. Singhatanadgid [40] validates the scaling laws for the natural frequencies of completely similar rectangular plates in experimental simulations. Several design parameters of the plates such as length aspect ratios and material properties are investigated. The boundary conditions of the parent and the replica need to be identical in order to accurately scale the natural frequencies [40]. Xiaojian [41] scales frequency response functions from experimental simulations of completely similar rectangular plates that are excited by an artificial turbulent boundary layer excitation.

PAHL and BEITZ [1–3] propose a power law as a more practical approach to derive scaling laws for size ranges of machines. Among others they define geometrical and dynamic similitude conditions. This approach is used by WEBER [42] to derive scaling laws for the sound power of a size range of gear boxes and by HEYNE [43, 44] to investigate acoustic similitudes of a size range of axial piston pumps. SUEKI [45] uses prototype testing and scaling laws to investigate rolling noise and impact noise of rail joints. HERRIN [46] studies the noise of a jumbo drill using an additively manufactured scale model and panel contribution analysis. The scaling laws are rather motivated by the reciprocity principle [47] than by detailed considerations of the similitude conditions. Scaling laws based on the wave equation are used by GUO and CHEN [48, 49] as well as by RUAN [50] for prototype testing of the noise of various railway girders and of the insertion loss of silencers in air conditioning ducts, respectively.

2.2.3 Similitude and asymptotic models for structural-acoustic research and applications

SAMSARA is an energy-based scaling method for vibroacoustic analyses developed by DE ROSA and FRANCO [21, 22, 51–55]. It is an extension of the scaling method *asymptotic scaled modal analysis* (ASMA) [21, 51, 52, 55], which is based on the *energy distribution approach* (EDA) [56]. The EDA uses natural frequencies and mode shapes of a system that is assembled from subsystems to estimate the vibration energy distribution in each subsystem [56]. ASMA increases the valid frequency range of EDA by artificially increasing the damping to keep the energy of the parent [51], i.e., ASMA takes incomplete similitude conditions into account [21]. ASMA is limited to global vibration responses such as natural frequencies and surface-averaged vibration responses. The method is applied to coupled beams, plates with a coupled beam, and assemblies of rectangular plates [21, 52, 55]. SAMSARA extends ASMA to (1) scale local vibration responses (e.g., at the driving point) and (2) vibrating structures coupled to an acoustic cavity [53]. SAMSARA derives the scaling laws from a generalized modal approach [22]. Thus, SAMSARA can use mode shapes and natural frequencies from finite element (FE) models, but the scaling laws themselves need to be derived manually. SAMSARA predicts vibration responses of plates [22, 57] and stiffened cylindrical shells [54, 58] obtained from virtual simulations under geometrically complete and incomplete similitude conditions. Experimental simulations validate the scaling laws derived from SAMSARA for vibrating cantilever plates [57] and simply supported plates [59]. The similitude of the damping is

essential for accurately scaling the vibration responses from experimental simulations [57]. SAMSARA is further extended to scaling the sound power and sound intensity of rectangular plates under harmonic [59] and random excitation [60].

The accuracy of the scaled vibration responses is assessed in an a-posteriori analysis using the HAUSDORFF distance [57, 58]. The HAUSDORFF distance is the maximum of the minimum distances between two sets of points [61], see Appendix A.5 for its mathematical definition.

2.3 Fundamentals of sensitivity analysis

Sensitivity analysis (SA) analyzes how the responses of a system change due to a perturbation of its design parameters [5]. This thesis uses SA to derive meta-models. After introducing the fundamentals of SA, literature on SA methods that focuses on meta-modeling and scaling in vibroacoustics is reviewed. If a meta-model is derived from a TAYLOR series expansion of the system responses at a particular point in the design parameter space, the SA is referred to as *local sensitivity analysis* (LSA) [5]. If a meta-model is derived from a sampling of the entire parameter space and a subsequent regression analysis, the SA is referred to as sampling-based *global sensitivity analysis* (GSA). SA methods are used for numerical optimization [62], uncertainty analyses [5], or design of experiments [63] as well, but these applications are out of the scope of this thesis.

The design parameters and the responses that are used for an SA are written as sets

$$\mathbf{X}^{(\mathrm{p})} = \left\{X_1^{(\mathrm{p})}, X_2^{(\mathrm{p})}, \ldots, X_N^{(\mathrm{p})}\right\}, \qquad \mathbf{Y}^{(\mathrm{p})} = \left\{Y_1^{(\mathrm{p})}, Y_2^{(\mathrm{p})}, \ldots, Y_M^{(\mathrm{p})}\right\}. \tag{2.27}$$

The superscript (p) is chosen in agreement with the notation of similitude analysis, see Section 2.2. It indicates the parent system, i.e., the system with the original values of the design parameters. A perturbed (or *scaled*) system is referred to as *replica* and, thus, denoted by the superscript (r). The design parameters in the set $\mathbf{X}$ span the parameter space of the system. If the system is modeled by FE, two types of design parameters can be distinguished. *Sizing design parameters* can be altered without affecting the spatial location of FE nodes (e.g., shell thickness). Altering *shape design parameters* (e.g., a length) causes the FE nodes to move during the SA. The latter can affect the accuracy of the sensitivities [62].

2.3.1 Local sensitivity analysis

Each response Y_k of the set in Eq. (2.27) can be expanded into a TAYLOR series [5]

$$Y_k^{(\mathrm{r})}\left(\mathbf{X}^{(\mathrm{r})}\right) = Y_k^{(\mathrm{p})}\left(\mathbf{X}^{(\mathrm{p})}\right) + \sum_{j=1}^{N} \frac{\partial Y_k^{(\mathrm{p})}}{\partial X_j^{(\mathrm{p})}} \left(X_j^{(\mathrm{r})} - X_j^{(\mathrm{p})}\right) + \frac{1}{2} \sum_{j=1}^{N} \sum_{l=1}^{N} \frac{\partial^2 Y_k^{(\mathrm{p})}}{\partial X_j^{(\mathrm{p})} \partial X_l^{(\mathrm{p})}} \left(X_j^{(\mathrm{r})} - X_j^{(\mathrm{p})}\right)\left(X_l^{(\mathrm{r})} - X_l^{(\mathrm{p})}\right) + \cdots . \tag{2.28}$$

The partial derivative

$$\frac{\partial Y_k^{(\mathrm{p})}}{\partial X_j^{(\mathrm{p})}} = S_{j,k} \tag{2.29}$$

denotes the first order sensitivity $S_{j,k}$ of the response $Y_k^{(\mathrm{p})}$ with respect to the design parameter $X_j^{(\mathrm{p})}$. First order sensitivities suffice for many engineering purposes [5]. Several sensitivity calculation methods exist for linear and nonlinear system analysis and design optimization [62, 64]. Among these methods the central difference scheme

$$\frac{\partial Y_k^{(\mathrm{p})}}{\partial X_j^{(\mathrm{p})}} \approx \frac{Y_k^{(+)} - Y_k^{(-)}}{X_j^{(+)} - X_j^{(-)}} \tag{2.30}$$

is popular due to its simple implementation [5, 65]. $X_k^{(+)}$ and $X_k^{(-)}$ indicate the design parameters that are perturbed during the LSA. This leads to the perturbed responses $Y_k^{(+)}$ and $Y_k^{(-)}$, respectively. The accuracy of the sensitivities depends on the proper choice of $X_j^{(+)}$ and $X_j^{(-)}$ [66]. On the one hand, a small perturbation is required since the central difference scheme is a linear approximation. On the other hand, a small perturbation may cause changes of the responses that are smaller than the computational accuracy. Thus, different values for $X_j^{(+)}$ and $X_j^{(-)}$ must be tested in practice in order to obtain a sufficient perturbation [5]. Calculating sensitivities from Eq. (2.30) for N design parameters requires $2N + 1$ calculations including the parent since each design parameter is altered separately.

LSA can be used to study the effect of design parameters on frequency response functions, e.g., of structural-acoustic systems [67, 68]. However, investigations on LSA rather focus on developing and validating sensitivity calculation methods [62, 64, 67, 68] or comparing their performance [65] than using sensitivities to build meta-models. YANG [69] uses a TAYLOR series expansion to predict the changes of vibration response functions due to changes of mass, stiffness, and damping of a single mass oscillator, a three story building, and a part of a suspension system. KRAMER [70] develops a meta-model in terms of a power law from a TAYLOR series expansion of the vibration response of a single mass oscillator. A similar approach is used by ESLAVA [71] to obtain sensitivities of intermolecular potential parameters. By introducing the sensitivities into a power law, the intermolecular potential parameters can be scaled over several orders of magnitude. Recalling that PAHL and BEITZ [1–3] propose a power law as a scaling law for mechanical structures in complete similitude, an LSA can potentially be used to derive scaling laws.

2.3.2 Sampling-based global sensitivity analysis

Sampling-based GSA is performed in three steps. First, the design parameter space is sampled. Second, the system responses are calculated for each sample point. Third, a meta-model is obtained from a regression analysis and the sensitivities are calculated [5].

The sampling techniques for GSA can be distinguished in deterministic sampling techniques, e.g., factorial designs [63], and random sampling techniques [5], e.g., a quasi-random sampling based on HALTON or SOBOĽ number sequences [72, 73]. The quasi-random sampling techniques are preferred to factorial designs for vibration analyses since they reduce the correlation of the design parameters and spread the sample points over the entire design parameter space [74, 75].

A meta-model can be built from a linear regression analysis after the system responses have been obtained from virtual (or experimental) simulations at each sampling point. The linear regression model of the response Y_k with respect to N design parameters X_j reads [63]

$$Y_k = \beta_{0,k} + \sum_{j=1}^{N} \beta_{j,k} X_j + \varepsilon_k, \tag{2.31}$$

where $\beta_{0,k}$, $\beta_{j,k}$, and ε_k denote the interception, the regression coefficient of the design parameter X_j, and the error, respectively. The coefficients of the regression model are estimated from a least squares approximation. The regression coefficients $\beta_{j,k}$ are standardized by the standard deviations s_{X_j} and s_{Y_k}

$$S_{j,k} = \beta_{j,k} \frac{s_{X_j}}{s_{Y_k}} \tag{2.32}$$

in order to obtain the sensitivities [5]. Higher order sensitivities can be considered by introducing interactions (e.g., $X_j X_l$) or higher polynomial orders (e.g., X_j^2) into Eq. (2.31) [63].

The quality of the regression model is assessed by the adjusted coefficient of determination

$$R^2_{\text{adj}} = 1 - \left(\frac{N_{\text{sample}} - 1}{N_{\text{sample}} - N + 1} \right) \frac{SS_{\text{res}}}{SS_{\text{tot}}}, \tag{2.33}$$

where SS_{tot}, SS_{res}, and N_{sample} denote the total sum of squares, the residual sum of squares, and the number of sample points, respectively [63]. The adjusted coefficient of determination describes the share of the variance that can be explained by the regression model. If $R^2_{\text{adj}} = 1$ the regression model exactly predicts the responses at the sampling points. However, predictions of the regression model between the sampling points are not necessarily exact [63]. The normalization by $N_{\text{sample}} - 1/\left(N_{\text{sample}} - N + 1\right)$ prevents R^2_{adj} to spuriously increase just by adding more sample points, which is important to determine the number of samples N_{sample} required for GSA. The number of samples is increased step by step until the sensitivities converge. Compared to LSA, GSA requires much more samples and, thus, is computationally more expensive [5].

GSA is used to analyze the effect of design parameters on vibration responses, e.g., the effect of the thickness of a car body on the sound pressure [76] or the effect of the material stiffness and mass properties on the structure borne sound transmission of machinery [77]. The linear regression model given by Eq. (2.31) is used in [78] to scale natural frequencies of simply supported rectangular plates. Luo and Zhu use similitude analysis and a 3rd order polynomial regression model to scale natural frequencies of vibrating cantilever plates and annular plates [79–81]. Thus, it is demonstrated that

GSA can be used to scale vibration responses, but a proper regression model approach such as the polynomial order needs to be chosen. Literature lacks recommendations for a proper choice of the regression model approach or other approaches that avoid this issue.

2.4 Discussion of similitude analysis and sensitivity analysis methods

The similitude analysis methods DA, STAGE, and SAMSARA are state-of-the-art scaling methods, but vibroacoustic analyses mainly use STAGE or SAMSARA. Recall that complete similitude conditions in vibroacoustics require that

- the mode shape order of the parent and of the replica is kept [22], and
- the parent and the replica have equal damping [21].

In this case, the vibration responses of replicas can be exactly predicted from those of the parent [21, 22, 31–37, 51, 54, 57–60]. All state-of-the-art similitude analysis methods are used manually, e.g., the governing equations are manually transformed within STAGE. Literature lacks similitude analysis methods that directly derive scaling laws from any virtual model like an FE model. Such a scaling method is developed in Chapter 4 for rectangular plates and a plate-like structure in complete similitude. Measures to determine whether the structures are in complete similitude are developed as well. In case of incomplete similitude conditions, literature shows that scaling laws can approximate the vibration responses of replicas from those of a parent sufficiently well [22, 35–37, 54, 57, 58]. However, literature lacks permissible limits for the validity of scaling laws under incomplete similitude conditions. Thus, permissible limits of scaling laws are developed for rectangular plates under geometrically incomplete similitude conditions in Chapter 5. This requires appropriate measures to assess the accuracy of scaled vibration responses. It is shown in Chapter 5 that a-posteriori accuracy measures from literature such as [22, 58] can be misleading and an improved accuracy measure is developed.

The SA methods LSA and GSA can be used to investigate the effect of design parameters on system responses as well as to scale system responses. The power law approach proposed by Eslava and Kramer [70, 71] is based on SA. It is similar to the power law approach proposed by Pahl and Beitz [1–3] for investigating similitudes. Both approaches have a common ground that is investigated in Chapter 3 in order to demonstrate potential commonalities of similitude analysis and SA methods. Several application scenarios of a method that combines

similitude analysis with SA are elaborated as well. Although GSA has already been used in parallel with similitude analysis [79–81], similitude analysis and GSA have not been combined yet. Particularly, the method proposed in [79–81] requires that the user chooses a proper regression model, which can reduce the efficiency of the method or even lead to errors. The scaling method developed in Chapters 4 and 5 circumvents such shortcomings by actually combining similitude analysis with SA.

3 Similitudes and sensitivities of a double mass oscillator

This chapter uses the double mass oscillator (2-DoF oscillator) shown in Figure 3.1 to perform a potential analysis of the similitude analysis methods DA and STAGE (Section 3.1) as well as LSA and GSA (Section 3.2). This corresponds to the first step of the method development described in Figure 1.2 on page 18. The aims of the potential analysis are to illustrate how similitude analysis and SA methods apply, to compare them, and to illustrate how they can be possibly combined. Each method is qualitatively assessed and three application scenarios for a combined method are elaborated (Section 3.3).

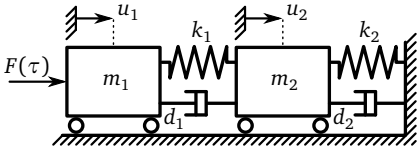

Figure 3.1: illustration of the 2-DoF oscillator

3.1 Scaling laws from similitude analysis methods

The scaling laws of the 2-DoF oscillator given in Figure 3.1 are derived from DA and from STAGE. It can be expected that both methods yield identical scaling laws, but this section aims at illustrating commonalities and differences of both methods.

3.1.1 Dimensional analysis of the 2-DoF oscillator

The DA is performed by the following steps [4]

1. list all relevant quantities as a general functional, see Eq. (2.15),
2. chose the fundamental dimensions and free quantities,
3. calculate the Π-products,
4. introduce scaling factors, see Eq. (2.23).

The general functional with $N = 10$ relevant quantities is directly obtained from Figure 3.1

$$\mathfrak{f}(u_1, u_2, m_1, m_2, k_1, k_2, d_1, d_2, F, \tau) = 0. \tag{3.1}$$

The dimensions M, L, and T are selected as fundamental dimensions. Thus, $K = 3$ and $N - K = 7$ Π-products describe the 2-DoF oscillator. The dimensions of the quantities in Eq. (3.1) read

$$\begin{aligned} [u_1, u_2] &= \mathsf{L}, & [m_1, m_2] &= \mathsf{M}, \\ [k_1, k_2] &= \mathsf{MT}^{-2}, & [d_1, d_2] &= \mathsf{MT}^{-1}, \\ [F] &= \mathsf{MLT}^{-2}, & [\tau] &= \mathsf{T}. \end{aligned} \tag{3.2}$$

Writing the powers of the dimensions in Eq. (3.2) into the dimension matrix yields

$$\begin{array}{c} \\ \mathsf{M} \\ \mathsf{L} \\ \mathsf{T} \end{array} \begin{array}{c} \begin{array}{cccccccccc} m_1 & u_1 & k_1 & m_2 & u_2 & k_2 & d_1 & d_2 & F & \tau \end{array} \\ \begin{pmatrix} 1 & 0 & 1 & 1 & 0 & 1 & 1 & 1 & 1 & 0 \\ 0 & 1 & 0 & 0 & 1 & 0 & 0 & 0 & 1 & 0 \\ 0 & 0 & -2 & 0 & 0 & -2 & -1 & -1 & -2 & 1 \end{pmatrix} \end{array}. \tag{3.3}$$

In order to calculate the Π-products Eq. (3.3) must be transformed into an identity matrix and a sub-matrix according to Eq. (2.21). Thus, m_1, u_1, and k_1 are considered free quantities, while m_2, u_2, k_2, d_1, d_2, F, and τ are bounded quantities. Choosing appropriate free quantities is the essential step in DA, since the free quantities determine whether the Π-products can be validated from a physical point of view. The aforementioned free quantities are found by trial-and-error, which is the common approach to determine free quantities [24]. Equation (3.3) is transformed into an identity matrix and a sub-matrix by applying GAUSSIAN elimination. The stepwise procedure is shown in Appendix A.1.

The following Π-products are derived from the transformed matrix and Eq. (2.22)

$$\begin{aligned}
\Pi_1 &= \frac{m_2}{m_1}, & \Pi_2 &= \frac{u_2}{u_1}, & \Pi_3 &= \frac{k_2}{k_1}, \\
\Pi_4 &= \frac{d_1}{(m_1 k_1)^{0.5}}, & \Pi_5 &= \frac{d_2}{(m_1 k_1)^{0.5}}, & & \\
\Pi_6 &= \frac{F}{k_1 u_1}, & \Pi_7 &= \frac{k_1^{0.5}\tau}{m_1^{0.5}}. & &
\end{aligned} \tag{3.4}$$

KITTIRUNGSI obtains the same set of Π-products for a quarter car suspension, which is also modeled as a 2-DoF oscillator [30]. Equation (3.4) is not a unique set of Π-products for the 2-DoF oscillator since other sets of Π-products can be obtained by choosing other free quantities [4, 6, 20, 23]. Complete similitude conditions are achieved if all Π-products are kept for a scaled 2-DoF oscillator. The Π-products can be interpreted from a physical point of view:

- Π_1, Π_2, and Π_3 are dimensionless mass, displacement, and stiffness. They are a direct consequence of the principle of homology [4].
- Π_4 and Π_5 are dimensionless damping values of the 2-DoF oscillator. They are equivalent to the definition of the material loss factor η [82]. The similitude of the loss factor is essential to achieve complete similitude conditions [21].
- Π_6 is the ratio of the excitation force and the spring force $k_1 u_1$. It is similar to the HOOKE number, which describes static similitude [3].
- Π_7 is a dimensionless time. Complete similitude is achieved if the time τ and a characteristic frequency $(k_1/m_1)^{0.5}$ are homologous.[1]

Introducing the scaling factors of Eq. (2.23) into Eq. (3.4) yields

$$\begin{aligned}
\phi_{m_1} &= \phi_{m_2}, & \phi_{u_1} &= \phi_{u_2}, & \phi_{k_1} &= \phi_{k_2}, \\
\phi_{d_1} &= \phi_{m_1}^{0.5}\phi_{k_1}^{0.5}, & \phi_{d_2} &= \phi_{m_1}^{0.5}\phi_{k_1}^{0.5}, & & \\
\phi_F &= \phi_{k_1}\phi_{u_1}, & \phi_\tau &= \phi_{m_1}^{0.5}\phi_{k_1}^{0.5}. & &
\end{aligned} \tag{3.5}$$

[1] Note that $(k_1/m_1)^{0.5}$ is not equivalent to the fundamental frequency of the 2-DoF oscillator. The natural frequencies of the 2-DoF oscillator can be obtained from Eq. (A.12) on page 145.

Equation (3.5) represents the scaling laws of the 2-DoF oscillator. In order to achieve complete similitude all scaling factors must satisfy Eq. (3.5). Setting $\phi_\tau = \phi_F = 1$ yields [30]

$$\phi_{m_1} = \phi_{m_2} = \phi_{k_1} = \phi_{k_2} = \phi_{d_1} = \phi_{d_2} = \phi_{u_1}^{-1} = \phi_{u_2}^{-1}. \tag{3.6}$$

Considering that the quantities mass, stiffness, and damping are design parameters of the 2-DoF oscillator, while the displacements are responses, Eq. (3.6) states that

- all design parameters need to be scaled by the same factor to achieve complete similitude, and
- the displacements and the design parameters scale inversely.

Recall that only the relevant quantities listed in Eq. (3.1) and the demand for dimensional homogeneity (i.e., the fundamentals of DA) have been used to draw these conclusions. Thus, if the relevant quantities are known or can be obtained from any prior analysis, a set of Π-products and scaling laws can be derived. However, from a physical point of view it is necessary to properly choose the free quantities in order to validate the Π-products. This can be an iterative process [24].

3.1.2 Similitude theory applied to governing equations of the 2-DoF oscillator

STAGE requires three steps to derive the scaling laws

1. derive the governing equations of the parent and of the replica,
2. introduce scaling factors, see Eq. (2.23),
3. derive the scaling laws by assuming that the governing equations of the parent and of the replica are proportional, see Eq. (2.16).

The governing equations of a parent 2-DoF oscillator are given from NEWTON'S second law

$$m_1^{(\mathrm{p})}\ddot{u}_1^{(\mathrm{p})} + d_1^{(\mathrm{p})}\left(\dot{u}_1^{(\mathrm{p})} - \dot{u}_2^{(\mathrm{p})}\right) + k_1^{(\mathrm{p})}\left(u_1^{(\mathrm{p})} - u_2^{(\mathrm{p})}\right) = F^{(\mathrm{p})}\left(\tau^{(\mathrm{p})}\right), \tag{3.7}$$

$$\begin{aligned} m_2^{(\mathrm{p})}\ddot{u}_2^{(\mathrm{p})} + d_1^{(\mathrm{p})}\left(\dot{u}_2^{(\mathrm{p})} - \dot{u}_1^{(\mathrm{p})}\right) + k_1^{(\mathrm{p})}\left(u_2^{(\mathrm{p})} - u_1^{(\mathrm{p})}\right) \\ + d_2^{(\mathrm{p})}\dot{u}_2^{(\mathrm{p})} + k_2^{(\mathrm{p})}u_2^{(\mathrm{p})} = 0. \end{aligned} \tag{3.8}$$

A scaled replica will also satisfy Eqs. (3.7) and (3.8). Thus, its governing equations read in analogy

$$m_1^{(\mathrm{r})}\ddot{u}_1^{(\mathrm{r})} + d_1^{(\mathrm{r})}\left(\dot{u}_1^{(\mathrm{r})} - \dot{u}_2^{(\mathrm{r})}\right) + k_1^{(\mathrm{r})}\left(u_1^{(\mathrm{r})} - u_2^{(\mathrm{r})}\right) = F^{(\mathrm{r})}\left(\tau^{(\mathrm{r})}\right), \tag{3.9}$$

$$\begin{aligned} m_2^{(\mathrm{r})}\ddot{u}_2^{(\mathrm{r})} + d_1^{(\mathrm{r})}\left(\dot{u}_2^{(\mathrm{r})} - \dot{u}_1^{(\mathrm{r})}\right) + k_1^{(\mathrm{r})}\left(u_2^{(\mathrm{r})} - u_1^{(\mathrm{r})}\right) \\ + d_2^{(\mathrm{r})}\dot{u}_2^{(\mathrm{r})} + k_2^{(\mathrm{r})}u_2^{(\mathrm{r})} = 0. \end{aligned} \tag{3.10}$$

Each quantity in Eqs. (3.9) and (3.10) can be expressed in terms of its homologous quantity in Eqs. (3.7) and (3.8) multiplied by a scaling factor according to Eq. (2.23). Due to the principle of homology, the scaling factor of the displacements are equal, i.e., $\phi_{u_1} = \phi_{u_2} = \phi_u$ [4]. Inserting all scaling factors into Eqs. (3.9) and (3.10) and rearranging them yields

$$\begin{aligned} \left(\frac{\phi_{m_1}\phi_u}{\phi_\tau^2}\right) m_1^{(\mathrm{p})}\ddot{u}_1^{(\mathrm{p})} + \left(\frac{\phi_{d_1}\phi_u}{\phi_\tau}\right) d_1^{(\mathrm{p})}\left(\dot{u}_1^{(\mathrm{p})} - \dot{u}_2^{(\mathrm{p})}\right) \\ + \left(\phi_{k_1}\phi_u\right) k_1^{(\mathrm{p})}\left(u_1^{(\mathrm{p})} - u_2^{(\mathrm{p})}\right) = \phi_F F^{(\mathrm{p})}\left(\phi_\tau t^{(\mathrm{p})}\right) \end{aligned} \tag{3.11}$$

and

$$\begin{aligned} \left(\frac{\phi_{m_2}\phi_u}{\phi_\tau^2}\right) m_2^{(\mathrm{p})}\ddot{u}_2^{(\mathrm{p})} + \left(\frac{\phi_{d_1}\phi_u}{\phi_\tau}\right) d_1^{(\mathrm{p})}\left(\dot{u}_2^{(\mathrm{p})} - \dot{u}_1^{(\mathrm{p})}\right) + \left(\phi_{k_1}\phi_u\right) k_1^{(\mathrm{p})} \\ \cdot\left(u_2^{(\mathrm{p})} - u_1^{(\mathrm{p})}\right) + \left(\frac{\phi_{d_2}\phi_u}{\phi_\tau}\right) d_2^{(\mathrm{p})}\dot{u}_2^{(\mathrm{p})} + \left(\phi_{k_2}\phi_u\right) k_2^{(\mathrm{p})}u_2^{(\mathrm{p})} = 0. \end{aligned} \tag{3.12}$$

Complete similitude is achieved if Eqs. (3.11) and (3.12) are proportional to Eqs. (3.7) and (3.8), respectively [20]. This requires the scaling factors to be

$$\frac{\phi_{m_1}\phi_u}{\phi_\tau^2} = \frac{\phi_{d_1}\phi_u}{\phi_\tau} = \phi_{k_1}\phi_u = \frac{\phi_{m_2}\phi_u}{\phi_\tau^2} = \frac{\phi_{d_2}\phi_u}{\phi_\tau} = \phi_{k_2}\phi_u = \phi_F. \tag{3.13}$$

Eq. (3.13) represents the scaling laws of the 2-DoF oscillator. Note that STAGE can be applied to the governing equations without solving them. Setting $\phi_F = \phi_\tau = 1$ and resubstituting $\phi_u = \phi_{u_1} = \phi_{u_2}$ yields

$$\phi_{m_1} = \phi_{m_2} = \phi_{k_1} = \phi_{k_2} = \phi_{d_1} = \phi_{d_2} = \phi_{u_1}^{-1} = \phi_{u_2}^{-1}. \tag{3.14}$$

The scaling law given by Eq. (3.14) equals that from DA, see Eq. (3.6), which has been expected. On the one hand, STAGE requires prior knowledge of the 2-DoF oscillator in terms of governing equations, while a list of relevant quantities suffices to perform a DA. On the other hand, STAGE is a unique procedure since it works directly with the governing equations, while DA is ambiguous due to the fact that the free quantities need to be chosen appropriately.

3.2 Sensitivity analysis

This section illustrates how LSA and GSA methods are used to derive metamodels of the 2-DoF oscillator, which is considered a *black box* during SA. The commonalities and differences of both SA methods are illustrated and the metamodels are compared to the scaling laws obtained from similitude analysis. The design parameter set

$$\mathbf{X} = \left[m_1, m_2, k_1, k_2, d_1, d_2, \hat{F}\right] \tag{3.15}$$

of the 2-DoF oscillator is given from Figure 3.1. The force $F(\tau)$ is considered harmonic and is characterized by its magnitude $\hat{F}$. The responses are the displacements u_1 and u_2. They are the solutions of the governing equations (3.7) and (3.8), which are solved by a modal approach that is described in Appendix A.2. For simplicity, only the sum of displacements at the fundamental frequency f_1 is considered the response

$$\mathbf{Y} = [u_1(f_1) + u_2(f_1)] \equiv u_f. \tag{3.16}$$

Table 3.1 lists the design parameter values of the parent[2] 2-DoF oscillator. The damping is considered proportional to the stiffness, i.e., $d_1 = \delta k_1$ and $d_2 = \delta k_2$. Figure 3.2 illustrates the frequency response function $u(f) = u_1(f) + u_2(f)$. The fundamental frequency and the corresponding displacement u_f are marked as dotted lines. Note that f_1 is not located at the displacement maximum due to the damping.

Table 3.1: design parameters of the parent 2-DoF oscillator

design parameter	value	unit
m_1	1.0	kg
m_2	10.0	kg
k_1	5.0	$\mathrm{N\,m^{-1}}$
k_2	25.0	$\mathrm{N\,m^{-1}}$
δ	0.1	s
$\hat{F}$	1.0	N

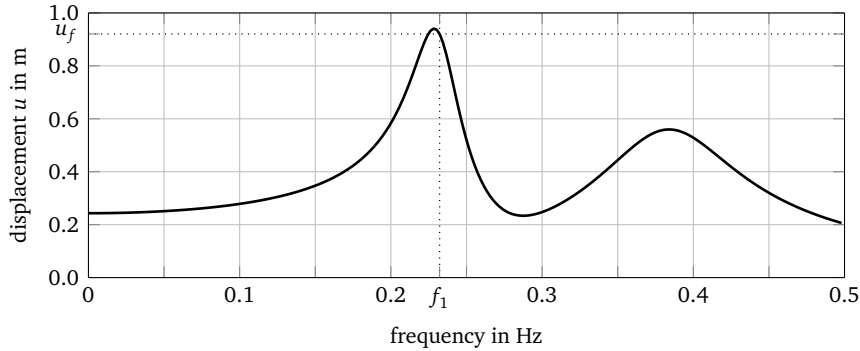

Figure 3.2: frequency response function of the parent 2-DoF oscillator

[2] The *parent* is the reference 2-DoF oscillator. The term is used in agreement with similitude analysis.

3.2.1 Local sensitivity analysis

The LSA of the 2-DoF oscillator comprises the following steps

1. alter one design parameter around the parent value listed in Table 3.1,
2. solve Eqs. (3.7) and (3.8) and obtain the displacement u_f,
3. calculate the sensitivity according to Eq. (2.30).

The steps are repeated until all sensitivities are calculated. The total number of calculations equals 12. The design parameter perturbation should not exceed 5%, but a minimum perturbation is required due to machine precision [5]. In order to find an appropriate perturbation, several LSA are performed with perturbations between ±0.5% and ±5%. A perturbation of ±2% is found sufficient to calculate all sensitivities of the 2-DoF oscillator. Finding such a sufficient perturbation by iteration is necessary unless another sensitivity calculation method is used instead of the central difference scheme [5].

Figure 3.3 shows the sensitivities $S_{j,u_f}^{(\mathrm{LSA})}$ of the displacement u_f with respect to the design parameters. A high sensitivity magnitude $|S_{j,u_f}^{(\mathrm{LSA})}|$ indicates the importance of the design parameters with respect to the displacement u_f. The damping δ has the highest effect on the displacement u_f, while the effects of the remaining parameters are much smaller. Thus, the damping is considered the most important design parameter. A positive sign of the sensitivities $S_{j,u_f}^{(\mathrm{LSA})}$ states that an increase of the design parameter causes the displacement u_f to increase, while a negative sign causes it to decrease. For example, increasing the damping δ decreases the displacement u_f, which can be expected. Thus, based on the sensitivities shown in Figure 3.3, the design parameters can be prioritized by their sensitivity magnitude, and their *direction* of influence is determined by the sensitivity sign. However, the sensitivities may differ if an LSA is performed for another parent 2-DoF oscillator [5].

A meta-model (hereafter referred to as LSA meta-model) is derived by introducing the sensitivities $S_{j,u_f}^{(\mathrm{LSA})}$ into Eq. (2.28). The LSA meta-model predicts the displacement u_f for an altered (or *scaled*) set of design parameters. Since only the first order sensitivities are taken into account only linear changes of the displacement u_f are accurately predicted by the LSA meta-model. Although

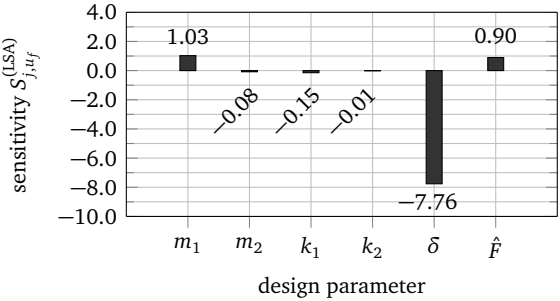

Figure 3.3: local sensitivities of the displacement u_f

the LSA meta-model is valid for a maximum design parameter perturbation of ±2% only, this maximum perturbation is exceeded in order to demonstrate the limits of the LSA meta-model with respect to the solution of the governing equations (3.7) and (3.8) and with respect to the scaling law derived from similitude analysis, see Eq. (3.14). The design parameters m_1, m_2, k_1, k_2 are perturbed (or *scaled*) by factors $\phi = 0.8 \ldots 1.2$. The damping δ and the force magnitude $\hat{F}$ are kept, i.e., $\phi_\delta = \phi_{\hat{F}} = 1$. The scaling factors are chosen in agreement with the similitude analysis in Section 3.1 to ensure complete similitude conditions for the LSA meta-model as well.

Figure 3.4 illustrates the displacement u_f calculated from the governing equations, predicted by the LSA meta-model, and scaled by the scaling law versus the scaling factor ϕ. The calculated displacement and the scaled displacement

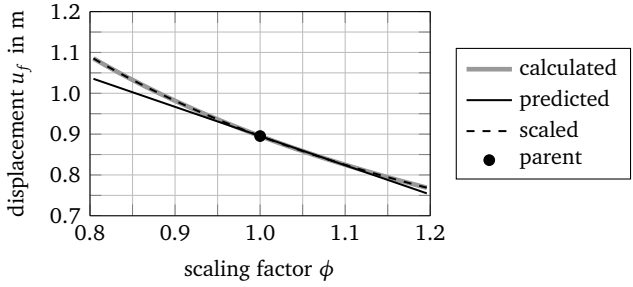

Figure 3.4: calculated, predicted, and scaled displacement u_f versus scaling factor ϕ

are identical, whereas the predicted displacement more and more deviates from the calculated displacement the more the scaling factor ϕ differs from one. The scaling law exactly reflects the scaling behavior of the 2-DoF oscillator, whereas the LSA meta-model is a linearization of the parent 2-DoF oscillator. Thus, it exactly predicts the displacement of the parent 2-DoF oscillator only. The LSA meta-model can be improved by taking higher order sensitivities into account for the TAYLOR series expansion, which is an iterative process.

3.2.2 Global sensitivity analysis

The GSA of the 2-DoF oscillator comprises the following steps

1. sample the design parameter space of the design parameters listed in Table 3.1 and choose the number of samples,
2. calculate the displacement u_f at each sample point,
3. fit a regression model and calculate the sensitivities.

The parameter space spans a range of $0.8\mathbf{X}$ through $1.2\mathbf{X}$, see Table 3.2, to allow for comparing the results of GSA and LSA. Finding an appropriate sampling technique and number of samples is an iterative process [75]. For the 2-DoF oscillator 1 000 uniformly distributed samples are required. They are obtained from a quasi-random SOBOL' sequence [73, 83, 84]. The computational effort for GSA is two orders of magnitude higher than that for LSA, which is common for GSA [5]. The regression analysis fits the linear model in Eq. (2.31) to the displacement u_f using least squares. The sensitivities $S_{j,u_f}^{(\mathrm{GSA})}$ are the standardized regression coefficients β_{j,u_f} given by Eq. (2.32).

Table 3.2: design parameter space for the GSA of the 2-DoF oscillator

design parameter	$\phi = 0.8$	$\phi = 1.0$ **(parent)**	$\phi = 1.2$	**unit**
m_1	0.80	1.00	1.20	kg
m_2	8.00	10.00	12.00	kg
k_1	4.00	5.00	6.00	$\mathrm{N\,m^{-1}}$
k_2	20.00	25.00	30.00	$\mathrm{N\,m^{-1}}$
δ	0.08	0.10	0.12	s
$\hat{F}$	0.80	1.00	1.20	N

Figure 3.5 shows the sensitivities $S_{j,u_f}^{(\mathrm{GSA})}$. Again the design parameters can be prioritized, but the sensitivities differ from those of the LSA, cf. Figures 3.3 and 3.5. This is caused by the fact that GSA considers the global parameter space, while LSA is a local derivative at one point in the parameter space [5].

The regression model is the meta-model (hereafter referred to as GSA meta-model) that predicts the displacement u_f for a scaled set of design parameters within the limits of the design parameter space, see Table 3.2. The predicted displacement is compared with the displacement calculated from the governing equations and with the predicted displacement of the LSA meta-model, see Section 3.2.1. The design parameters m_1, m_2, k_1, k_2 are again scaled by factors between $\phi = 0.8 \ldots 1.2$, while $\phi_\delta = \phi_{\hat{F}} = 1$.

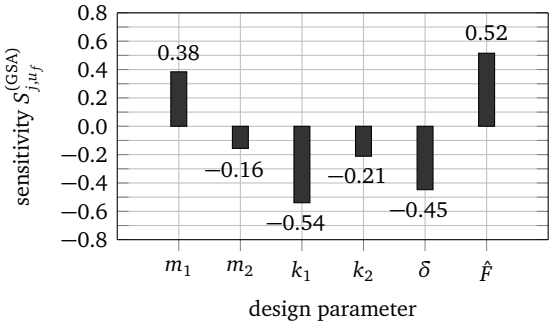

Figure 3.5: global sensitivities of the displacement u_f

Figure 3.6 illustrates the predicted and the calculated displacement u_f. The displacement u_f of the parent 2-DoF oscillator is exactly predicted by the LSA meta-model, while the displacement predicted by the GSA meta-model differs. The regression model fits with an adjusted coefficient of determination $R^2_{\mathrm{adj}} = 0.95$, see Eq. (2.33). Since $R^2_{\mathrm{adj}} \neq 1$ the regression model does not necessarily fit the calculated displacements u_f at the sample points or at other points of the design parameter space. The GSA meta-model has a minimized error in the entire parameter space in the sense of least squares, while the LSA meta-model correctly predicts the parent 2-DoF oscillator only. An improved GSA meta-model requires that higher order sensitivities are included in the regression model, which is again an iterative process.

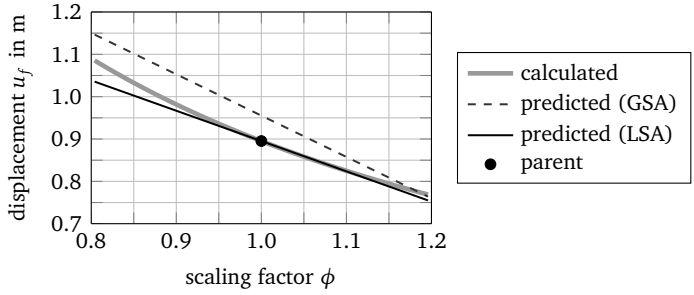

Figure 3.6: calculated and predicted displacement u_f versus scaling factor ϕ

3.3 Discussion

The findings of the previous sections are summarized and qualitatively assessed, and possible links of similitude analysis and SA methods are obtained. The DA of the 2-DoF oscillator illustrates, on the one hand, that scaling laws can be derived only based on a list of relevant quantities. On the other hand, those relevant quantities must actually be known. The relevant quantities of the 2-DoF oscillator are known, but they are not necessarily known for more complex structures in practical design engineering. It is also a challenge to validate the physical meaning of the Π-products. DA is ambiguous and deriving scaling laws becomes an iterative process. Unique scaling laws can be derived from STAGE. The scaling laws can be validated since they reflect the scaling behavior of the governing equations. However, STAGE requires that the governing equations are actually known. Thus, scaling laws cannot be derived from a *black box* model. The scaling laws derived from both similitude analysis methods are identical and they accurately predict the displacements of scaled 2-DoF oscillators in complete similitude.

LSA and GSA consider the 2-DoF oscillator a black box. The importance of design parameters as well as their direction of influence can be determined. However, LSA and GSA yield different sensitivities due to the fact that they take into account the local and the global behavior of the 2-DoF oscillator, respectively. Meta-models derived from LSA and GSA are valid in a defined range that is determined by the amount of design parameter perturbation (LSA) or by the design parameter space limits (GSA). However, the meta-models need to be iteratively refined until they are sufficiently accurate.

The similitude analysis and SA methods are qualitatively assessed by the following criteria: *low prior knowledge* required, *easy validation* of the meta-models, and *high accuracy* of the predicted responses in a *wide range* of the design parameter space. Each criterion is assessed on the relative scale − (poor), 0 (acceptable), and + (good). The assessment is shown in Table 3.3, which summarizes this chapter. DA requires the least prior knowledge, followed by both SA methods and STAGE. The scaling laws derived from DA might be hard to validate from a physical point of view, while STAGE utilizes the governing equations for this purpose. A meta-model derived from GSA can be validated based on R^2_{adj} or similar measures, while LSA lacks such measures. Both similitude analysis methods accurately predict the displacement of scaled 2-DoF oscillators in complete similitude. The LSA meta model and the GSA meta-model are found to be valid in a much smaller range or are less accurate than the scaling laws from similitude analysis even for complete similitude conditions. Based on the previously described results and the assessment in Table 3.3, three scenarios can be deduced, where similitude analysis and SA methods can be combined to use their synergies:

Table 3.3: qualitative assessment of similitude analysis and SA methods

criterion	**DA**	**STAGE**	**LSA**	**GSA**
low prior knowledge	+	−	0	0
easy validation	−	+	−	+
high accuracy	+	+	0	0
wide range	+	+	−	0

1. *Derive scaling laws of black box systems*: The design parameters that need to be scaled are known, but the system itself is considered a black box. Instead of using DA, which can be inefficient due to ambiguity, an SA can be performed to build the meta-model. The meta-model approach itself is based on similitude theory. Such a scaling method is proposed and validated in Chapter 4 for complete similitude conditions and enhanced to incomplete similitude conditions in Chapter 5.

2. *Prioritize design parameters to be used for scaling laws*: SA assesses the importance of design parameters with respect to a certain response. Important and unimportant design parameters can be distinguished based

on the sensitivity magnitude, and only important design parameters can be included in the similitude analysis to derive scaling laws. It is shown during the validation of the scaling method proposed in Chapter 4 that important design parameters are included into the scaling laws, whereas negligible design parameters are removed.

3. *Prioritize design parameters and derive scaling laws of black box systems*: It is expected that scenarios one and two are combined in practical design engineering. Section 5.2 exemplifies how scaling laws are derived for the size range of gear boxes (see Figure 1.1). Only important design parameters are used for the scaling laws, while the scaling laws themselves are derived from the method proposed in Chapters 4 and 5.

4 Similitudes and sensitivities for complete similitude conditions

In this chapter a scaling method is developed that directly derives scaling laws from virtual models, e.g., FE models, by combining similitude analysis and SA. The scaling method is proposed in Section 4.1 for complete similitude conditions. This corresponds to the second step of the method development shown in Figure 1.2 on page 18. In Section 4.2, the scaling laws for the natural frequencies and the MSTA, see Eq. (2.10), of rectangular plates are derived from virtual simulations using LSA and GSA. They are verified by comparing them to scaling laws from literature and validated by replicating the natural frequencies and the MSTA of scaled rectangular plates. An experimental simulation validates that the scaling laws derived from virtual simulations can be used to replicate natural frequencies and MSTA obtained from experimental simulations as well. In Section 4.3, the scaling laws of a simplified car undercarriage are derived in virtual simulations using LSA. The scaling laws are used to replicate the driving point admittance and the vibration velocities at an arbitrarily chosen receiver point. Besides the geometrical dimensions the material properties are scaled as well, but complete similitude conditions are still kept.

4.1 Scaling laws from similitude and sensitivity analyses

Consider an arbitrary parent structure and its scaled replica as shown in Figure 4.1. The parent's design parameters $X_j^{(\mathrm{p})}$ as well as the responses $Y_k^{(\mathrm{p})}$ are known from a previous simulation (virtual or experimental simulation). The replica is a scaled model of the parent, and its design parameters $X_j^{(\mathrm{r})}$ are related to those of the parent by scaling factors. A scaling factor for the response $Y_k^{(\mathrm{r})}$ can be defined in analogy. Thus, the scaling factors read

$$\phi_{X_j} = \frac{X_j^{(\mathrm{r})}}{X_j^{(\mathrm{p})}} \quad \text{and} \quad \phi_{Y_k} = \frac{Y_k^{(\mathrm{r})}}{Y_k^{(\mathrm{p})}}. \tag{4.1}$$

Equation (2.15) can be rewritten as

$$\mathfrak{f}\left(\phi_{X_1}, \phi_{X_2}, \ldots, \phi_{X_N}, \phi_{Y_1}, \phi_{Y_2}, \ldots, \phi_{Y_M}\right) = 0, \tag{4.2}$$

where N and M denote the number of design parameters and responses, respectively.

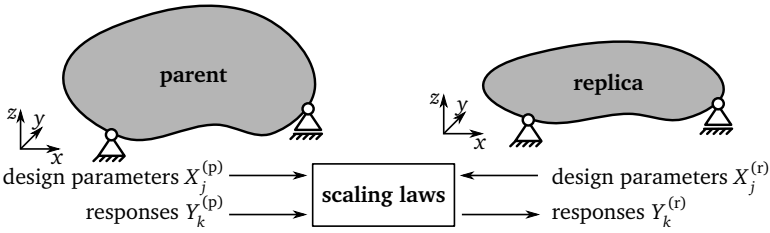

Figure 4.1: scheme of scaling laws applied to an arbitrary structure [85]

It is assumed that

1. the parent and the replica are in complete similitude, i.e.,
   - the mode shape order is kept and
   - the damping remains the same [21, 22],
2. the scaling factors ϕ_{X_j} are linearly independent, and
3. the responses are continuous.

The scaling factor ϕ_{Y_k} of a response Y_k can then be obtained from a power law

$$\phi_{Y_k} = \prod_{j=1}^{N} \left(\phi_{X_j}\right)^{\alpha_{j,k}}. \tag{4.3}$$

The validity of this approach is illustrated in [85] and the following derivations are also based on that paper. Equation (4.3) is directly deduced from the Π-theorem of BUCKINGHAM [19]. Scaling laws obtained from DA, STAGE, or

SAMSARA are power laws as well provided that complete similitude conditions persist [4, 22, 32–34, 39, 57–59]. Logarithmizing Eq. (4.3)

$$\ln\left(\phi_{Y_k}\right) = \sum_{j=1}^{N} \alpha_{j,k} \ln\left(\phi_{X_j}\right) \tag{4.4}$$

and inserting the substitutions

$$Y'_k = \ln\left(\phi_{Y_k}\right), \tag{4.5}$$

$$b'_{j,k} = \alpha_{j,k}\,, \tag{4.6}$$

$$X'_j = \ln\left(\phi_{X_j}\right) \tag{4.7}$$

yields a linear equation

$$Y'_k = \sum_{j=1}^{N} b'_{j,k} X'_j. \tag{4.8}$$

Comparing Eq. (4.8) with the second summand of Eq. (2.28) or with the second summand of Eq. (2.31) shows that the coefficient $b'_{j,k}$ equals a first order sensitivity

$$b'_{j,k} = S_{j,k} = \frac{\partial Y'_k}{\partial X'_j} \tag{4.9}$$

or a regression coefficient

$$b'_{j,k} = \beta_{j,k} \tag{4.10}$$

of a linear regression model, respectively. Resubstituting the variables in Eqs. (4.9) and (4.10) by those of Eqs. (4.5) through (4.7) yields

$$\alpha_{j,k} = \frac{\partial \ln\left(\phi_{Y_k}\right)}{\partial \ln\left(\phi_{X_j}\right)} \tag{4.11}$$

and

$$\alpha_{j,k} = \beta_{j,k}. \tag{4.12}$$

Each scaling factor ϕ_{X_j} in Eq. (4.3) is weighted by a power $\alpha_{j,k}$ that can either be obtained from an LSA (Eq. (4.11)) or from a GSA (Eq. (4.12)). The central difference approximation of Eq. (4.11) reads

$$\alpha_{j,k} \approx \frac{\ln\left(Y_k^{(+)}\right) - \ln\left(Y_k^{(-)}\right)}{\ln\left(\phi_{X_j}^{(+)}\right) - \ln\left(\phi_{X_j}^{(-)}\right)}. \tag{4.13}$$

$\phi_{X_j}^{(+)}$ and $\phi_{X_j}^{(-)}$ denote a slight scale-up and scale-down of the parameter X_j during the LSA, respectively, and $Y_k^{(+)}$ and $Y_k^{(-)}$ are the corresponding responses. The powers are calculated from Eq. (4.13) in all subsequent LSA due to its simple implementation [5, 65]. The proposed scaling method can be characterized as follows:

- The power law in Eq. (4.3) is based on similitude theory, whereas the powers $\alpha_{j,k}$ are obtained from LSA or GSA. On the one hand, the iterative meta-modeling process within SA (e.g., choosing an appropriate regression model) becomes redundant due to the power law that is motivated by similitude theory. On the other hand, the unknown powers $\alpha_{j,k}$ are directly calculated from an SA instead of manually derived by one of the similitude analysis methods discussed in Section 2.2. The proposed scaling method actually combines similitude analysis with SA. Scaling laws can directly be derived from virtual models without prior knowledge of their scaling behavior as will be subsequently demonstrated.

- The powers $\alpha_{j,k}$ can be read as sensitivities. The power magnitude $|\alpha_{j,k}|$ indicates the importance of the corresponding design parameter, while the sign determines the direction of influence, as illustrated in Section 3.2 for the 2-DoF oscillator. Particularly, a zero power indicates that a response is independent from the corresponding design parameter, since $\phi_{X_j}^0 = 1$. Consequently, such a design parameter can be removed from the scaling law.

- During the SA it must be ensured that neither the design parameters nor the responses yield zero due to the logarithm in Eq. (4.13). In order to avoid zeros in the logarithm the design parameters need to be chosen appropriately or a constant offset can be added to the model. Within GSA, all samples need to be checked as well.

4.2 Scaling laws of vibrating rectangular plates

The proposed scaling method is verified and validated by applying the method to vibrating rectangular plates. Section 4.2.1 introduces the parent rectangular plate with simply supported edges, the considered vibration responses, and the virtual models. Section 4.2.2 verifies the proposed scaling methods regarding various virtual models, various SA methods, and various boundary conditions of the rectangular plates. It is expected that scaling laws derived from the proposed scaling method equal those from literature. Section 4.2.3 validates the scaling laws by comparing replicated and calculated vibration responses that are obtained from virtual simulations. A-posteriori measures are proposed to assess whether complete similitude conditions persist for the scaled rectangular plates. Section 4.2.4 validates the scaling laws by applying them to measured vibration responses obtained in experimental simulations.

4.2.1 Virtual models of the parent rectangular plate

A parent rectangular plate made from aluminum is considered, where all edges are simply supported (*SSSS*). The length, the width, and the thickness equal 870 mm, 620 mm, and 5 mm, respectively. The dimensions equal those of the parent rectangular plate that is used for the experimental validation and the material properties are obtained from measurements of this parent rectangular plate as well, see Section 4.2.4. A dynamic excitation force of 1 N magnitude acting at the dimensionless coordinate (a_F, b_F) causes the parent rectangular plate to vibrate. Table 4.1 lists all design parameters of the parent rectangular plate.

The first 100 natural frequencies (or modes) and the MSTA are considered the vibration responses. Two virtual models are used to calculate the vibration responses. The *analytical model* uses Eqs. (2.6) and (2.11) and is based on KIRCHHOFF-LOVE plate theory [11, 12]. Scaling laws of the analytical model are already known from literature such as [9, 22]. The analytical model serves as a reference to verify the scaling method proposed in the previous section. Since the analytical model is a modal summation approach, the first 200 modes are used during the calculation in order to reduce the truncation error, but only the first 100 modes are actually analyzed. The *FE model* is based on MINDLIN-REISSNER plate theory [13, 14]. Scaling laws have not been directly derived from FE models yet. Thus, the FE model serves as the first test case to

Table 4.1: design parameters of the parent rectangular plate

parameter	symbol	value	unit
length	$a^{(\mathrm{p})}$	870	mm
width	$b^{(\mathrm{p})}$	620	mm
thickness	$t^{(\mathrm{p})}$	5	mm
excitation position	$a_{\mathrm{F}}^{(\mathrm{p})}/a^{(\mathrm{p})}$	0.885	–
excitation position	$b_{\mathrm{F}}^{(\mathrm{p})}/b^{(\mathrm{p})}$	0.161	–
excitation magnitude	$\hat{F}^{(\mathrm{p})}$	1	N
YOUNG's modulus	$E^{(\mathrm{p})}$	$70.59 \cdot 10^9$	$\mathrm{N\,m^{-2}}$
POISSON's ratio	$\mu^{(\mathrm{p})}$	0.33	–
mass density	$\rho^{(\mathrm{p})}$	2 676	$\mathrm{kg\,m^{-3}}$
loss factor	$\eta^{(\mathrm{p})}$	0.005	–

verify and validate the scaling method proposed in the previous section. The natural frequencies are calculated from a modal analysis [86], while the MSTA is obtained from the direct solution of the full system matrices [87] as well as Eqs. (2.9) and (2.10). The FE model uses a structured mesh with a minimum of 12 SHELL281 elements [87] per flexural wavelength up to the 100th mode. The FE model setup is described in detail in Appendix B.1. In order to reduce calculation time, both models use *frequency clustering* [87], which narrows the frequency spacing in the vicinity of natural frequencies and widens it between them. Frequency clustering requires the loss factor and an integer constant, which are set to 0.005 (see Table 4.1) and the default value 4 [87], respectively.

Figure 4.2 illustrates the MSTA levels of the parent rectangular plate calculated from the analytical model and from the FE model. The level reference equals $(v_0/F_0)^2 S_0 = 6.25 \cdot 10^{-6}\,\mathrm{m^4\,N^{-2}\,s^{-2}}$, where $v_0 = 5 \cdot 10^{-8}\,\mathrm{m\,s^{-1}}$, $F_0 = 2 \cdot 10^{-5}\,\mathrm{N}$, and $S_0 = 1\,\mathrm{m^2}$ are the reference values of the velocity, the force, and the surface area, respectively [88]. The peaks of the MSTA levels are located at natural frequencies, which can be expected due to the small loss factor of $\eta = 0.005$. Between two natural frequencies the MSTA levels are significantly lower, e.g., the MSTA level between the fundamental frequency $f_{1,1} = 48.48\,\mathrm{Hz}$ and the second peak is 40 dB lower than the MSTA level at the fundamental frequency. The natural frequencies and the MSTA levels of both models agree well. However, minor deviations occur at frequencies above 1.75 kHz. The natural frequencies of the analytical model are approximately 1.43% higher

than those of the FE model and the maximum level difference of the MSTA equals 3.7 dB. Taking into account that engineers in practice need to choose an appropriate virtual model for their purpose, the aforementioned deviations are considered characteristic deviations between different virtual models. Thus, valid scaling laws for practical design engineering should replicate the vibration responses with a similar accuracy.

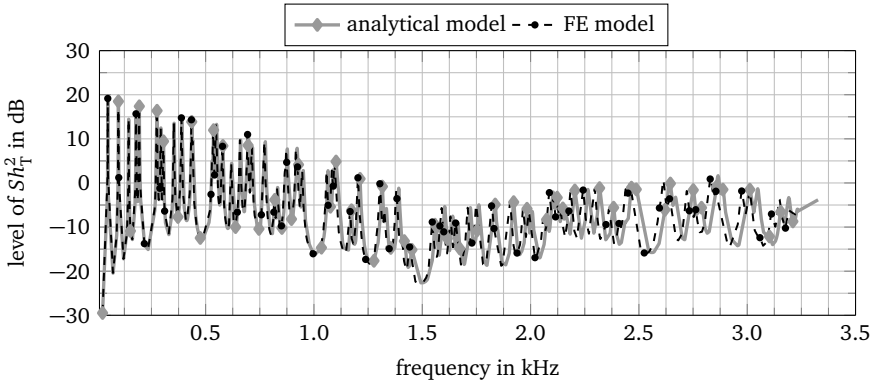

Figure 4.2: MSTA level of the parent rectangular plate with simply supported edges versus frequency (re $6.25 \cdot 10^{-6}\,\mathrm{m^4\,N^{-2}\,s^{-2}}$)

4.2.2 Derivation and verification of scaling laws for rectangular plates

The rectangular plate is scaled in its geometrical dimensions a, b, and t. The analytical model keeps complete geometrical similitude conditions if length and width are scaled by a different factor than the thickness [31]. As can be seen from Eqs. (2.6) and (2.11) only length and width occur in different summands, whereas the thickness can be factored out. Thus, a common scaling factor ϕ_l is required for length and width only in order to achieve complete similitude conditions, while a different scaling factor ϕ_t for the thickness does not affect the similitude of length and width. Such considerations can hardly be made for the FE model, and its complete similitude conditions need to be proven. Thus, the scaling laws of the natural frequencies and of the MSTA are established as follows

$$\frac{f_{m,n}^{(\mathrm{r})}}{f_{m,n}^{(\mathrm{p})}} = \phi_{f_{m,n}} = \phi_l^{\alpha_{l,f}}\,\phi_t^{\alpha_{t,f}} \tag{4.14}$$

and

$$\frac{Sh_{\mathrm{T}}^{2\,(\mathrm{r})}}{Sh_{\mathrm{T}}^{2\,(\mathrm{p})}} = \phi_{Sh} = \phi_l^{\alpha_{l,Sh}} \phi_t^{\alpha_{t,Sh}}. \tag{4.15}$$

The scaling laws derived from Eqs. (4.14) and (4.15) are verified in two steps. First, the powers $\alpha_{l,f}$, $\alpha_{t,f}$, $\alpha_{l,Sh}$, and $\alpha_{t,Sh}$ are obtained for simply supported rectangular plates from

- the analytical model (LSA and GSA),
- the FE model with SHELL281 elements built in ANSYS (LSA and GSA),
- another FE model with SHELL63 elements built in ANSYS (LSA), and
- another FE model with S8R elements built in ABAQUS (LSA).

The analytical model serves as a reference to verify the scaling laws derived from the different FE models and SA methods. SHELL281 elements and S8R elements consider shear deformations, while shear deformations can be neglected by using SHELL63 elements. Comparing the scaling laws derived from the FE model with SHELL281 elements and the FE model with SHELL63 elements shows the effect of shear deformations on the scaling laws. Comparing the scaling laws derived from the FE model with SHELL281 elements and the FE model with S8R elements verifies the scaling method among different software packages. It is expected that the scaling laws derived from the different virtual models and from LSA or GSA are identical to scaling laws from literature.

Second, scaling laws are derived from the FE model with SHELL281 elements using LSA for

- a rectangular plate with all edges simply supported (*SSSS*),
- a rectangular plate with all edges clamped (*CCCC*),
- a rectangular plate all edges free (*FFFF*), and
- a cantilever plate (*CFFF*).

These boundary conditions are common in vibroacoustic analyses, and scaling laws are derived for such plates, e.g., for a plate with *CFFF* boundary condition [57, 81]. It is expected that the vibration behavior is significantly affected by the boundary conditions, but the scaling laws should not be affected.

During the SA, only the natural frequencies are chosen as frequency steps to reduce calculation time. Each scaling factor is altered by ±2% during LSA, which is obtained from [85]. The design parameter space of GSA spans $\phi_l = 0.5 \ldots 2.5$ and $\phi_t = 0.5 \ldots 2.5$ according to typical geometrical scaling factors in vibroacoustics [21, 22, 53, 54, 57]. GSA uses a quasi-random sampling technique based on a HALTON number sequence [72] and assumes uniformly distributed scaling factors ϕ_l and ϕ_t [75]. LSA requires 4 calculations, while 5 calculations are found sufficient for GSA [75].

Verification of scaling laws among virtual models and SA methods

The powers $\alpha_{l,f}$, $\alpha_{t,f}$, $\alpha_{l,Sh}$, and $\alpha_{t,Sh}$ of the analytical model obtained from both LSA and GSA equal -2, 1, 2, and -4, respectively, at the first 100 natural frequencies. The regression model within GSA is fitted with $R^2_{\text{adj}} = 1$, i.e., the linear regression model exactly fits the sampling points. The powers are in exact agreement with those of the scaling laws from literature, e.g., [22]. Thus, the proposed scaling method is verified for the analytical model.

The powers calculated from the FE model with SHELL281 elements slightly vary with frequency and depend on the SA method, see Figure 4.3. The subsequent analysis discusses the deviations between the analytical model and the FE model first, while the deviations due to the SA methods are discussed afterwards. The powers $\alpha_{l,f}$ and $\alpha_{t,f}$ slightly increase and decrease, respectively, for an increasing frequency. The powers $\alpha_{l,Sh}$ and $\alpha_{t,Sh}$ agree well with those of the analytical model up to approximately 2 kHz, whereas deviations occur at frequencies above 2 kHz. These deviations are caused by the fact that SHELL281 elements include shear deformations based on an *equivalent energy method* [87]. In order to prove this hypothesis, the FE model with SHELL63 elements is used to derive the scaling laws since these elements neglect shear deformations. The powers obtained from LSA are illustrated in Figure C.1 on page 163. These powers equal those of the analytical model. Thus, the deviations of the powers obtained from the FE model with SHELL281 elements from the powers obtained from the analytical model are caused by the effect of shear deformations. However, the power $\alpha_{l,Sh}$ obtained from the FE model with SHELL63 elements still deviates at some frequencies from the power of the analytical model, see Figure C.1, but to a lesser extent compared to the FE model with SHELL281 elements. This smaller deviation is caused by inaccurate sensitivities due to the fact that the FE mesh

changes if plate length and width are altered during the LSA [62]. However, the sensitivities obtained from the LSA are considered sufficiently accurate, but the proposed scaling method is limited in taking effects of shear deformations into account. Further discussion on the effect of the shear deformations on the accuracy of replicated vibration responses follows in Section 4.2.3.

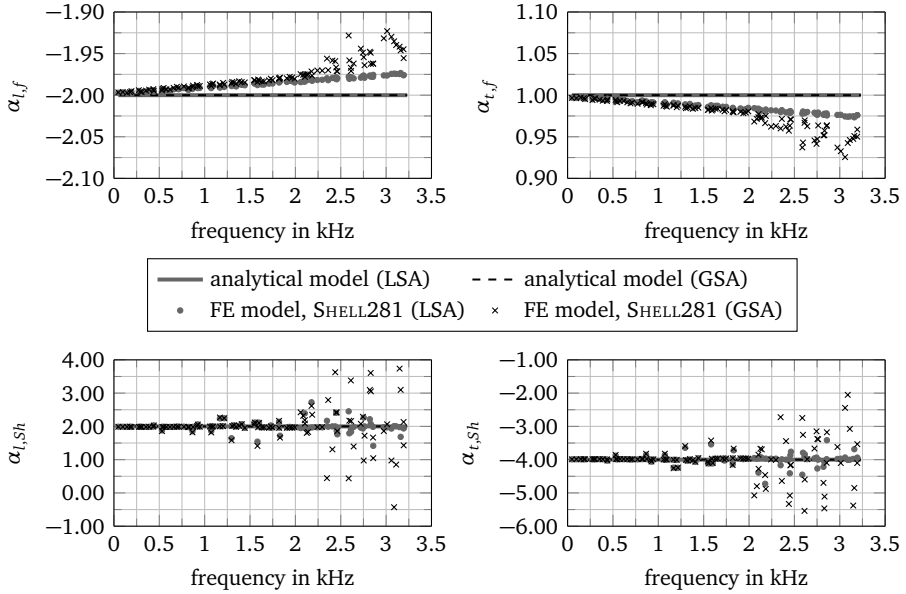

Figure 4.3: powers for the scaling laws obtained from LSA and GSA, legend refers to all plots

Comparing the powers obtained from GSA with those from LSA, Figure 4.3 shows that the powers $\alpha_{l,f}$ and $\alpha_{t,f}$ increase and decrease, respectively, to a higher extent at frequencies above 2 kHz. The regression model is fitted with $R^2_{\text{adj}} = 1$ as shown in the left part of Figure 4.4. Thus, the additional deviation of the powers $\alpha_{l,f}$ and $\alpha_{t,f}$ within GSA is rather caused by the global sampling of the parameter space than by an inaccurately fitted regression model. The regression model of the powers $\alpha_{l,Sh}$ and $\alpha_{t,Sh}$ is fitted with $R^2_{\text{adj}} = 1$ up to approximately 2 kHz as well. Above 2 kHz R^2_{adj} drops at some frequencies, i.e., the fitted regression model deviates from the sample points. As a consequence, the powers deviate from those of the LSA, see Figure 4.3.

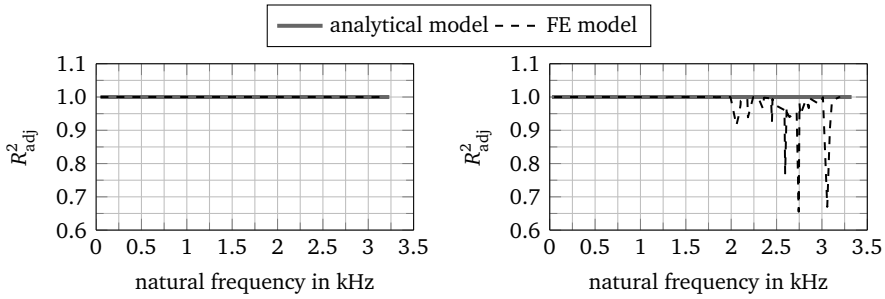

Figure 4.4: adjusted coefficient of determination R^2_{adj} versus the natural frequencies of the linear regression models, left: natural frequencies, right: MSTA

Finally, the scaling laws are derived from an LSA of the FE model with S8R elements built in ABAQUS. The powers are plotted in Figure C.2 on page 164. They agree well with those obtained from the LSA of the FE model with SHELL281 elements. This can be expected since S8R elements consider shear deformations as well [89].

In summary, the powers obtained from the FE models differ from those of the analytical model due to the fact that

1. the FE models (with SHELL281 elements and with S8R elements) take shear deformations into account,

2. GSA samples the entire parameter space,

3. the regression model of GSA is imperfectly fitted.

However, the aforementioned deviations between the powers obtained from the FE models and from the analytical model are small. Particularly, the mean powers of the scaling laws obtained from all virtual models agree well as shown in Table 4.2. Thus, the scaling laws can be approximated sufficiently well by [85]

$$\frac{f^{(\mathrm{r})}_{m,n}}{f^{(\mathrm{p})}_{m,n}} = \phi_{f_{m,n}} = \phi_l^{-2}\phi_t^1 \tag{4.16}$$

and

$$\frac{Sh_{\mathrm{T}}^{2\,(\mathrm{r})}}{Sh_{\mathrm{T}}^{2\,(\mathrm{p})}} = \phi_{Sh} = \phi_l^2 \phi_t^{-4}. \tag{4.17}$$

Equations (4.16) and (4.17) agree well with scaling laws from literature, e.g., [22]. Thus, the proposed scaling method is verified for LSA and GSA of FE models of the rectangular plate.

Table 4.2: mean values of the powers for the scaling laws, precision of the powers visualizes their difference only

power	SA method	analytical model	ANSYS SHELL281	ANSYS SHELL63	ABAQUS S8R
$\alpha_{l,f}$	LSA	−2.00	−1.99	−2.00	−1.99
	GSA	−2.00	−1.98	–	–
$\alpha_{t,f}$	LSA	+1.00	+0.99	+1.00	+0.99
	GSA	+1.00	+0.98	–	–
$\alpha_{l,Sh}$	LSA	+2.00	+1.98	−2.02	+1.98
	GSA	+2.00	+2.00	–	–
$\alpha_{t,Sh}$	LSA	−4.00	−3.98	−4.00	−3.96
	GSA	−4.00	−4.00	–	–

Verification of scaling laws among the rectangular plate's support

In the second verification step, the scaling laws are derived for rectangular plates with *CCCC*, *FFFF*, and CFFF boundary conditions from LSA of FE models with SHELL281 elements.[1] The calculated powers behave in analogy to those in Figure 4.3. Table 4.3 shows their mean values in comparison to the simply supported rectangular plates (*SSSS*). The powers agree well, thus, the scaling laws in Eqs. (4.16) and (4.17) seem to be independent from the boundary conditions. They are verified for rectangular plates with *SSSS*, *CCCC*, CFFF, and *FFFF* boundary conditions. However, a parent and a replica must have identical boundary conditions to be in complete similitude. The proposed scaling method cannot replicate the vibration responses of a replica from a parent that has different boundary conditions than the replica.

[1] Unless specified otherwise the FE models that are subsequently described are built in the FE software ANSYS.

Table 4.3: mean values of the powers for scaling laws of rectangular plates with various boundary conditions

power	*SSSS*	*CCCC*	*CFFF*	*FFFF*
$\alpha_{l,f}$	−1.99	−1.98	−1.99	−1.99
$\alpha_{t,f}$	+0.99	+0.98	+0.99	+0.99
$\alpha_{l,Sh}$	+1.98	+1.98	+2.00	+2.04
$\alpha_{t,Sh}$	−3.98	−3.98	−4.00	−4.01

4.2.3 Validation of scaling laws by virtual simulations

In order to validate the scaling laws, the natural frequencies and the MSTA of simply supported rectangular plates are obtained from FE calculations and by replicating the natural frequencies from Eq. (4.16) and the MSTA magnitudes from Eq. (4.17). The vibration responses of the analytical model are always exactly replicated by Eqs. (4.16) and (4.17) [22, 85]. Thus, this section focuses on the FE model. In particular, it is validated whether complete geometrical similitude conditions persist for the FE model if length and width are scaled by a different factor than the thickness. On the one hand, it can be expected that shear deformations more and more affect the vibration responses with increasing plate thickness. This causes mode shapes to change their order and complete similitude conditions to be violated. On the other hand, increasing the plate thickness affects the vibrations in a given frequency range in a different manner. Considering a given frequency range in terms of a certain number of natural frequencies, it can be expected that modes change their order at high mode numbers first, while the modes at low mode numbers are still in the same order. Thus, complete similitude conditions are first violated at high mode numbers. Consequently, the vibration responses at low mode numbers should still be accurately replicated by the scaling laws. At higher mode numbers some error occurs, but this might be acceptable for engineering purposes.

In order to assess the error of the replicated vibration responses, four half-scale plates are investigated, where the thickness increases step by step, see Table 4.4. The thickness ratio

$$\xi = \frac{\min(a, b)}{t} \tag{4.18}$$

is defined with respect to the minimum length (i.e., the width in this case) [85]. Replica r1 ($\phi_l = \phi_t$) is in perfect similitude to the parent and its thickness ratio $\xi^{(\mathrm{r1})} = 124$ equals that of the parent as well. The thickness ratio ξ of the replicas r2 through r4 decreases more and more to approximately 50. The shear deformations are expected to more and more affect the vibration responses in the desired frequency range, which still covers the first 100 modes.

Table 4.4: geometrical dimensions, scaling factors, and thickness ratios of the replicas

	dimensions in mm			scaling factors		
replica	a	b	t	ϕ_l	ϕ_t	ξ
r1	435	310	2.5	0.5	0.5	124.00
r2	435	310	4.0	0.5	0.8	77.50
r3	435	310	5.0	0.5	1.0	62.00
r4	435	310	6.0	0.5	1.2	51.67

Replicating the natural frequencies

The replicated natural frequencies are obtained from Eq. (4.16) and are plotted in Figure 4.5 versus the natural frequencies obtained from the FE calculation. If the data are located on the main diagonal, which is plotted as a thin solid line, the replicated natural frequencies equal those from the FE calculation. The replicated natural frequencies of replica r1 exactly match those from the FE calculation since replica r1 is in perfect similitude to the parent. The replicated natural frequencies of the replicas r2, r3, and r4 agree well up to approximately 7.8 kHz. Above this frequency the replicated natural frequencies tend to be higher than those of the FE calculation. These deviations are analyzed qualitatively and quantitatively using the modal assurance criterion (MAC) [90] and the error of the replicated natural frequencies, respectively. The MAC is defined as

$$MAC = \frac{\left| \underline{\psi}^{(\mathrm{p})H} \underline{\psi}^{(\mathrm{r})} \right|^2}{\underline{\psi}^{(\mathrm{p})H} \underline{\psi}^{(\mathrm{p})} \underline{\psi}^{(\mathrm{r})H} \underline{\psi}^{(\mathrm{r})}}, \tag{4.19}$$

where the superscript H denotes the HERMITIAN [90]. MAC measures the consistency of the mode shapes of the parent $\underline{\psi}^{(\mathrm{p})}$ and of the replica $\underline{\psi}^{(\mathrm{r})}$ in a range between zero (inconsistent) and one (consistent). The mode shape order

is equal if the MAC matrix equals the identity matrix, while a different mode shape order causes the values on the main diagonal to decrease. Thus, the mode shape order can be assessed by exclusively analyzing the main diagonal of the MAC matrix.

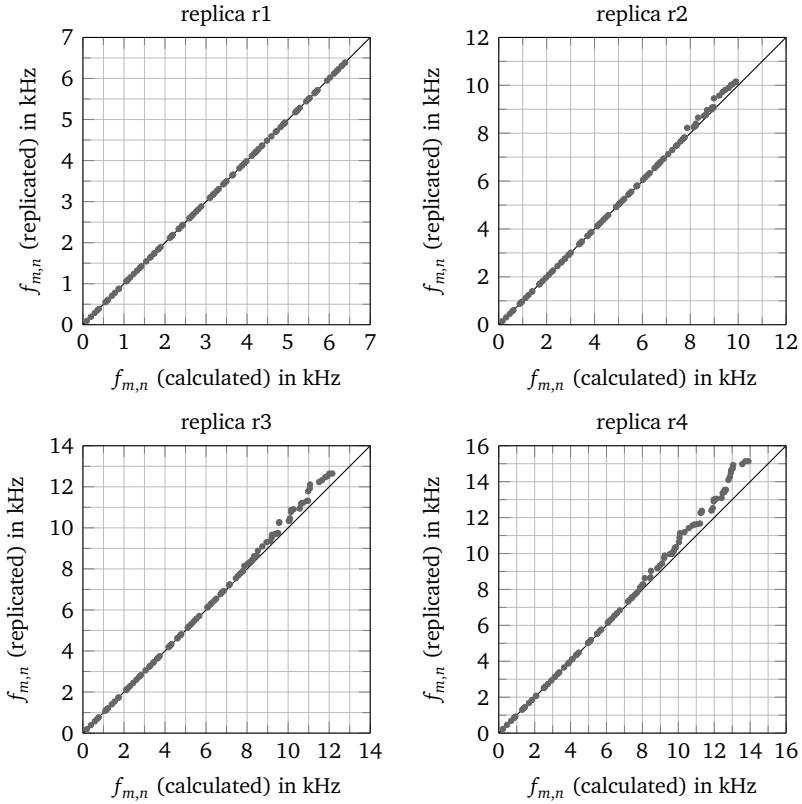

Figure 4.5: replicated natural frequencies versus calculated natural frequencies of simply supported rectangular plates

The error of the replicated natural frequencies reads

$$\varepsilon_f = \left| \frac{f_{\mathrm{FE}} - f_{\mathrm{SL}}}{f_{\mathrm{FE}}} \right| \cdot 100\%, \tag{4.20}$$

where the subscripts FE and SL denote the natural frequencies that are calculated (by means of FE) and replicated (by means of scaling laws, abbreviated as SL), respectively.

Figure 4.6 shows the MAC values on the main diagonal of the MAC matrices versus the mode number. The MAC matrices are plotted in Figure C.3 on page 165 for the sake of completeness. The MAC values of replica r1 equal one for the mode numbers 1 through 100 and the error ε_f equals zero. Thus, the mode shape order of replica r1 equals that of the parent and the natural frequencies are exactly replicated, which can be expected due to the perfect similitude of replica r1. The MAC values of the replicas r2, r3, and r4 drop to zero at the mode numbers 78, 61, and 51, respectively, see Figure 4.6. Each of

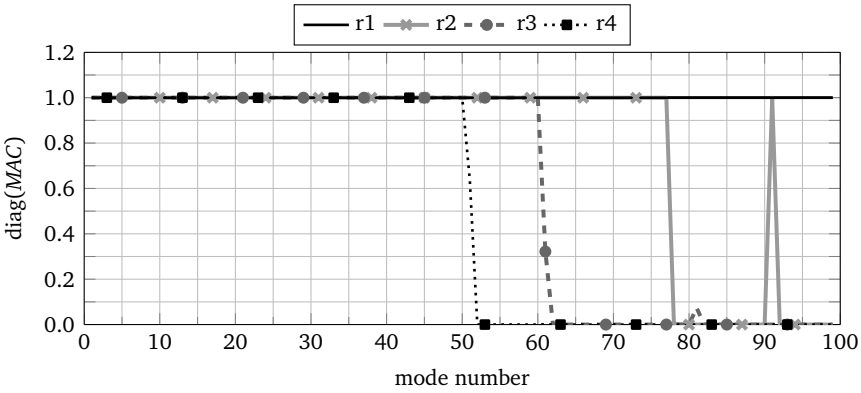

Figure 4.6: main diagonal values of the MAC matrices of the replicas r1 through r4 versus the mode number

these mode numbers corresponds to a frequency of approximately 7.8 kHz. At these mode numbers (or frequency) new mode shapes occur that correspond to none of the mode shapes of the parent. Thus, complete similitude conditions are violated at the mode numbers 78, 61, and 51, while they still persist below these mode numbers. Figure 4.7 compares the 78th mode shape of the parent with that of the replica r2. Similarly, Figures C.4 and C.5 on page 166 compare the mode shapes of the 61st and 51st mode of the parent with those of the replicas r3 and r4, respectively. The error ε_f increases above the mode numbers 78, 61, and 51 as well, see Figure 4.8. This can be expected since the mode shape order changes. The maximum values of the error ε_f equal 5.2%, 9.4%,

and 14.3% for the replicas r2, r3, and r4, respectively. However, this can still be acceptable for practical design engineering if a rough estimate of the natural frequency suffices for the desired purpose. The thickness ratio ξ should not be smaller than $\xi_{\min} = 50$ to keep the error below 15%. The same value for $\xi_{\min}$ is also found in [85], where replicas with other scaling factors are investigated.

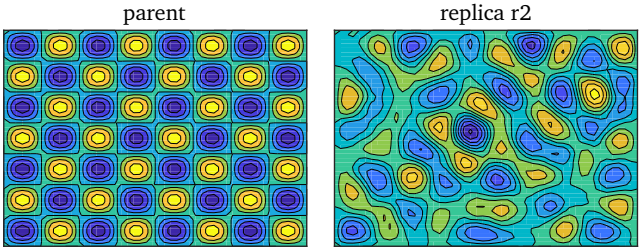

Figure 4.7: 78th mode shapes of the parent and of the replica r2 (both plates are plotted in equal size for visualization purposes only)

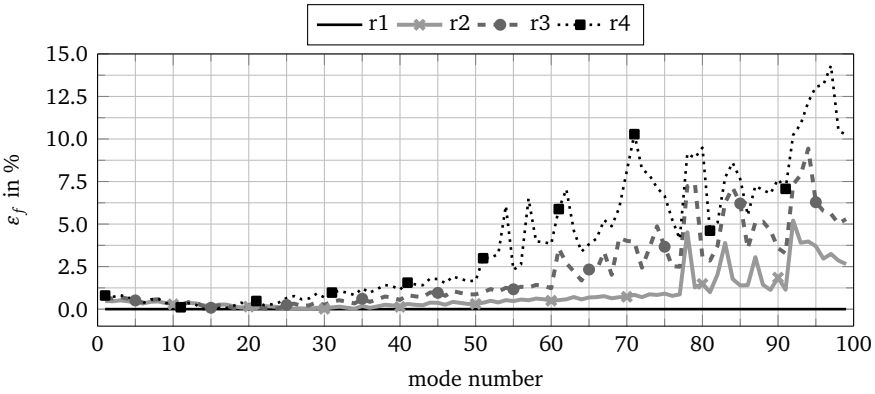

Figure 4.8: error of the replicated natural frequencies ε_f of the replicas r1 through r4 versus the mode number

From a practical point of view, plates are usually made from metal sheets that are available in certain sizes only, i.e., the scaling factor of the thickness ϕ_t takes only certain values as well. Based on the minimum thickness ratio $\xi_{\min} = 50$ and the scaling factor of the thickness ϕ_t, the minimum permissible scaling factor for length and width yields

$$\phi_{l,\min} = \frac{\xi_{\min}}{\xi^{(\mathrm{p})}} \phi_t = \frac{50}{\xi^{(\mathrm{p})}} \phi_t, \tag{4.21}$$

where $\xi^{(\mathrm{p})}$ denotes the thickness ratio of the parent.

Replicating the mean squared transfer admittance

Figures 4.9 through 4.12 illustrate the replicated MSTA and that from the FE calculations for the replicas r1 through r4. The frequency axis is replicated from Eq. (4.16). The MSTA magnitudes are replicated from Eq. (4.17) and the levels are calculated. The replicated MSTA levels of replica r1 agree well with those of the FE calculation, which can again be expected due to the perfect similitude. The replicated MSTA levels of the replicas r2 through r4 agree well up to the mode numbers 78, 61, and 51, respectively (or approximately 7.8 kHz), while deviations occur above 7.8 kHz. This can be expected taking into account the previous discussion on replicated natural frequencies. In order to assess the accuracy of the replicated MSTA levels the level difference is introduced

$$\Delta L_{Sh}\left(f_{m,n}\right) = \left| L_{Sh,\mathrm{FE}}\left(f_{m,n}\right) - L_{Sh,\mathrm{SL}}\left(f_{m,n}\right) \right|. \tag{4.22}$$

The level differences are obtained at the natural frequencies $f_{m,n}$ only. The MSTA levels reach maximum values at the natural frequencies, whereas the levels between natural frequencies are much smaller. Thus, possible deviations of the replicated MSTA levels from the calculated MSTA levels are negligible between natural frequencies. Figure 4.13 on page 75 illustrates the level difference for the replicas r1 through r4. Below 7.8 kHz, the level difference of the replicas r2 through r4 is less than approximately 2.5 dB, which is smaller than the maximum level difference between the MSTA obtained from the FE model and from the analytical model (see page 61). Thus, the MSTA levels of the replicas r2 through r4 can be replicated sufficiently well up to 7.8 kHz. Above 7.8 kHz the level difference increases. Due to the fact that the mode shapes of the replicas r2 through r4 differ above 7.8 Hz, the vibration behavior changes and, thus,

the MSTA levels differ as well. The maximum level differences for the replicas r1 through r4 equal $\ll$1 dB, 12.2 dB, 11.7 dB, and 14.3 dB, respectively. The maximum level differences of the replicas r2 through r4 might still be acceptable for a rough approximation of the MSTA levels above 7.8 Hz, but a more precise prediction of the MSTA levels by the scaling laws requires the parent and the replica to be in perfect similitude.

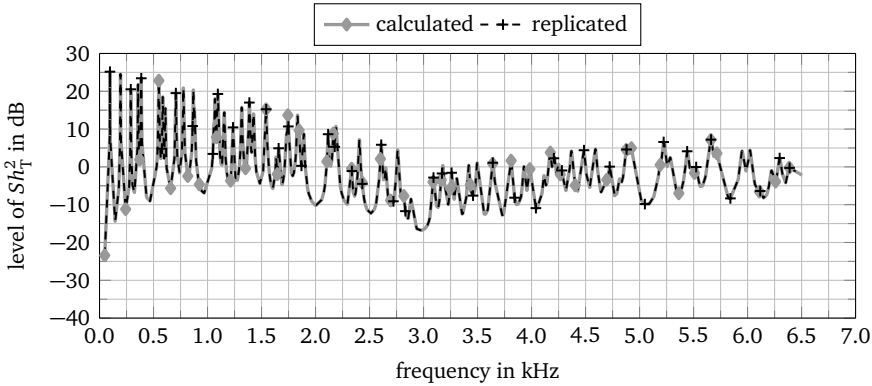

Figure 4.9: MSTA level of replica r1 versus frequency (re $6.25 \cdot 10^{-6}\,m^4\,N^{-2}\,s^{-2}$)

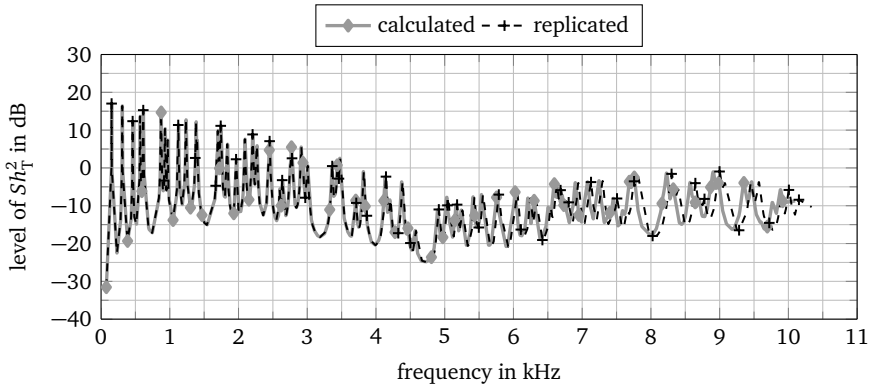

Figure 4.10: MSTA level of replica r2 versus frequency (re $6.25 \cdot 10^{-6}\,m^4\,N^{-2}\,s^{-2}$)

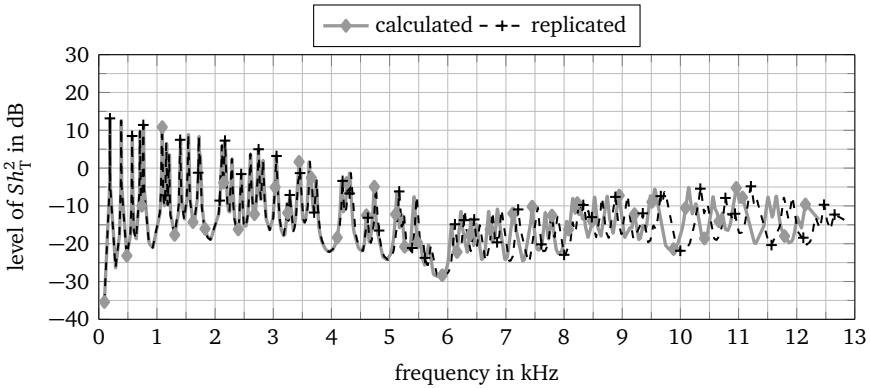

Figure 4.11: MSTA level of replica r3 versus frequency (re $6.25 \cdot 10^{-6}\,\mathrm{m^4\,N^{-2}\,s^{-2}}$)

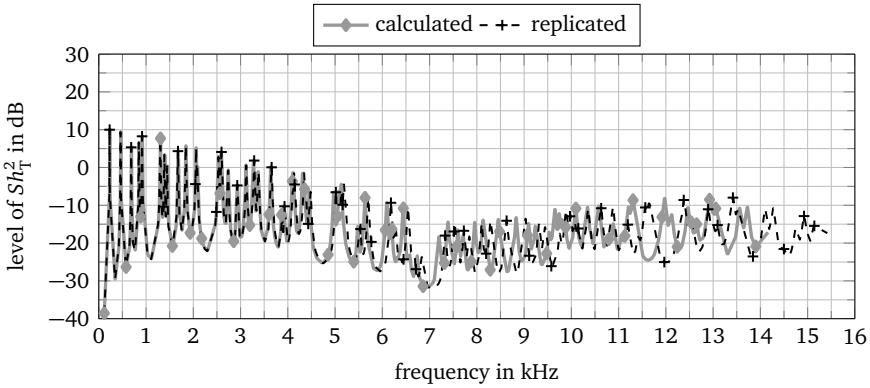

Figure 4.12: MSTA level of replica r4 versus frequency (re $6.25 \cdot 10^{-6}\,\mathrm{m^4\,N^{-2}\,s^{-2}}$)

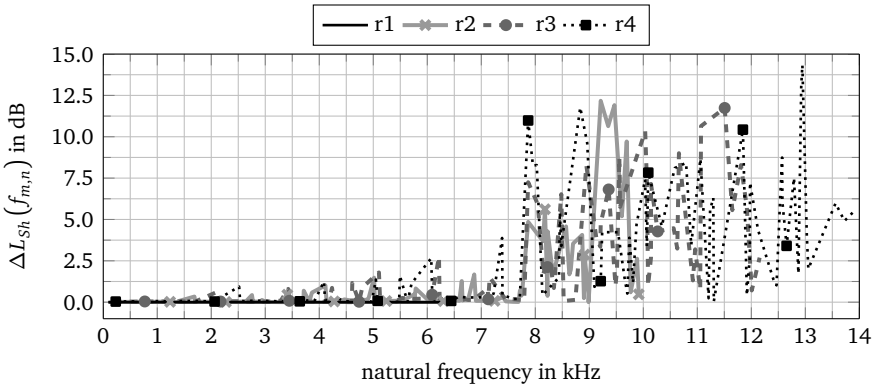

Figure 4.13: difference $\Delta L_{Sh}\left(f_{m,n}\right)$ of the replicated MSTA levels

4.2.4 Validation of scaling laws by experimental simulations

The scaling laws derived in Section 4.2.2 are validated by experimental simulations of simply supported rectangular plates. The natural frequencies and the MSTA levels of two replicas are replicated from measured natural frequencies and MSTA levels of a parent. The replicated vibration responses are compared with measured vibration responses of the replicas in order to validate the scaling laws. In addition, it is validated that the parent and the replicas are actually in similitude by analyzing the mode shape order and the damping.

This section is organized as follows: First, the experimental setup and the measurement procedures used to determine the vibration responses, the mode shapes, and the damping are described. Second, the similitude of the mode shapes and of the damping is analyzed. Third, the vibration responses of the replicas are replicated from those of the parent and compared with measured vibration responses of the replicas.

Experimental setup and measurement procedures

A corporate test stand, the so-called SAMple test stand,[2] is used to measure the vibration responses, see Figure 4.14. Circumferential brackets are screwed to the

[2] SAMple test stand – System reliability, Adaptive structures, and Machine acoustics test stand for primary laboratory experiments

acoustic box, where the simply supported rectangular plates (specimens) can be mounted. A scanning laser DOPPLER vibrometer (SLDV) measures the vibration velocities of the specimens. It is mounted at the surrounding truss structure [91]. The simply supported boundary conditions of the rectangular plates are

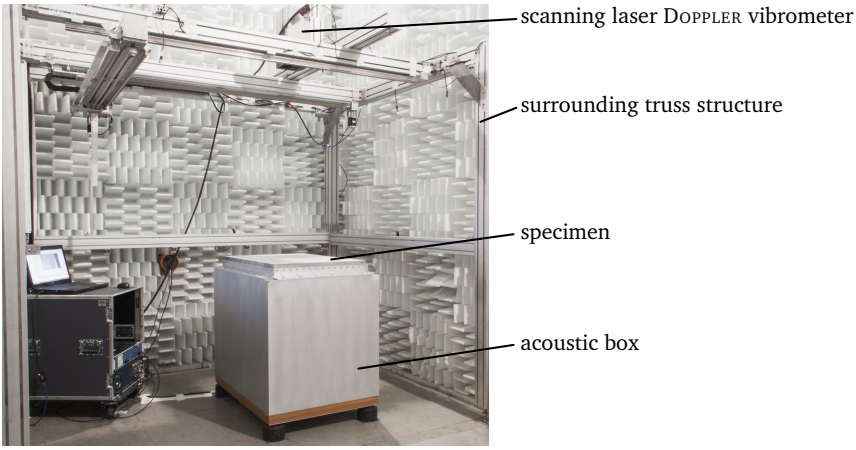

Figure 4.14: SAMple test stand for investigating simply supported rectangular plates, figure shows the parent rectangular plate

designed based on [92]. Steel blades of 0.5 mm thickness are bonded to the edges of the rectangular plates and are attached to the circumferential brackets. Their lengths l_{bl} are calculated from FE analyses, where the length l_{bl} is altered until the fundamental frequency matches the plate's fundamental frequency calculated from Eq. (2.6) within a permissible deviation of 5%. Higher natural frequencies are affected to a lesser extent by the boundary conditions. Thus, it is sufficient to consider the fundamental frequency only [92]. Further details on the design of the simply supported boundary conditions can be found in Appendix B.2 and in [92]. One parent and two different replicas are considered, see Table 4.5, where three specimens of each size are manufactured. The parent equals that of Section 4.2.1. Replica r1 is a half-scale model in length and width, while the thickness is kept ($\phi_l = 0.5$, $\phi_t = 1.0$), and replica r2 is a perfect half-scale model ($\phi_l = \phi_t = 0.5$). All specimens are made from aluminum. The YOUNG'S modulus and the POISSON'S ratio of all specimens are obtained from measurements of the speed of sound of the material in longitudinal and transverse direction. The mass density is obtained from hydrostatic weighing

[93]. Table C.3 on page 173 lists the material properties of each specimen including the measurement uncertainty and Table 4.1 on page 60 lists the averaged material properties.

Table 4.5: geometrical dimensions and scaling factors of the specimens

specimen		dimensions in mm a	b	t	scaling factors ϕ_a	ϕ_b	ϕ_t	ϕ_l	l_{bl} in mm
parent	p	870	620	5.0	1.0	1.0	1.0	1.0	25
replica	r1	435	310	5.0	0.5	0.5	1.0	0.5	15
replica	r2	435	310	2.5	0.5	0.5	0.5	0.5	50

The material loss factors of all specimens are obtained in order to assess the similitude of the damping, whereas the mode shapes, the modal damping, and the natural frequencies are obtained from experimental modal analyses of one specimen of each size only, and the MSTA levels are obtained from frequency response analyses of one specimen of each size as well. The detailed measurement and analysis procedures are subsequently described.

Similitude of the loss factor

The similitude of the damping is analyzed by an analysis of variance (ANOVA) [63] of the loss factors. The aim is to determine the effects of the specimen's size and of the simply supported boundary conditions on the similitude of the damping. The loss factors of the specimens are estimated from the 3 dB bandwidth

$$\eta_i = \frac{\Delta f_i}{f_i}, \tag{4.23}$$

where Δf_i is the 3 dB bandwidth of a peak in a measured transfer function at the frequency f_i [17]. The transfer function is measured between two representative points of each specimen. The specimens are excited at the dimensionless coordinate $(0.318a, 0.368b)$ by an impact hammer (Dytran 5850B) and the vibration response is measured at the dimensionless coordinate $(0.929a, 0.684b)$ by an accelerometer (Brüel & Kjær 45118-003). The dimensionless coordinates are irrational numerical proportions of length and width, and they are spread on the specimens' surface. This ensures that the transfer functions of the specimens are homologous and that they are representative for the specimens' vibration behavior. Thus, all loss factors of the specimens can be compared to each other

regarding their similitude. The loss factors of each specimen are determined at 30 peaks of the transfer function, where an automatic peak detection algorithm of MATLAB is used. Each transfer function is measured three times at three different states:

- specimens with *FFFF* boundary conditions,
- specimens with blades bonded to the edges and *FFFF* boundary conditions,
- specimens with *SSSS* boundary conditions.

The loss factors are compared during the ANOVA between the specimen's sizes to determine the effect of the specimen's size on the similitude of the damping. Comparing the loss factors between the three states during the ANOVA allows for determining the effect of the simply supported boundary conditions on the similitude of the damping. This leads to the following null hypotheses for the ANOVA

1. *the loss factor is independent from the specimen's size* and
2. *the loss factor is independent from the specimen's boundary conditions*,

which are tested on a confidence level of 95%. If the first null hypothesis can be rejected the loss factors of the specimens are considered in similitude. If the second null hypothesis can be rejected the loss factor is independent from the boundary conditions, i.e., the blades bonded to the edges do not affect the loss factors.

Experimental modal analysis and similitude of the modes

The experimental modal analysis is performed using the SLDV as shown in Figure 4.14. The specimens are excited by an impact, while the SLDV measures the time-decaying vibration velocity. The impact is generated by an electrodynamic shaker (LDS V101) that is equipped with an impedance head (PCB 288D01) to measure the impact force, see [91] and Appendix B.2 (pages 156 et seqq.). The first 10 natural frequencies, mode shapes, and modal damping values are determined from experimental modal analyses, where MATLAB R2017a is used. The modal analysis algorithm uses the least squares complex exponential method [94].

The measured natural frequencies are used to validate the scaling law in Eq. (4.16). The similitude of the mode shape order is analyzed using MAC, see Eq. (4.19), and the similitude of the modal damping is analyzed using ANOVA. In contrast to the loss factor measurements, the modal damping can be related to a certain mode shape, which allows for determining the similitude of the modal damping for each mode. Several ANOVA are performed, where the modal damping of more and more modes is taken into account, and the null hypothesis *the modal damping is independent from the specimen's size* is tested on a confidence level of 95% [91].

Frequency response analysis

The MSTA is obtained from a frequency response analysis, where the vibration velocities are measured using the SLDV. The MSTA is calculated from Eqs. (2.9) and (2.10), and the levels are calculated. A reaction-type shaker with a pre-mounted impedance head (WILCOXON RESEARCH F5B/Z11) causes the specimens to vibrate, where a sine sweep is used. The sine sweep's frequency ranges from half of the specimen's fundamental frequency to 5 kHz, which is found to be the maximum possible frequency of the reaction-type shaker. Further details on the measurement procedure are given in Appendix B.2 and [91].

Results and discussion

The results are presented in the following order

- similitude of the loss factors,
- similitude of the modal damping,
- similitude of the mode shape order,
- comparison of replicated and measured natural frequencies,
- comparison of replicated and measured MSTA levels.

Similitude of the loss factors

In sum, 2381 valid loss factors are obtained from the transfer function measurements, while 49 loss factors are obvious outliers, e.g., due to erroneous peak detection. The loss factors are found to be log-normally distributed, i.e., the logarithmized loss factors $\ln(\eta_i)$ are used for the ANOVA instead of the

loss factors η_i themselves. Figure 4.15 shows the box plot[3] obtained from the ANOVA to test the first null hypothesis (see page 78). The gray horizontal lines are the median, the box covers 50% of the loss factors, and the whiskers cover 99.3% of the loss factors. The gray crosses mark loss factors that are outside of the 99.3% bounds. They are considered outliers. The notches of the boxes are not overlapping, i.e., the loss factors of the specimens differ on the confidence level of 95%. Thus, the first null hypothesis must be rejected and the loss factors are not in similitude. It can be expected that the replicated vibration responses differ from those of the measurements due to the incomplete similitude of the loss factors.

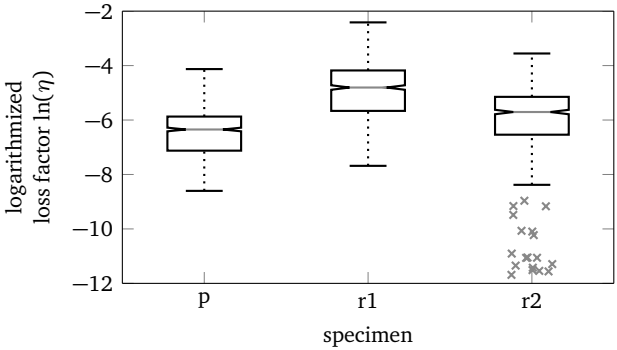

Figure 4.15: box plot of logarithmized loss factors for the parent and the replicas r1 and r2, see Figure C.6 on page 166 for an explanation of the box plot

Figure 4.16 shows the box plot obtained from the ANOVA to test the second null hypothesis (see page 78). The median loss factor of the specimens with *FFFF* boundary conditions equals $0.952 \cdot 10^{-3} (= \mathrm{e}^{-6.957})$. It increases to $4.072 \cdot 10^{-3} (= \mathrm{e}^{-5.504})$ after the blades have been bonded to the specimens, and it further increases to $5.704 \cdot 10^{-3} (= \mathrm{e}^{-5.167})$ for the specimens with *SSSS* boundary conditions. This is equivalent to an increase by factors of 4.28 and of 1.40, respectively. Due to fact that the notches of the boxes are not overlapping, the loss factor increases significantly on the confidence level of 95%. Thus, the second null hypothesis must be rejected as well and the loss factors depend on the boundary conditions of the specimens. The variance (i.e., the size of the

[3] Figure C.6 on page 166 explains the terms that are subsequently used to analyze the box plot.

box) of the loss factors of the specimens with "*SSSS* boundary conditions" is higher than that of the specimens with "*FFFF* boundary conditions" and "*FFFF* boundary conditions with blades bonded". Thus, attaching the specimens to the brackets rather causes the variance of the loss factors to increase, while bonding the blades to the specimens mainly causes the loss factor itself to increase.

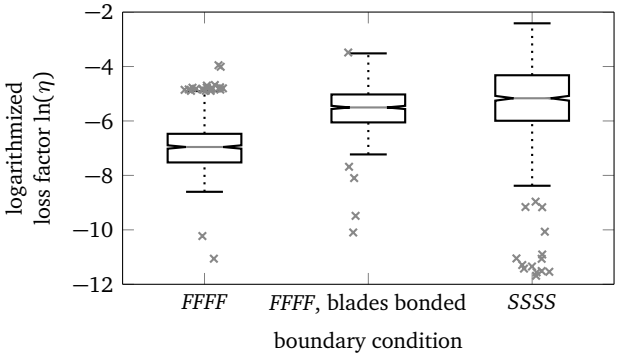

Figure 4.16: box plot of logarithmized loss factors for the specimens with different boundary conditions, see Figure C.6 on page 166 for an explanation of the box plot

Similitude of the modal damping

The ANOVA of the modal damping is repeated, where more and more modes are taken into account. The results of the ANOVA are illustrated in Figure 4.17, where the value $1-p$ is plotted versus the cumulative mode number. p denotes the probability that an F-statistic takes a higher value than the calculated statistic value of the loss factors for the different *specimen's sizes* (p, r1, r2) [63]. The *cumulative* mode number in Figure 4.17 indicates the total number of modes that are used during the ANOVA, e.g., a cumulative mode number of 5 uses the modal damping of the modes 1 through 5 of each specimen. The value $1-p$ exceeds the confidence level of 95% if more than 7 modes are taken into account, which leads to a significant difference of the modal damping if more than 7 modes are considered. Thus, the modal damping of the specimens is in similitude unless more than the first 7 modes are taken into account [91]. This corresponds to 0.6 kHz and 1.2 kHz for the replicas r1 and r2, respectively. As a consequence, it can be expected that the vibration responses can be accurately

replicated up to 0.6 kHz and 1.2 kHz, while deviations between the measured vibration responses and the replicated vibration responses are expected above these frequencies.

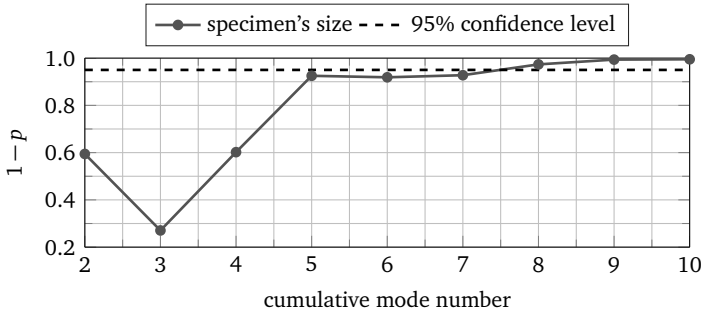

Figure 4.17: $1-p$ value of the ANOVA of the modal damping versus the cumulative mode number

Similitude of the mode shape order

Figure 4.18 illustrates the MAC values for the measured mode shapes of the replicas r1 and r2 with respect to the measured mode shapes of the parent. The MAC values on the main diagonal are close to one, while all off-diagonal values are close to zero, i.e., the mode shapes of both replicas are in similitude to the parent. However, the mode shapes 7 and 8 of the replicas r1 and r2 as well as mode shape 4 of replica r2 are poorly excited due to increased damping. The modal analysis algorithm fails to fit a physically meaningful mode shape, although a value for the natural frequency is obtained [91]. As a consequence, these mode shapes are excluded from further analysis.

Replicating the natural frequencies

The scaling law in Eq. (4.16) replicates the natural frequencies of the replicas r1 and r2 from those of the parent. Figure 4.19 illustrates the replicated natural frequencies versus those from the experimental modal analysis of the replicas. Only the modes with MAC values close to one are considered (see Figure 4.18). They are labeled by their mode number in Figure 4.19. The natural frequencies are located on the main diagonal of the plot. Thus, the replicated natural frequencies agree well with the measured ones. Calculating the error ε_f in analogy to Eq. (4.20) yields mean errors of 2.6% and 3.5% for the replicas r1

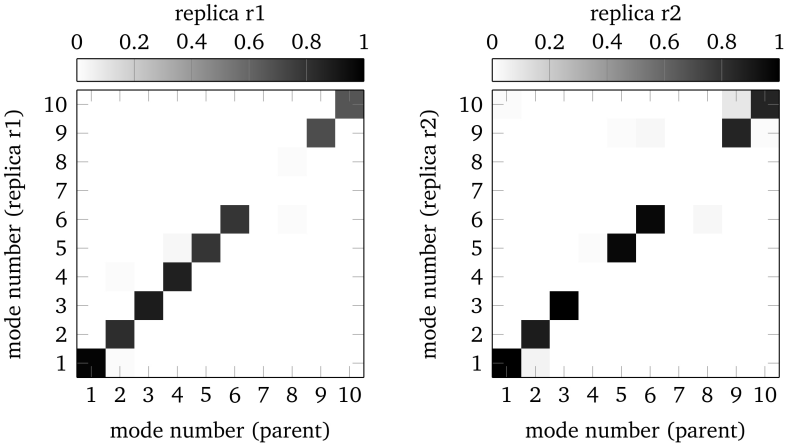

Figure 4.18: MAC matrices of the replicas r1 and r2, MAC values are indicated by the grayscale

and r2, respectively, and the maximum error is approximately 11% for both replicas [91]. The mean error ε_f is lower than the permissible deviation of 5%, which is considered during the design of the simply supported boundary conditions, see page 76. Although the loss factors and the modal damping are

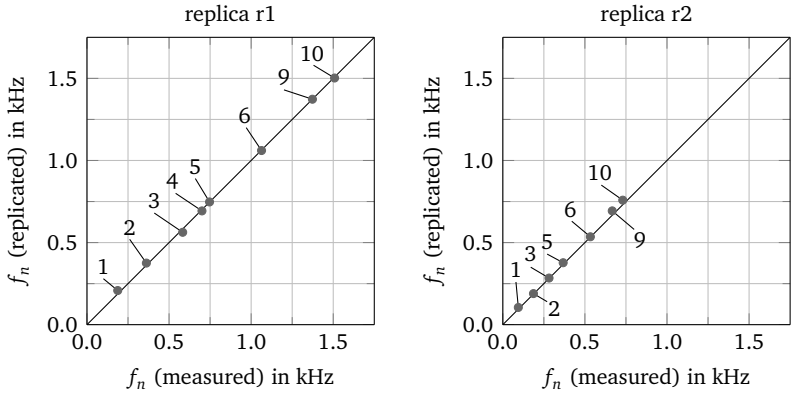

Figure 4.19: replicated natural frequencies versus measured natural frequencies of the replicas r1 and r2, numbers denote the mode numbers

not in similitude, the natural frequencies can still be replicated sufficiently well since the specimens are still weakly damped, i.e., the natural frequencies are hardly affected by the damping. Thus, the scaling law of the natural frequencies can be validated for scaling measured natural frequencies of simply supported rectangular plates.

Replicating the MSTA

The scaling law in Eq. (4.16) replicates the frequencies of MSTA and Eq. (4.17) replicates the MSTA magnitudes of the replicas r1 and r2 from those of the parent. The replicated MSTA levels of replica r1 agree sufficiently well with the measured MSTA levels up to approximately 1 kHz, see top of Figure 4.20. Note that the frequency axis applies to both plots in the same manner. Above 1 kHz the frequencies are still accurately replicated, but the replicated MSTA levels are higher than the measured MSTA levels. The frequency of 1 kHz is slightly

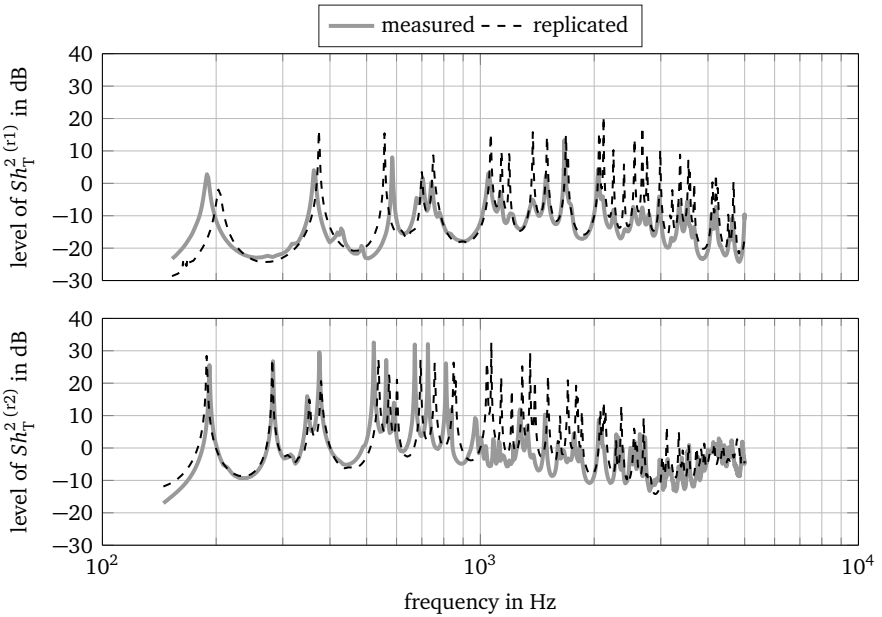

Figure 4.20: replicated and measured MSTA levels versus frequency (re $6.25 \cdot 10^{-6}\,\mathrm{m^4\,N^{-2}\,s^{-2}}$), top: replica r1, bottom: replica r2, frequency axis applies to both plots

higher than the natural frequency of the 8th mode, where the modal damping is not in similitude anymore. Thus, the replicated MSTA levels differ from the measured MSTA levels due to incomplete similitude of the modal damping. The replicated MSTA levels of replica r2 also agrees well with the measured MSTA levels up to approximately 1 kHz, see Figure 4.20, bottom. However, this is slightly lower than the natural frequency of the 8th mode, where the modal damping is not in similitude anymore. Above 1 kHz, the frequencies are again accurately replicated and the replicated MSTA levels are again higher than the measured ones. In order to improve the accuracy of the scaling laws for replicating the MSTA magnitudes at frequencies above 1 kHz, the damping must be considered in the scaling laws. However, this leads to incomplete similitude conditions, which is out of the scope of this section.

4.3 Scaling laws of a generic car undercarriage

This section applies the proposed scaling method to a generic car undercarriage (GCU) made from fiber-reinforced plastics. Fiber-reinforced plastics more and more substitute metals such as steel and aluminum since lightweight designs are getting more and more important in the automotive industry, e.g., to reduce fuel consumption. Scaling laws are not only derived for a global vibration response, i.e., the natural frequencies, but also for local vibration responses, i.e., the driving point admittance and the vibration velocities at an arbitrarily chosen receiver point. The scaling laws incorporate the geometrical dimensions and the material properties, but complete similitude conditions are always kept. A complete similitude of material properties might be hardly achievable in practice. Nevertheless, it is validated whether material properties can be scaled by the proposed scaling method in principle.

The FE model setup and the parent GCU are described in Section 4.3.1. Scaling laws are derived by the proposed scaling method (Section 4.3.2) and validated by replicating the vibration responses of replicas from those of a parent in virtual simulations (Section 4.3.3). Complete geometrical similitude conditions of the GCU are validated by analyzing the maximum deviations between replicated and calculated vibration responses (Section 4.3.4).

4.3.1 Virtual model of the parent generic car undercarriage

The parent GCU is shown in Figure 4.21 and its geometrical design parameters are listed in Table 4.6. The GCU consists of two thin rectangular plates that are connected by a trapezoidal transmission tunnel, where the thickness ratio $\xi = 337.5 > 50$, see Section 4.2.3. This simple design of the GCU neglects other requirements such as structural durability, producibility, or crash reliability, but the GCU is more complex than a thin rectangular plate due to the transmission tunnel. An additional mass m_A that equals 10% of the GCU's total mass is placed on the GCU to avoid double natural frequencies due to geometrical symmetry [85, 95]. A dynamic force acting at the spatial location $(a_\mathrm{F},\, b_\mathrm{F})$ causes the GCU to vibrate. The vibration responses are the natural frequencies f_n, where n denotes the mode number, the driving point admittance

$$h_\mathrm{F}^2 = \frac{\tilde{v}_\mathrm{F}^2}{\tilde{F}^2}, \tag{4.24}$$

where $\tilde{v}_\mathrm{F}^2$ denotes the squared RMS vibration velocity at the excitation position $(a_\mathrm{F}, b_\mathrm{F})$, and the squared RMS vibration velocity at the receiver point $\tilde{v}^2\,(a_\mathrm{R},\ b_\mathrm{R}) = \tilde{v}_\mathrm{R}$.

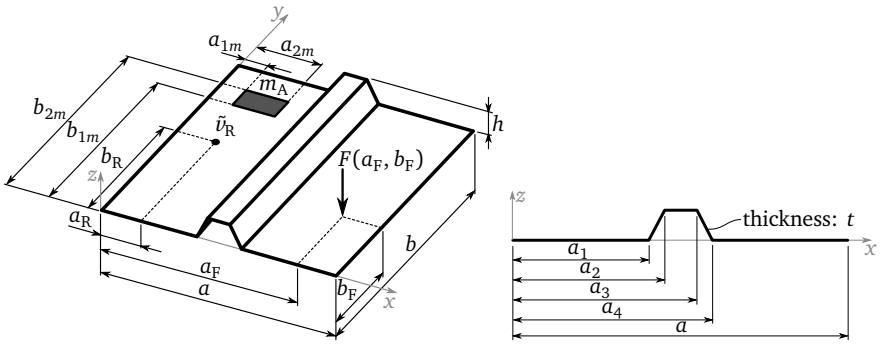

(a) 3-D view **(b)** profile view

Figure 4.21: geometry of the parent GCU, superscript (p) is dropped for convenience

An FE model of the GCU with free boundary conditions (*FFFF*) is set up, where SHELL281 elements [87] of 25 mm size are used [85]. The orthotropic material properties of the fiber-reinforced plastic are modeled by setting the YOUNG'S moduli E_x, E_y, and $E_z = E_y$ in global x-, y-, and z-direction, respectively, as well as the shear modulus G_{xy}. Considering an epoxy matrix and carbon fibers with a fiber volume ratio of 0.6 yields the material properties listed in Table 4.7. The material properties are calculated from the rule of mixture and material properties from literature [96, 97]. The material model is kept simple since the proposed scaling method needs to be validated for complete similitude conditions in a first step. Vibrations of fiber-reinforced plastics are significantly affected by the material properties including number of plies, fiber angle, and stacking sequence. However, scaling these material properties leads to incomplete similitude conditions [35–37], which is out of the scope of this section. The vibration responses are calculated up to the 20th natural frequency. The driving point admittance $h_{\mathrm{F}}^{2\ (\mathrm{p})}$ and the receiver point velocity $\tilde{v}_{\mathrm{R}}^{(\mathrm{p})}$ of the parent GCU are plotted versus frequency in Figure 4.22. The frequency axis applies to both plots in the same manner and the markers indicate the natural frequencies.

Table 4.6: geometrical design parameters of the parent GCU (values in mm), superscript (p) is dropped for convenience

symbol	value	symbol	value	symbol	value	symbol	value
a	1 350	a_1	546	a_{1m}	170	b_{F}	500
b	1 470	a_2	610	a_{2m}	440	b_{R}	830
h	130	a_3	740	a_{R}	235	b_{1m}	1 080
t	4	a_4	804	a_{F}	1 175	b_{2m}	1 250

Table 4.7: material properties of the parent GCU, superscript (p) is dropped for convenience

parameter	symbol	value	unit
YOUNG's modulus	E_x	$1.39 \cdot 10^{11}$	$\mathrm{N\,m^{-2}}$
YOUNG's modulus	E_y	$1.06 \cdot 10^{10}$	$\mathrm{N\,m^{-2}}$
shear modulus	G_{xy}	$5.14 \cdot 10^{9}$	$\mathrm{N\,m^{-2}}$
POISSON's ratio	μ	0.28	–
mass density	ρ	1 524	$\mathrm{kg\,m^{-3}}$
loss factor	η	0.005	–

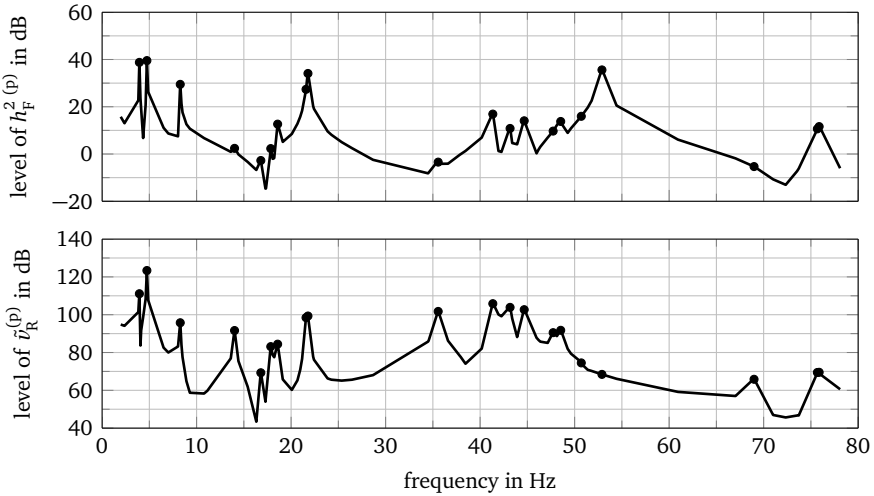

Figure 4.22: vibration responses of the parent GCU versus frequency, top: level of the driving point admittance (re $6.25 \cdot 10^{-6}\,\mathrm{m^2\,N^{-2}\,s^{-2}}$), bottom: level of the vibration velocity at the receiver point (re $5 \cdot 10^{-8}\,\mathrm{m\,s^{-1}}$), markers are placed at the natural frequencies

4.3.2 Derivation of scaling laws of the generic car undercarriage

All lengths, the thickness, and the mass density of the GCU are scaled by the factors ϕ_l, ϕ_t, and ϕ_ρ, respectively. The POISSON's ratio is considered constant, i.e., $\phi_\mu \approx 1$. The YOUNG's moduli and the shear modulus are scaled by a common factor ϕ_E to ensure complete similitude conditions. The scaling laws are established according to Eq. (4.3). Altering each design parameter by ±2% during an LSA of the parent GCU and taking the mean value of the powers yields

$$\frac{f_n^{(\mathrm{r})}}{f_n^{(\mathrm{p})}} = \phi_{f_n} = \phi_l^{-2}\phi_t^{1}\phi_E^{0.5}\phi_\rho^{-0.5} \tag{4.25}$$

for the natural frequencies,

$$\frac{h_{\mathrm{F}}^{2\,(\mathrm{r})}}{h_{\mathrm{F}}^{2\,(\mathrm{p})}} = \phi_{h_{\mathrm{F}}} = \phi_l^{0}\phi_t^{-4}\phi_E^{-1}\phi_\rho^{-1} \tag{4.26}$$

for the driving point admittance, and

$$\frac{\tilde{v}_{\mathrm{R}}^{(\mathrm{r})}}{\tilde{v}_{\mathrm{R}}^{(\mathrm{p})}} = \phi_{\tilde{v}_{\mathrm{R}}} = \phi_l^{0.1}\phi_t^{-4.1}\phi_E^{-1}\phi_\rho^{-1} \tag{4.27}$$

for the receiver point velocity. The powers of the geometrical scaling factors ϕ_l and ϕ_t in Eq. (4.25) equal those of the scaling law for the natural frequencies of the rectangular plate, cf. Eq. (4.25) and Eq. (4.16). The natural frequencies of the GCU and of a flat rectangular plate scale in the same manner, since the GCU is still a thin plate-like structure. The driving point admittance depends only on the thickness and on the material properties. The scaling factor of the lengths $\phi_l^0 = 1$ is removed from the scaling law (see the 2nd remark on page 58). The scaling law for the receiver point velocity $\tilde{v}_{\mathrm{R}}$ almost equals that of the driving point admittance, but the scaling factor of the lengths weakly affects the vibration velocity $\tilde{v}_{\mathrm{R}}$. In case of perfect geometrical similitude ($\phi_l = \phi_t$) the driving point admittance and the receiver point velocity scale in the same manner.

4.3.3 Validation of the scaling of material properties by virtual simulations

Four replicas are defined according to Table 4.8. The replicas r1 and r2 are perfect half-scale models, whereas r3 and r4 are half-scaled in their lengths, while the thickness is scaled by a factor of 0.25. The replicas r1 and r3 are made from the same material as the parent, but the fiber volume ratio is reduced to 0.4, i.e., it is scaled by a factor of 2/3. For the replicas r2 and r4 the carbon fiber is replaced by glass fiber, while the fiber volume ratio is kept. The material

Table 4.8: scaling factors and thickness ratios of the replica GCU

replica	ϕ_l	ϕ_t	ϕ_E	ϕ_ρ	ξ
r1	0.50	0.50	0.70	0.90	337.5
r2	0.50	0.50	0.35	1.30	337.5
r3	0.50	0.25	0.70	0.90	675.0
r4	0.50	0.25	0.35	1.30	675.0

properties are again calculated from the rule of mixture and material data from literature [96, 97]. Table C.1 on page 167 lists all geometrical design parameters and material properties of the replicas. The vibration responses of the

replicas are calculated from an FE model and replicated from Eqs. (4.25), (4.26), and (4.27). A MAC analysis shows that the mode shape order is kept. Thus, the mode shape order of the parent and of the replicas r1 through r4 are in similitude. The MAC matrices are plotted in Figure C.7 on page 168 for the sake of completeness. Figure 4.23 illustrates the replicated natural frequencies versus those from the FE calculation. The maximum error of the natural frequencies reads

$$\varepsilon_{f,\max} = \max\left(\varepsilon_f\right) = \max\left(\left|\frac{f_{\mathrm{FE}} - f_{\mathrm{SL}}}{f_{\mathrm{FE}}}\right| \cdot 100\%\right). \tag{4.28}$$

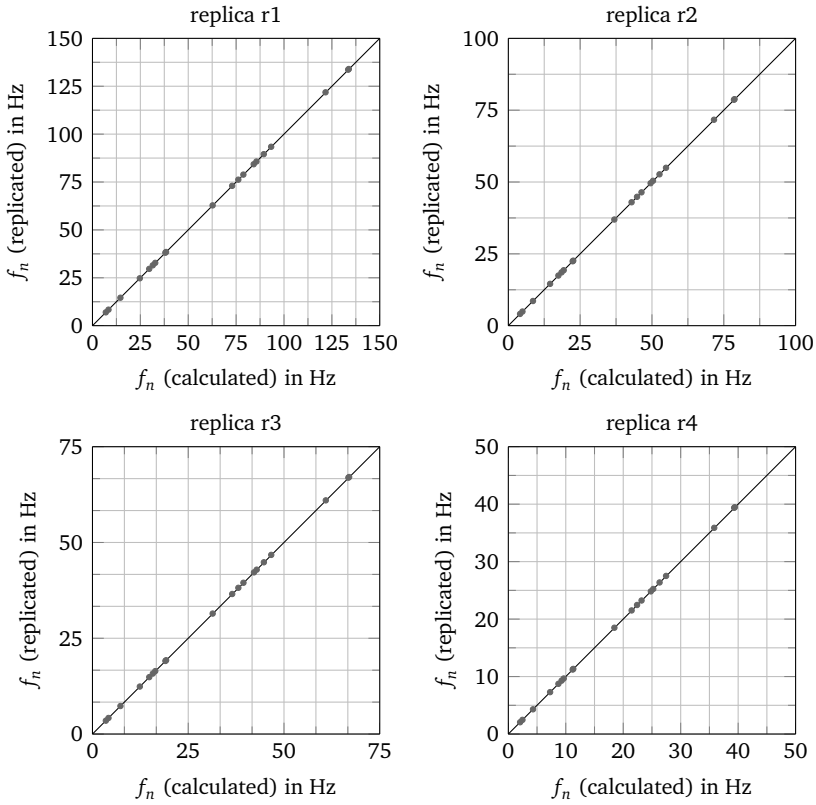

Figure 4.23: replicated natural frequencies versus calculated natural frequencies of the GCU

The maximum error yields 0.12% for the replicas r1 and r2, and 0.25% for the replicas r3 and r4. Thus, the natural frequencies are accurately replicated from Eq. (4.25). However, the maximum error of the natural frequencies of the replicas r3 and r4 is approximately twice the maximum error of the replicas r1 and r2. On the one hand, the replicas r3 and r4 are scaled down in thickness, i.e., they are thinner compared to the parent since the thickness ratio ξ increases, see Table 4.8. Thus, shear deformations should hardly affect the replicated natural frequencies. On the other hand, complete geometrical similitude in case of different scaling factors $\phi_l \neq \phi_t$ is validated only for flat plates [31]. Thus, the increased error of the replicated natural frequencies of the replicas r3 and r4 is rather caused by geometrically incomplete similitude conditions due to different scaling factors $\phi_l \neq \phi_t$ than due to shear deformations. Further assessment of geometrical similitude conditions of the GCU follows in Section 4.3.4.

The levels of the replicated driving point admittance and of the receiver point velocity of the replicas r1 through r4 are plotted in Figures 4.24 through 4.27, respectively. The replicated vibration responses agree well with those from the calculations. The maximum level differences are calculated from

$$\Delta L_{h_{\mathrm{F,max}}} = \max\left(\left|L_{h_{\mathrm{F,FE}}}(f_n) - L_{h_{\mathrm{F,SL}}}(f_n)\right|\right) \tag{4.29}$$

and

$$\Delta L_{v_{\mathrm{R,max}}} = \max\left(\left|L_{v_{\mathrm{R,FE}}}(f_n) - L_{v_{\mathrm{R,SL}}}(f_n)\right|\right). \tag{4.30}$$

The maximum level differences are within approximately 1 dB as can be seen from Table 4.9. Thus, the driving point admittance and the receiver point velocity are accurately replicated. Again, the maximum level differences of the replicas r3 and r4 are higher than those of the replicas r1 and r2 due to incomplete geometrical similitude conditions.

Table 4.9: maximum level difference of the replicated driving point admittance and of the receiver point velocity in dB

replica	$\Delta L_{h_{\mathrm{F,max}}}$	$\Delta L_{v_{\mathrm{R,max}}}$
r1	0.05	0.06
r2	0.05	0.06
r3	0.43	1.08
r4	0.43	1.08

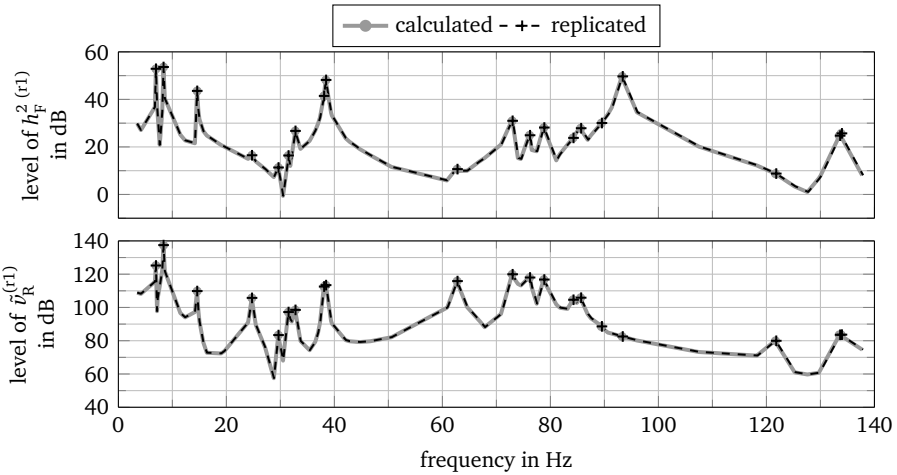

Figure 4.24: vibration responses of replica r1 versus frequency, top: level of the driving point admittance (re $6.25 \cdot 10^{-6}\,\mathrm{m^2\,N^{-2}\,s^{-2}}$), bottom: level of the receiver point velocity (re $5 \cdot 10^{-8}\,\mathrm{m\,s^{-1}}$)

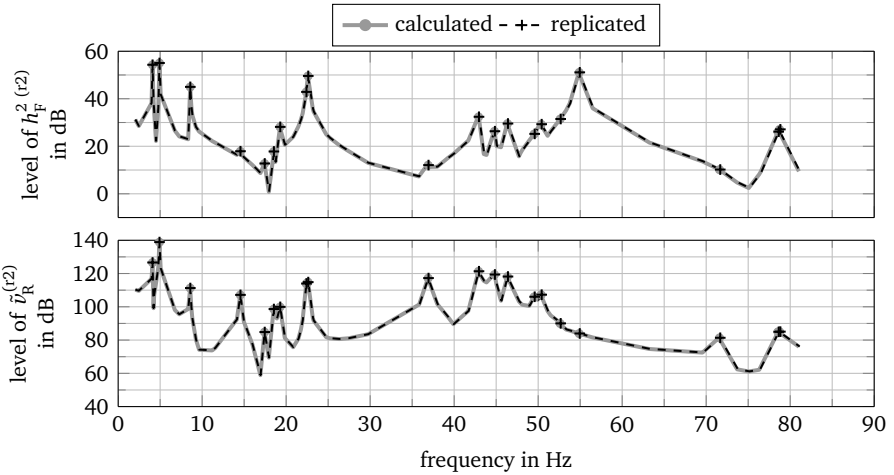

Figure 4.25: vibration responses of replica r2 versus frequency, top: level of the driving point admittance (re $6.25 \cdot 10^{-6}\,\mathrm{m^2\,N^{-2}\,s^{-2}}$), bottom: level of the receiver point velocity (re $5 \cdot 10^{-8}\,\mathrm{m\,s^{-1}}$)

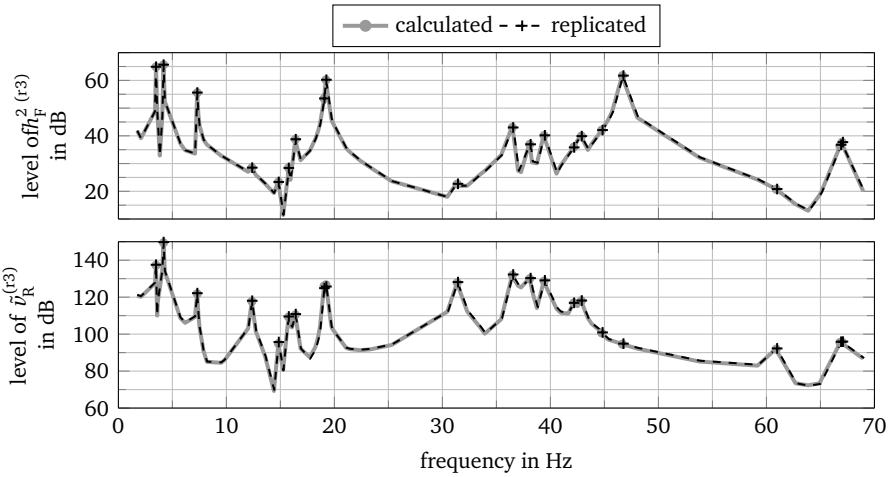

Figure 4.26: vibration responses of replica r3 versus frequency, top: level of the driving point admittance (re $6.25 \cdot 10^{-6}\,\mathrm{m^2\,N^{-2}\,s^{-2}}$), bottom: level of the receiver point velocity (re $5 \cdot 10^{-8}\,\mathrm{m\,s^{-1}}$)

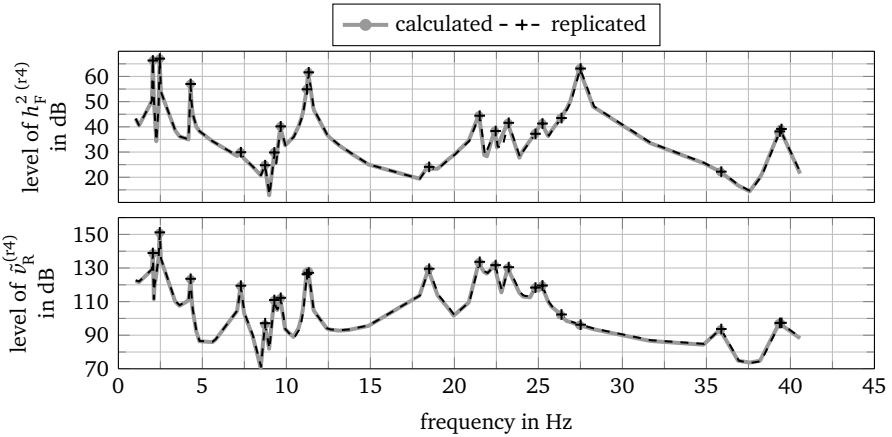

Figure 4.27: vibration responses of replica r4 versus frequency, top: level of the driving point admittance (re $6.25 \cdot 10^{-6}\,\mathrm{m^2\,N^{-2}\,s^{-2}}$), bottom: level of the receiver point velocity (re $5 \cdot 10^{-8}\,\mathrm{m\,s^{-1}}$)

4.3.4 Validation of complete geometrical similitude conditions by virtual simulations

Thin flat plates remain in complete geometrical similitude if the scaling factors of the lengths and of the thickness differ [31]. On the one hand, perfect geometrical similitude conditions of the GCU requires that *all* geometrical dimensions are scaled by the same factor. On the other hand, scaling laws are derived for the GCU in Section 4.3.2, where the scaling factors of all lengths ϕ_l and of the thickness ϕ_t differ. It is validated in Section 4.3.3 that these scaling laws accurately replicate the vibration responses, although the scaling factors ϕ_l and ϕ_t differ. In order to validate complete geometrical similitude conditions of the GCU, two sets of replicas are defined. In the first set, only the thickness is scaled by factors $\phi_t = \{1.5,\ 2.0, \ldots,\ 7.0\}$. In the second set, only the lengths are scaled by factors $\phi_l = \{0.9,\ 0.8, \ldots,\ 0.1\}$. These values are chosen since the thickness ratio ξ drops below the minimum value of 50 proposed in Section 4.2.3 at $\phi_t > 6.8$ and $\phi_l < 0.15$. The replicated vibration responses are compared with the calculated vibration responses using the maximum error of the natural frequencies given by Eq. (4.28), and the maximum level differences given by Eqs. (4.29) and (4.30). The similitude of the mode shape order is assessed using MAC, see Eq. (4.19).

Figure 4.28 illustrates the maximum error of the natural frequencies in case of scaling the thickness by ϕ_t (left part) and all lengths by ϕ_l (right part). The maximum error of the natural frequencies increases for an increasing scaling

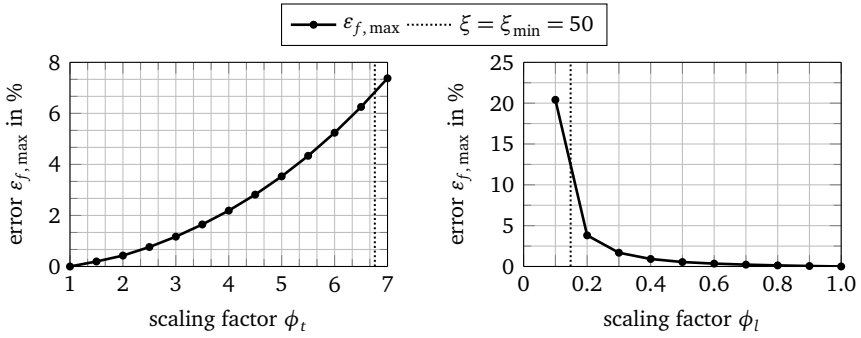

Figure 4.28: maximum error of the natural frequencies versus ϕ_t (left) and ϕ_l (right)

factor ϕ_t and a decreasing scaling factor ϕ_l due to the fact that the geometry is more and more distorted. However, the maximum error of the natural frequencies remains smaller than 7% and 12%, unless the thickness ratio ξ drops below its minimum value of 50. These maximum errors are similar to those of the replicated natural frequencies of the rectangular plates (see page 70). Thus, complete geometrical similitude conditions of the GCU can be assumed for the scaling law of the natural frequencies provided that the minimum thickness ratio of $\xi_{\min} = 50$ is exceeded.

The maximum level differences $\Delta L_{h_{\mathrm{F}},\max}$ and $\Delta L_{v_{\mathrm{R}},\max}$ are shown in Figure 4.29. The maximum level difference of the driving point admittance $\Delta L_{h_{\mathrm{F}},\max}$ continuously increases and decreases for increasing scaling factors ϕ_t and ϕ_l, respectively. It behaves similarly to the maximum error of the natural frequencies and the conclusions can be drawn in analogy.

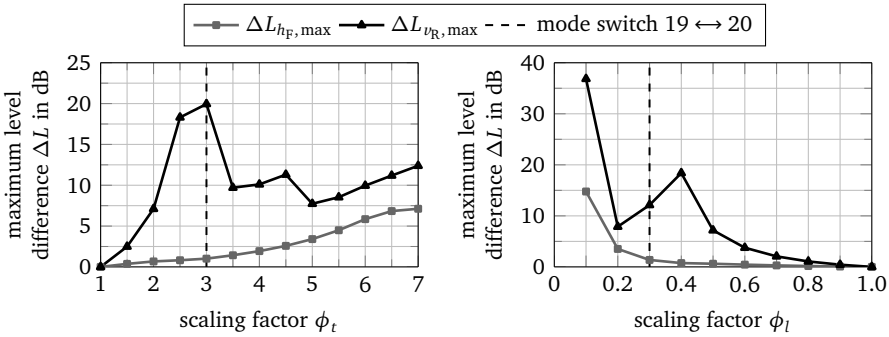

Figure 4.29: maximum level difference of the driving point admittance and of the receiver point velocity versus ϕ_t (left) and ϕ_l (right)

The maximum level difference of the receiver point velocity $\Delta L_{v_{\mathrm{R}},\max}$ increases to 20 dB at $\phi_t = 3.0$, drops to 10 dB at $\phi_t = 3.5$, and remains within 7–12 dB at $\phi_t > 3.5$. Similarly, decreasing the scaling factor ϕ_l causes the maximum level difference $\Delta L_{v_{\mathrm{R}},\max}$ to increase to 18 dB at $\phi_l = 0.4$ and to drop to 8 dB at $\phi_l = 0.2$. The behavior of the maximum level difference $\Delta L_{v_{\mathrm{R}},\max}$ can be explained by tracking the mode shape order of the replicas using MAC analysis. The mode shape order is tracked using a so-called *MAC track plot*, which is shown in Figure 4.30. Four MAC values at the indices (19,19), (20,20), (19,20), and (20,19) of the MAC matrix are plotted versus the scaling factors ϕ_t and

ϕ_l. The first index refers to the parent mode number and the second index refers to the replica mode number. MAC values close to one at the indices (19,19) and (20,20) indicate that the mode shape order of the parent and of the replica are equal, while MAC values close to one at the indices (19,20) and (20,19) indicate switched modes. The mode switch itself is highlighted by a thick gray dotted line. The MAC values at the indices (19,19) and (20,20) decrease for increasing and decreasing scaling factors ϕ_t and ϕ_l, respectively. The modes actually switch at the scaling factors $\phi_t = 3.0$ and $\phi_l = 0.3$. At scaling factors $\phi_t > 3.0$ and $\phi_l < 0.3$ the MAC values at the indices (19,20) and (20,19) increase to approximately 1.0, but the interchanged mode shape order is kept. Coming back to the maximum level difference $\Delta L_{v_{\mathrm{R}},\max}$ shown in Figure 4.29, its increase at the scaling factors $\phi_t = 3.0$ and $\phi_l = 0.4$ is associated to decreased MAC values at indices (19,19) and (20,20), which are caused by small changes of the mode shapes. After the modes are interchanged, the maximum level difference $\Delta L_{v_{\mathrm{R}},\max}$ decreases again since the MAC values at indices (19,20) and (20,19), i.e., of the interchanged mode shapes, increase. Only the modes 19 and 20 switch unless $\phi_l < 0.15$. For $\phi_l = 0.1$ the maximum level difference $\Delta L_{v_{\mathrm{R}},\max}$ increases to approximately 38 dB since $\xi < \xi_{\min}$, i.e., the GCU cannot be considered thin anymore and increased deviations of the replicated and of the calculated vibration responses can be expected anyway.

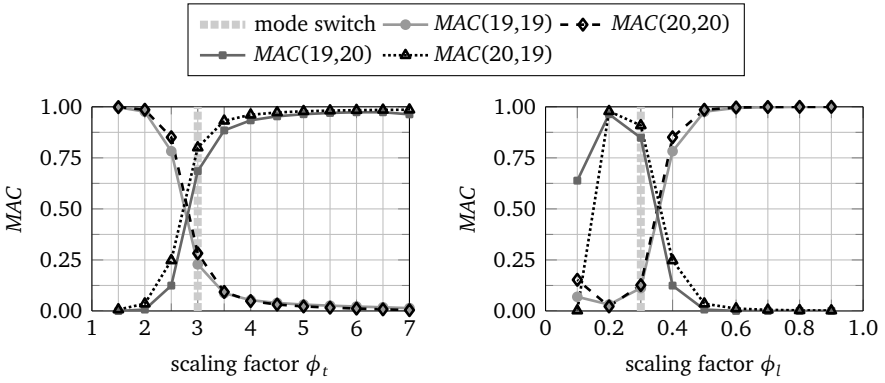

Figure 4.30: MAC track plot of the replica GCU versus ϕ_t (left) and ϕ_l (right)

However, the maximum level difference $\Delta L_{v_{\mathrm{R}},\max}$ occurs at frequency f_9, which corresponds to mode number 9 as exemplified in Figure 4.31 for a replica with $\phi_t = 3.0$. The MAC value of mode number 9 equals 1.0, thus, the replica mode shape is in similitude to that of the parent. Due to the fact that the modes are coupled in the frequency response analysis of the FE model, each operation deflection shape is affected by each mode. Thus, the maximum level difference does not necessarily occur at the modes with reduced MAC values or at switched modes.

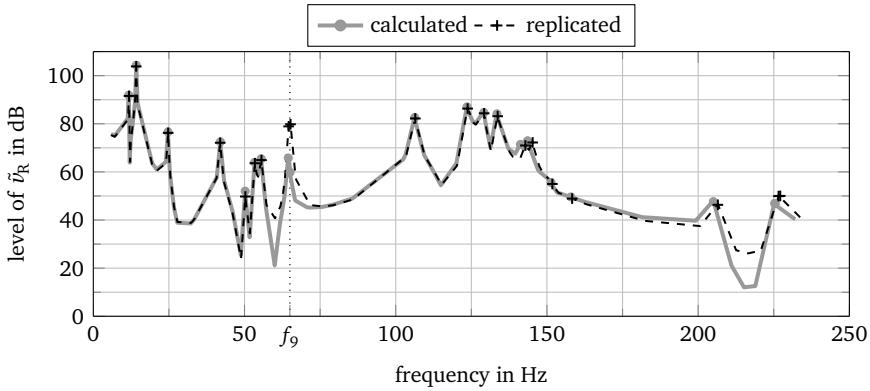

Figure 4.31: level of the vibration velocity at the receiver point (re $5 \cdot 10^{-8}\,\mathrm{m\,s^{-1}}$) of a replica scaled with $\phi_t = 3.0$, f_9 denotes the frequency of mode number 9

In summary, the minimum thickness ratio $\xi_{\min} = 50$ proposed for rectangular plates in Section 4.2.3 applies to the GCU as well. It indicates sufficiently well whether complete geometrical similitude conditions can be assumed if the natural frequencies or the driving point admittance are replicated. In case of replicating the receiver point velocity, the mode shape order of the parent and of the replica must strictly hold, i.e., neither the mode shape order nor the MAC value are allowed to change. A reduced MAC value indicates errors of the replicated receiver point velocity and mode switching introduces a certain amount of error as well. Due to mode coupling, the modes with decreased MAC values or switched modes are not necessarily those modes where the replicated receiver point velocity differs from the calculated one.

4.4 Summary of similitudes and sensitivities for complete similitude conditions

In this chapter, scaling laws are directly derived from virtual models such as FE models by combining similitude analysis with SA. A scaling law is considered a power law, which is motivated by similitude theory, and its powers can directly be calculated from an SA of a virtual model. Thus, scaling laws can straightforwardly be derived and a possible ambiguity of the scaling laws, e.g., as in DA, is avoided. Furthermore, the developed scaling method circumvents the choice of an appropriate fitting function, which is required for meta-models based on an SA such as linear regression models.

The scaling laws of vibrating rectangular plates in complete similitude are derived from an analytical model and from an FE model using LSA and GSA. The scaling laws agree well with those from literature, e.g., [22], and are verified regarding shear deformations, which are taken into account by the FE model, various boundary conditions, and changes of the FE mesh during the SA. Besides the geometrical dimensions, material properties can be considered in the scaling laws as well, which is exemplified for a vibrating GCU made from fiber-reinforced plastics.

Providing perfect similitude conditions, global and local vibration responses can accurately be replicated by the developed scaling method. If the length dimensions of FE models of the rectangular plates and of the GCU are scaled by a different factor than the thickness, the vibration responses can still be replicated sufficiently well unless the thickness ratio ξ is smaller than 50. Thus, complete similitude conditions can be considered for rectangular plates and plate-like structures that exceed the minimum thickness ratio of 50, although their length dimensions are scaled by a different factor than their thickness. However, local vibration responses such as the receiver point velocity tend to be more sensitive to deviations from perfect similitude conditions than global vibration responses such as the natural frequencies. Particularly, mode switching causes the replicated receiver point velocity to deviate from that of the calculation. Thus, the MAC track plot is introduced in order to track the mode shape order in a-posteriori analyses. The replicated receiver point velocity does not necessarily differ from the calculated one at the switched modes themselves due to mode coupling.

The scaling laws derived from virtual simulations are further validated by replicating measured natural frequencies and MSTA of simply supported rectangular plates. Provided that the parent and the replica are in complete similitude, the measured vibration responses can be replicated sufficiently well. Complete similitude of the simply supported rectangular plates is assessed by MAC analyses of the measured mode shapes and by ANOVA of the loss factors and of the modal damping. The implementation of the simply supported boundary conditions and the replicas' sizes mainly determine the damping and, thus, complete similitude conditions. However, replicating the MSTA with a sufficient accuracy requires the replicas to be in perfect similitude.

5 Similitudes and sensitivities for incomplete similitude conditions

This chapter enhances the scaling method proposed in Chapter 4 to geometrically incomplete similitude and validates the enhanced scaling method for vibrating rectangular plates (Section 5.1), which corresponds to the third step of the method development in this thesis, see Figure 1.2 on page 18. Finally, the enhanced scaling method is applied to a size range of gear boxes, where vibration responses from virtual and experimental simulations are considered (Section 5.2). This corresponds to the fourth step of the method development according to Figure 1.2.

5.1 Scaling laws for geometrically incomplete similitude of rectangular plates

The proposed scaling method is enhanced to geometrically incomplete similitude (Section 5.1.1). Scaling laws for a vibrating cantilever plate are derived in virtual simulations (Section 5.1.2). The scaling laws are validated by comparing replicated vibration responses with those obtained from FE calculations and the scaling method SAMSARA [57] (Section 5.1.3). SAMSARA is a state-of-the-art scaling method that benchmarks the proposed scaling method. It can be expected that the proposed scaling method and SAMSARA rather approximate the vibration responses than exactly replicate them. In order to assess the accuracy of the approximated vibration responses an a-posteriori measure is proposed and validated, where simply supported rectangular plates are considered (Section 5.1.4). An experimental simulation of simply supported rectangular plates validates that the proposed scaling method applies to measured vibration responses under geometrically incomplete similitude conditions as well (Section 5.1.5).

5.1.1 Enhancement of the proposed scaling method to geometrically incomplete similitude

In order to distinguish structures in geometrically complete and incomplete similitude, the terms *replica* and *avatar* are used, respectively, according to [54]. Considering that the geometrical distortion is small, i.e., $\phi_a \approx \phi_b$, it can be expected that the power law in Eq. (4.3) still approximates the vibration responses of avatars sufficiently well. For example, the vibration responses of cylinder structures can be approximated by SAMSARA with a sufficient accuracy provided that an avatar cylinder is *close* to a replica cylinder [54]. In other words, the vibration responses of an avatar can be approximated by those of a replica that is *close* to the avatar. Such a replica should be as close as possible to the avatar in order to replicate the vibration responses with a sufficient accuracy, i.e., the replica has a minimum distance to the avatar. The scaling factor of such a *closest replica* equals the mean value of the geometrical scaling factors [54]. Figure 5.1 exemplifies the scaling factor relations of an avatar and its closest replica for two linearly independent scaling factors ϕ_a and ϕ_b. All replicas are located on the main diagonal of the plot. The closest replica is located at the intersection of the main diagonal and a perpendicular line through the avatar. However, all considerations made in [54] consider two geometrical scaling factors only. In Appendix A.3 it is derived that the scaling factor $\overline{\phi}_l$ of the closest replica equals the mean value for an arbitrary number N of linearly independent scaling factors as well. Thus, the scaling factor of the closest replica yields

$$\overline{\phi}_l = \frac{1}{N} \sum_{j=1}^{N} \phi_{X_j}, \tag{5.1}$$

with ϕ_{X_j} being the geometrical scaling factors of the avatar that cause geometrically incomplete similitude conditions. In order to describe the difference of the scaling factors of an avatar with respect to the scaling factor of the closest replica, the *geometrical distortion* is defined

$$\varkappa_{X_j} = \frac{\phi_{X_j}}{\overline{\phi}_l} - 1. \tag{5.2}$$

A geometrical distortion of $\varkappa_{X_j} > 0$ refers to geometrical design parameters that are scaled up to a higher extent than the closest replica, while $\varkappa_{X_j} < 0$ refers to

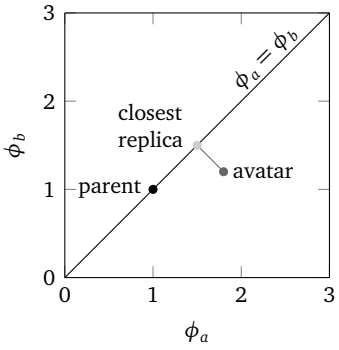

Figure 5.1: schematic illustration of a replica that is closest to an avatar

geometrical design parameters that are scaled down to a higher extent than the closest replica. The parent and all replicas have zero geometrical distortion.

Note again that the proposed enhancement of the scaling method rather approximates the vibration responses of an avatar than exactly replicates them. Nevertheless, the approximated vibration responses can be sufficiently accurate [54]. In order to validate the enhanced scaling method, the replicated vibration responses of cantilever plates obtained from the proposed scaling method are compared with calculated vibration responses and with those replicated from the scaling method SAMSARA.

5.1.2 Derivation of scaling laws of a cantilever plate

The cantilever plate (*CFFF* boundary conditions) is made from aluminum,[1] where length, width, and thickness equal 570 mm, 400 mm, and 2 mm, respectively. The scaling method SAMSARA has been applied to scale vibration responses from virtual and experimental simulations of an identical plate in [57]. Thus, this cantilever plate is a benchmark for the proposed scaling method.

The thickness ratio of the cantilever plate ξ equals 200, i.e., it exceeds the minimum value of 50 (see Section 4.2.3) and the cantilever plate can be considered thin. Two harmonic forces of $|F_1| = |F_2| = 1\,\mathrm{N}$ magnitude act at the dimensionless coordinates $(0.885a, 0.161b)$ and $(0.885a, 0.839b)$, respectively,

[1] Material properties are listed in Table 4.1 on page 60.

and cause the cantilever plate to vibrate. The force F_2 is phase-shifted by 30°. In complex notation both forces read $F_1^{(\mathrm{p})} = (1 + 0\mathrm{i})\,\mathrm{N}$ and $F_2^{(\mathrm{p})} = (0.87 + 0.50\mathrm{i})\,\mathrm{N}$. The surface-averaged squared RMS vibration velocities $\overline{\tilde{v}^2}$ are considered the vibration responses, which includes the scaling of the frequencies. An FE model is set up in analogy to that from Section 4.2.

The excitation force magnitudes are assumed to be scaled by factor ϕ_F, while length, width, and thickness are scaled by the factors ϕ_a, ϕ_b, and ϕ_t, respectively. Recall that length and width of a thin plate can be scaled by a different factor than its thickness, while complete geometrical similitude conditions are still kept [31]. Thus, only the scaling factors of the length ϕ_a and of the width ϕ_b cause incomplete similitude conditions. As a consequence, only ϕ_a and ϕ_b need to be considered for the mean scaling factor $\overline{\phi_l}$. Performing an LSA in analogy to Section 4.2.2 and taking the mean values of the powers yields the scaling law for the frequencies

$$\frac{f^{(\mathrm{a})}}{f^{(\mathrm{p})}} = \phi_f = \overline{\phi_l}^{\,-2} \phi_t^1 \tag{5.3}$$

and the scaling law for the mean squared velocity

$$\frac{\overline{\tilde{v}^2}^{(\mathrm{a})}}{\overline{\tilde{v}^2}^{(\mathrm{p})}} = \phi_{\overline{v}} = \phi_t^{-4} \phi_F^2. \tag{5.4}$$

The powers of the geometrical scaling factors equal those obtained in Chapter 4 since the LSA uses the closest replica, which is in complete similitude. The scaling law for the frequencies of SAMSARA equals Eq. (5.3) and the scaling law for the mean squared velocity of SAMSARA reads [57]

$$\frac{\overline{\tilde{v}^2}^{(\mathrm{a})}}{\overline{\tilde{v}^2}^{(\mathrm{p})}} = \phi_{\overline{v}} = \left(\phi_a \phi_b \phi_t \phi_f\right)^{-2} \phi_F^2, \tag{5.5}$$

where ϕ_f is obtained from Eq. (5.3). The scaling laws of SAMSARA are derived in Appendix A.4. Assuming perfect geometrical similitude conditions ($\phi_a = \phi_b$) and inserting Eq. (5.3) into Eq. (5.5) yields Eq. (5.4). Thus, the scaling laws derived from the proposed scaling method equal the scaling laws of SAMSARA for perfect geometrical similitude conditions.

5.1.3 Validation of the scaling laws of cantilever plates by virtual simulations

The scaling laws are validated by replicating the vibration velocities of the three avatars defined in Table 5.1. These avatars are identical to those in [57]. The vibration velocities are

- calculated from an FE model of each avatar,
- replicated by Eqs. (5.3) and (5.4), i.e., by the proposed scaling method, and
- replicated by Eqs. (5.3) and (5.5), i.e., by SAMSARA [57].

Table 5.1: geometrical dimensions, scaling factors, and geometrical distortion of the avatars

	dimensions in mm			**scaling factors**				**geometrical distortion**	
avatar	a	b	t	ϕ_a	ϕ_b	ϕ_t	$\overline{\phi}_l$ *)	$\varkappa_a$	$\varkappa_b$
a1	285	240	2	0.50	0.60	1.0	0.55	−0.091	+0.091
a2	342	200	2	0.60	0.50	1.0	0.55	+0.091	−0.091
a3	355	260	2	0.62	0.65	1.0	0.64	−0.031	+0.016

*): $\overline{\phi}_l$ equals the mean value of ϕ_a and ϕ_b according to Eq. (5.1)

The results are illustrated in Figure 5.2. The vibration velocities replicated by the proposed scaling method equal those of SAMSARA, although the scaling laws given by Eqs. (5.4) and (5.5) differ. This is caused by the fact that Eq. (5.5) becomes Eq. (5.4) for complete similitude conditions and that length and width of the avatars are only weakly distorted. Compared to the calculated vibration velocities, the replicated vibration velocities of the avatars a1 and a2 are approximated by the scaling laws, but they somewhat differ due to incomplete geometrical similitude conditions. Nevertheless, the replicated vibration velocity levels agree well with those from the calculation at some peaks, e.g., at 58 Hz and 54 Hz of avatar a1 and a2, respectively, see top and middle of Figure 5.2. Avatar a3 is close to complete similitude conditions since it is distorted to a lesser extent than the avatars a1 and a2, see Table 5.1. In this case, the replicated vibration velocities agree well with those from the

calculation, see bottom of Figure 5.2. The vibration behavior of the avatars is still similar to that of the parent and the vibration velocities are replicated sufficiently well. As a consequence, both scaling methods approximate the vibration velocities of the avatars in the same manner.

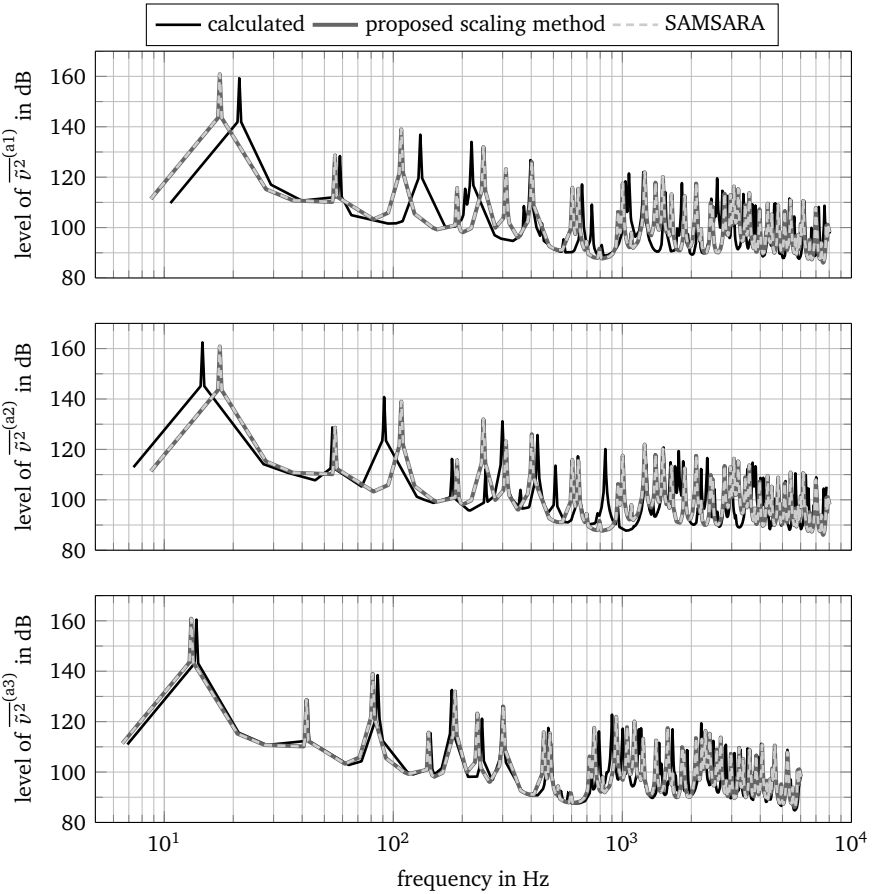

Figure 5.2: level of the mean squared velocity $\overline{\tilde{v}^2}$ versus frequency (re $5 \cdot 10^{-8}\,\mathrm{m\,s^{-1}}$), top: avatar a1, middle: avatar a2, bottom: avatar a3

5.1.4 Assessment of the accuracy of replicated vibration responses of simply supported rectangular plates

This section aims at developing a-posteriori measures to determine the accuracy of replicated vibration responses with respect to calculated vibration responses. The accuracy is assessed by two different distances between the replicated and the calculated vibration responses. The first distance is the HAUSDORFF distance d_{H} [61], which is already used in [57, 58] to assess the accuracy of replicated vibration responses. However, it has not been validated that the HAUSDORFF distance is actually an appropriate measure for this purpose. The second distance is the MAHALANOBIS distance [98], whose mean $\overline{d}_{\mathrm{M}}$ and maximum $d_{\mathrm{M,\,max}}$ values are considered. The HAUSDORFF distance and the MAHALANOBIS distance are introduced in Appendix A.5, see page 148 et seqq. Taking the MAHALANOBIS distance into account is motivated by the following consideration: An accurately replicated vibration response qualitatively and quantitatively matches the corresponding calculated vibration response. Consequently, the replicated and the calculated vibration responses are correlated. Distances between correlated data can be misleading if the distances are based on a EUCLIDEAN distance such as the HAUSDORFF distance. A principle example in Appendix A.5 illustrates the difference between the EUCLIDEAN distance and the MAHALANOBIS distance. It is subsequently shown that the MAHALANOBIS distance is appropriate to assess the accuracy of the MSTA of simply supported rectangular plates, while the HAUSDORFF distance can be misleading. In addition, the proposed scaling method is compared with SAMSARA in terms of the aforementioned distances.

The parent rectangular plate from Section 4.2 with all edges simply supported is considered and the MSTA of avatars are replicated using Eqs. (4.16), (4.17), and (5.1). The scaling law for the natural frequencies of SAMSARA equals Eq. (5.3) and the scaling law for the MSTA of SAMSARA reads

$$\frac{Sh_{\mathrm{T}}^{2\,(\mathrm{a})}}{Sh_{\mathrm{T}}^{2\,(\mathrm{p})}} = \phi_{Sh} = (\phi_a \phi_b)^{-1} \left(\phi_t \phi_f\right)^{-2}, \tag{5.6}$$

which is derived in Appendix A.4.

The avatars are scaled in length and width by factors between 0.5 and 2.5. The thickness ratio $\xi = 124$ of the parent is kept for all avatars to ensure that the geometrically incomplete similitude conditions are exclusively caused by different scaling factors in length and width. The scaling factor ratio ϕ_a/ϕ_b ranges from 0.2 to 5.0. This leads to geometrical distortions $\varkappa_a$ and $\varkappa_b$ between -0.67 and $+0.67$. Figure 5.3 illustrates the geometrical distortion $\varkappa$ versus the scaling factor ratio ϕ_a/ϕ_b. The curves are symmetric with respect to the $\varkappa = 0$ axis, i.e., $\varkappa_b = -\varkappa_a$ and vice versa. Nevertheless, both values, i.e., $\varkappa_a$ and $\varkappa_b$, are subsequently given for the sake of completeness. Figure 5.4 illustrates the

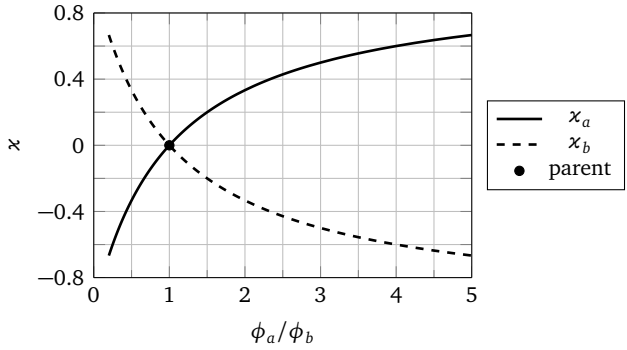

Figure 5.3: geometrical distortion in length and width versus the scaling factor ratio

rectangular plates with the maximum geometrical distortions and the parent. The aspect ratios significantly differ from that of the parent. It can be expected that the vibration behavior significantly differs as well. The MSTA of 272 avatars and 17 replicas are calculated from the FE model that is also used in Section 4.2.

Figure 5.5 illustrates the MSTA of two avatars a1 and a2 with geometrical distortions of $\varkappa_a^{(\mathrm{a1})} = -0.273$, $\varkappa_b^{(\mathrm{a1})} = +0.273$, $\varkappa_a^{(\mathrm{a2})} = +0.482$, and $\varkappa_b^{(\mathrm{a2})} = -0.482$. Both scaling methods replicate the MSTA in the same manner. The MSTA levels replicated from SAMSARA are approximately 1 dB higher for avatar a2 than those replicated from the proposed scaling method. However, this difference is much smaller compared to the difference between the replicated and calculated MSTA levels of avatar a2. The replicated frequencies of avatar a2 are underestimated, e.g., the first peak of the MSTA is replicated at 14.7 Hz, but calculated at 38.3 Hz. The replicated MSTA levels tend to be overestimated up to frequencies of 300 Hz and rather underestimated between 300 Hz and

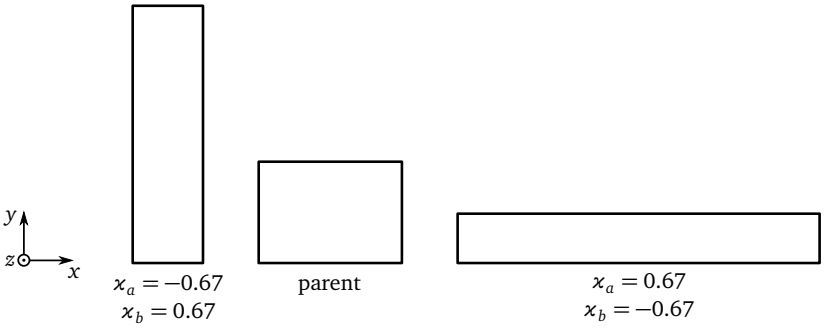

Figure 5.4: rectangular plates with the maximum geometrical distortions and parent rectangular plate

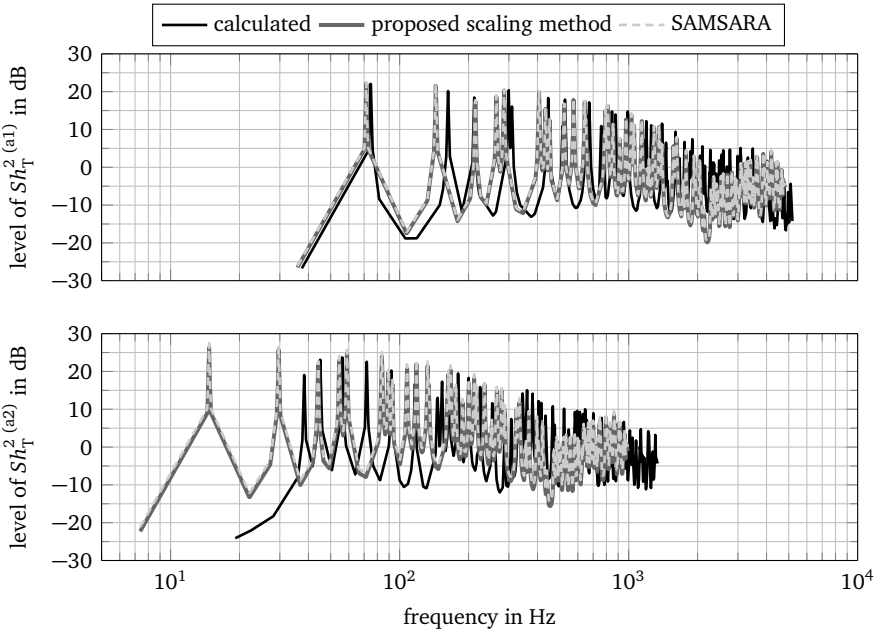

Figure 5.5: level of the MSTA versus frequency (re $6.25 \cdot 10^{-6}\,\mathrm{m^4\,N^{-2}\,s^{-2}}$), top: avatar, a1 bottom: avatar a2

700 Hz, e.g., the replicated MSTA level is approximately 7–8 dB higher at the first peak and approximately 5.6–6.6 dB lower in the vicinity of 367 Hz than the calculated MSTA levels. In contrast, the replicated MSTA of avatar a1 agrees sufficiently well with the calculated MSTA up to 2 000 Hz, while it deviates to a higher extent above 2 000 Hz. The MSTA of avatar a1 is replicated more accurately than the MSTA of avatar a2. Thus, the distance measures of avatar a1 should be smaller than those of avatar a2. As can be seen from the distance measures listed in Table 5.2 the mean and the maximum MAHALANOBIS distances of avatar a1 are smaller than those of avatar a2 by a factor of approximately 6 at least. However, the HAUSDORFF distance of avatar a1 is higher than that of avatar a2, thus, stating the opposite of the MAHALANOBIS distances.

Table 5.2: geometrical distortion and distance measures (in $m^4\,N^{-2}\,s^{-2}$) of the MSTA of the avatars a1 and a2

	geometrical distortion		**proposed scaling method**			**SAMSARA**		
avatar	$\varkappa_a$	$\varkappa_b$	d_H	$d_{\mathrm{M,\,max}}$	$\overline{d}_\mathrm{M}$	d_H	$d_{\mathrm{M,\,max}}$	$\overline{d}_\mathrm{M}$
a1	−0.273	+0.273	372.9	1.04	0.05	372.9	0.83	0.05
a2	+0.482	−0.482	347.2	6.66	0.16	347.2	11.21	0.20

In order to resolve this contradiction, the distance measures of all 272 avatars and 17 replicas are plotted versus the geometrical distortion, see Figures 5.6 through 5.8. The geometrical distortions $\varkappa_a$ and $\varkappa_b$ are plotted on separate abscissas. The ascending direction of the axis is shown by arrows for the sake of clarity. All distance measures are zero at zero geometrical distortion, which can be expected due to complete similitude conditions. An increasing geometrical distortion, i.e., $\varkappa_a$ and $\varkappa_b$ differ from zero, causes all distance measures to increase. The HAUSDORFF distance increases discontinuously, while the MAHALANOBIS distances increase continuously for an increasing geometrical distortion. The different behaviors of the distance measures are caused by the fact that the HAUSDORFF distance and the scaling factor ratio ϕ_a/ϕ_b correlate by $r_{d_\mathrm{H}} = -0.39$, whereas the MAHALANOBIS distances correlate only by $r_{\overline{d}_\mathrm{M}} = -0.14$ and $r_{d_{\mathrm{M,\,max}}} = -0.15$. r_{d_H}, $r_{\overline{d}_\mathrm{M}}$, and $r_{d_{\mathrm{M,\,max}}}$ denote PEARSON's correlation coefficient [5] of the HAUSDORFF distance, the mean and the maximum MAHALANOBIS distance, respectively.

Figures 5.7 and 5.8 show that the mean and the maximum MAHALANOBIS distance equal approximately 0.05 and approximately 1.0, respectively, unless the geometrical distortion exceeds ±0.4. Higher geometrical distortion causes the distances to rapidly increase. As a consequence, an approximately equal accuracy of the replicated MSTA can be expected within a geometrical distortion of ±0.4. Thus, the proposed scaling method and SAMSARA can be used to scale rectangular plates in geometrically incomplete similitude for geometrical distortions up to ±0.4. However, the mean and the maximum MAHALANOBIS distance of SAMSARA increase to a higher extent for geometrical distortions that are higher than ±0.4. For such geometrical distortions a significant difference between the replicated and the calculated MSTA can be expected anyway, e.g., see avatar a2 in Figure 5.5. A similar conclusion can be drawn for the driving point admittance as well, see Appendix C on pages 170 et seqq. Thus, the proposed scaling method and SAMSARA can be used to replicate the MSTA and the driving point admittance up to a permissible geometrical distortion of ±0.4.

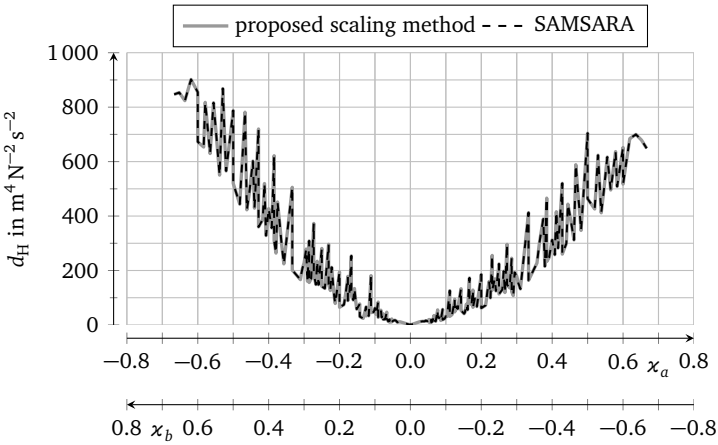

Figure 5.6: HAUSDORFF distance of the MSTA magnitudes versus the geometrical distortion

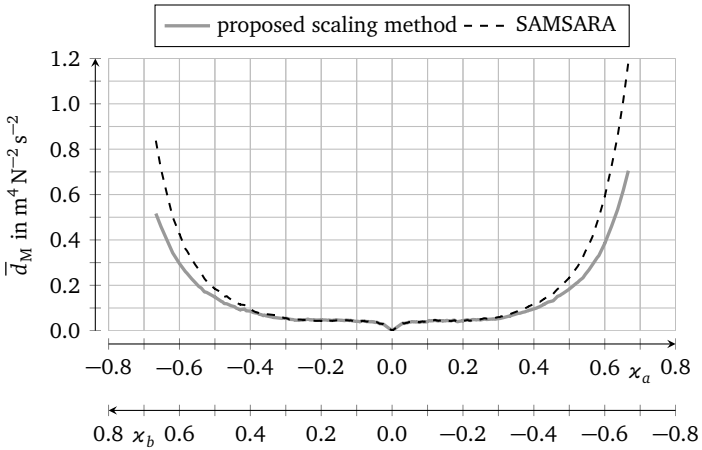

Figure 5.7: mean MAHALANOBIS distance of the MSTA magnitudes versus the geometrical distortion

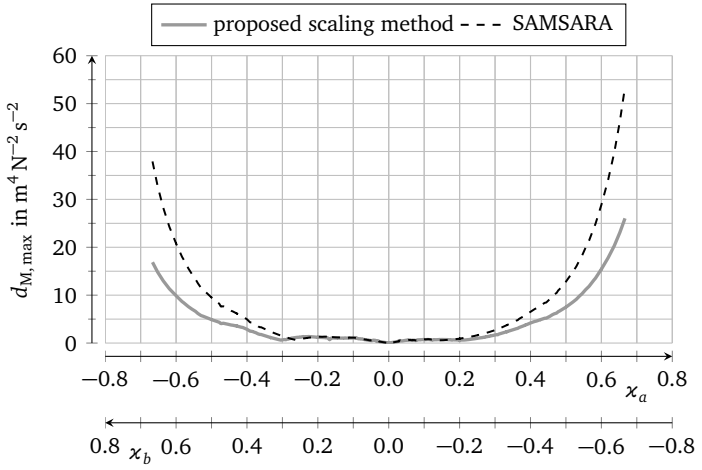

Figure 5.8: maximum MAHALANOBIS distance of the MSTA magnitudes versus the geometrical distortion

5.1.5 Validation of the scaling laws by experimental simulations

The enhancement of the scaling method proposed in Section 5.1.1 has been validated for measured vibration velocities of cantilever plates [57]. The avatars are identical to those from Section 5.1.3. However, the paper [57] lacks analyses of the similitude of mode shapes, modal damping, and loss factors as well as of the replicated natural frequencies. Therefore, this section considers two avatars of the simply supported parent rectangular plate used in Section 4.2.4, see Table 5.3. The avatars are made from aluminum as well and their material properties are listed in Table C.3 on page 173. The scaling factor ϕ_a is chosen to ensure similitude of the mode shapes at least up to the third mode [91]. The similitude of the mode shape order, of the modal damping, and of the loss factor are assessed in the same manner as in Section 4.2.4. The natural frequencies are replicated using the scaling law given by Eq. (5.3).

Similitude of the loss factors and of the modal damping

The ANOVA is based on 2111 loss factors that are measured as described in Section 4.2.4. Again, the loss factors significantly differ on a confidence level of 95%. Thus, the loss factors of the parent and of the avatars are not in similitude. The boxplot in analogy to Figure 4.15 is shown in Figure C.8 on page 169.

The ANOVA of the modal damping shows that the avatars are in similitude to the parent unless more than the first 7 modes are taken into account. Figure C.9 on page 169 shows the $1-p$ value versus the cumulative mode number in analogy to Figure 4.17. The results obtained for the avatars a1 and a2 agree with those obtained for the replicas in Section 4.2.4. Thus, the conclusions drawn in Section 4.2.4 can be drawn in analogy for the avatars a1 and a2.

Table 5.3: geometrical dimensions and scaling factors of the specimens

specimen		dimensions in mm			scaling factors				
		a	b	t	ϕ_a	ϕ_b	ϕ_t	$\overline{\phi}_l^{*)}$	l_{bl} in mm
parent	p	870	620	5.0	1.0	1.0	1.0	1.0	25
avatar	a1	375	310	5.0	0.43	0.5	1.0	0.466	10
avatar	a2	375	310	2.5	0.43	0.5	0.5	0.466	20

*): $\overline{\phi}_l$ equals the mean value of ϕ_a and ϕ_b according to Eq. (5.1)

Similitude of the mode shape order

The MAC matrices of the avatars a1 and a2 are illustrated in Figure 5.9 for the first 10 modes. The first three mode shapes of the avatars a1 and a2 are in similitude to those of the parent, as intended due to the choice of the scaling factor ϕ_a. The mode shapes 4 and 5 of the avatar a1 are interchanged. At higher mode numbers, the mode shape algorithm fails to fit a physically meaningful mode shape due to increased damping. The mode shapes 4 and 5 of avatar a2 are interchanged as well, but the MAC values are somewhat decreased due to increased damping. Mode shape 6 of the parent corresponds to mode shape 7 of the avatar a2 and at higher mode numbers the mode shape algorithm fails to fit a physically meaningful mode shape due to increased damping [91]. Based on the MAC analysis it is expected that the natural frequencies of the first three modes can be accurately replicated, while deviations can be expected at higher mode numbers.

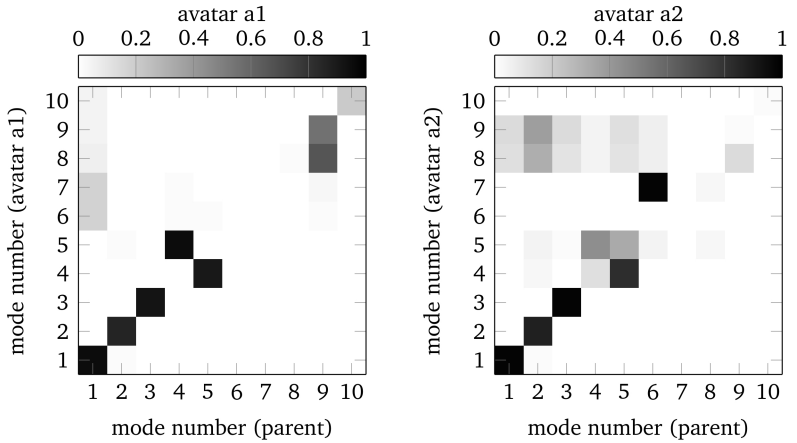

Figure 5.9: MAC analysis of the avatars a1 and a2, MAC values are indicated by the grayscale

Replicating the natural frequencies

Figure 5.10 shows the replicated natural frequencies versus the measured natural frequencies of the avatars. The natural frequencies are replicated using Eq. (5.3). Again, only the modes with a physically meaningful mode shape are considered. The error of the replicated natural frequencies ε_f is calculated

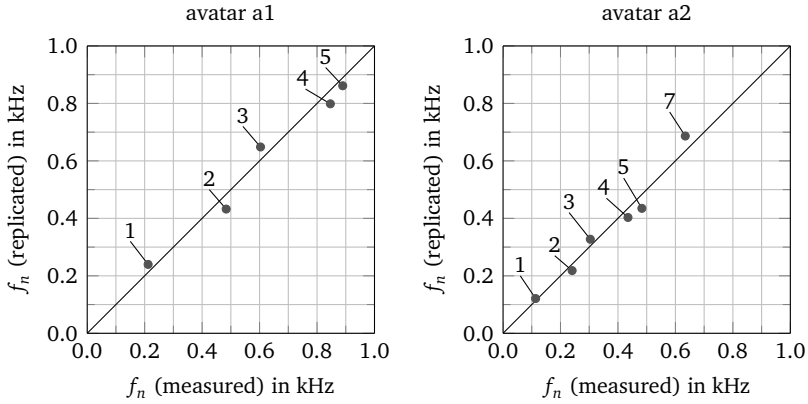

Figure 5.10: replicated natural frequencies versus measured natural frequencies of the avatars a1 and a2, numbers denote the mode numbers

according to Eq. (4.20). The averaged error yields 7.4% and 8.0% for the avatars a1 and a2, respectively. This is slightly higher than the error of the replicated natural frequencies of the replicas investigated in Section 4.2.4. The maximum error yields 10% and 13% for the avatars a1 and a2, respectively, which is approximately equal to the maximum error of the replicated natural frequencies of the replicas. Thus, the natural frequencies of the avatars can be replicated sufficiently well, although the natural frequencies are replicated from the closest replica. The scaling law of Eq. (4.16) can be validated for rectangular plates in geometrically incomplete similitude as well [91].

5.2 Scaling laws of a size range of gear boxes

This section derives scaling laws for the natural frequencies of the size range of gear boxes shown in Figure 1.1 on page 15. This size range of gear boxes serves as a representative example of a size range of drive technology systems. It is obtained from the manufacturer SEW-EURODRIVE GmbH & Co KG. The gear boxes are available in various sizes and with various gear transmission ratios and permissible torques. Various components can be mounted to the gear box such as an electrical machine, see Figure 5.11, in order to assemble a drive train. The size range of gear boxes is, thus, part of a so-called *kit* of drive trains [3].

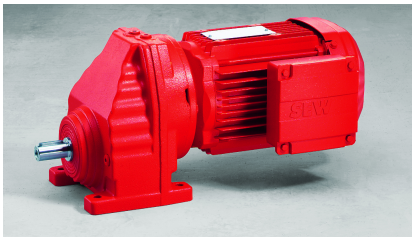

Figure 5.11: gear box of the size range shown in Figure 1.1 with an electrical machine attached, reprint permitted by SEW-EURODRIVE GmbH & Co KG [99]

In order to determine the natural frequencies of the entire size range of gear boxes, a scaling law is derived and used to replicate the natural frequencies of two avatar gear boxes from those of a parent gear box. The natural frequencies are particularly relevant in early stages of product design processes to improve the design of the gear box housings. For example, it must be avoided that natural frequencies agree with gear mesh frequencies in order to avoid increased noise and vibrations of the gear boxes. Thus, the natural frequencies need to be replicated sufficiently well as early as possible during product design processes. Based on discussions with industry, the natural frequencies are considered sufficiently well estimated for practical engineering purposes unless the deviation exceeds approximately 20%. Consequently, the scaling laws need to replicate the natural frequencies with a maximum permissible error of 20% compared with calculated natural frequencies.

A virtual model of each gear box is built (Section 5.2.1) and the scaling law of the natural frequencies is derived from the virtual model of the parent gear box (Section 5.2.2). Virtual simulations are performed to validate that the scaling laws replicate the natural frequencies of avatars sufficiently well (Section 5.2.3). An experimental modal analysis is performed to validate that the proposed scaling method can be used to replicate measured natural frequencies as well (Section 5.2.4). Finally, it is outlined how the proposed scaling method can be enhanced towards replicating the natural frequencies of gear boxes with different assemblies attached to the gear box (Section 5.2.5).

5.2.1 Virtual models of the size range of gear boxes

The virtual models incorporate only the main geometrical features of the gear boxes. Figure 5.12 illustrates the parent gear box and its main geometrical features. The *gear box housing* is a simplified geometry of the gear box housing shown in Figure 1.1 on page 15. Shafts, bearings, and gears are not considered for this virtual model. An assembly that is attached to the *input flange*, e.g., the electrical machine shown in Figure 5.11, is considered in Section 5.2.5 only. The gear box can be mounted on a foundation by four feet (labeled *foot mount* in Figure 5.12). An *inner plate* and an *inner wall* stiffen the gear box housing. The inner wall and the *truncated cone* support the output shaft.

Three individual FE models are set up to model the size range of gear boxes, see Figure 5.13. Each gear box is defined by 30 geometrical design parameters, see Table C.4 and Figure C.14 on page 174 et seq. The gear boxes are assumed to be made from cast iron[2] with a YOUNG'S modulus of $E = 1 \cdot 10^{11}\,\mathrm{N\,m^{-2}}$, a POISSON'S ratio of $\mu = 0.26$, and a mass density of $\rho = 7\,200\,\mathrm{kg\,m^{-3}}$.

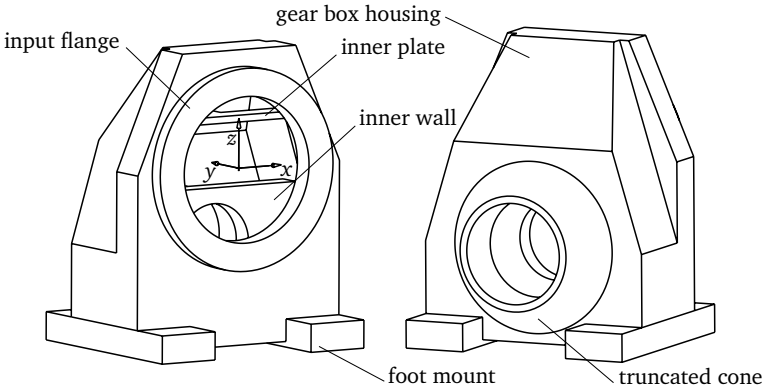

Figure 5.12: 3-D sketches of the simplified parent gear box of the size range

The geometry of the gear boxes is meshed with SOLID186 elements of tetrahedral shape. The SOLID186 elements comprise quadratic shape functions and are recommended to mesh structures like the gear boxes [87]. The initial elements' sizes of the parent, avatar a1, and avatar a2 equal 15 mm, 11.5 mm, and 20 mm,

[2] Note that cast iron is chosen since it is the common material for such gear boxes. However, the simplified geometry is not suitable for casting.

respectively. The mesh is then refined to ensure at least two elements in wall thickness direction. Mesh improvement is applied to optimize the shape of the tetrahedral elements. Refer to Appendix B.3 on pages 158 et seq. in conjunction with [87] for further details on meshing. The gear box feet are considered mounted on a foundation by setting the displacements of the feet to zero on a length of $l_{\mathrm{f,supp}}$ (see Figure C.14 on page 175) in x-, y-, and z- direction. The first 20 natural frequencies and mode shapes are obtained from a numerical modal analysis, where a BLOCK-LANCZOS algorithm is used [86, 87].

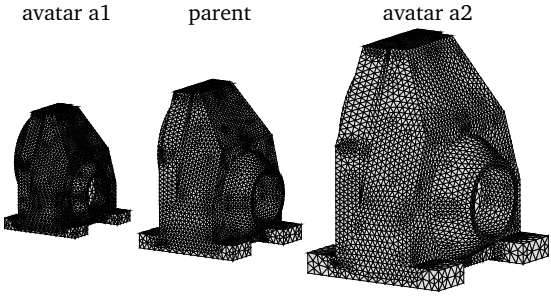

Figure 5.13: FE models of the size range of gear boxes

Figure 5.14 illustrates the natural frequencies of the three gear boxes versus the mode number. All natural frequencies of the avatars a1 and a2 are higher and lower, respectively, than those of the parent. This can be expected since avatar a1 is scaled down, while avatar a2 is scaled up with respect to the parent. The

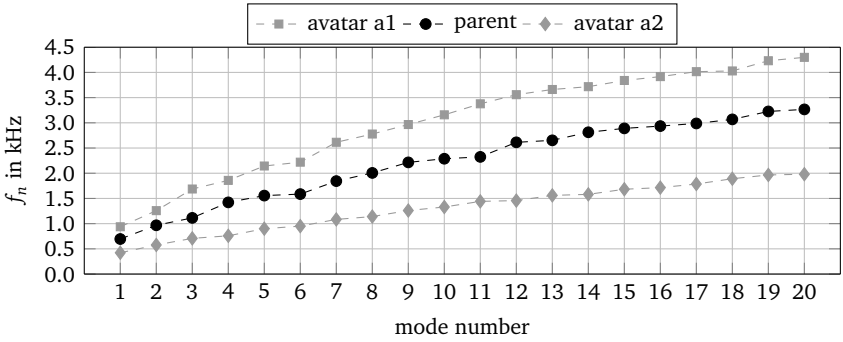

Figure 5.14: natural frequencies of the gear boxes versus mode number

mode shape order is assessed by MAC analyses using ANSYS. Due to the different sizes of the gear boxes the FE nodes of the avatars must be mapped to the FE nodes of the parent. However, not all FE nodes can accurately be mapped to the parent since the avatars are in geometrically incomplete similitude. As a consequence, some MAC values are decreased although the mode shapes look similar upon visual inspection. For example, the inner plates of the avatars a1 and a2 exclusively vibrate at the modes 7 and 8, respectively. These modes correspond to mode 7 of the parent as can be seen from Figure C.15 on page 177, but the corresponding MAC values equal 0.50 and 0.39 only. As a consequence, the MAC analyses only analyze whether the MAC values on the main diagonal of the MAC matrix tend to be higher than those on the off-diagonals instead of analyzing whether the MAC values are close to one. Figure 5.15 shows the MAC matrices of the mode shapes of the avatars a1 and a2 with respect to the mode shapes of the parent. The mode shape order of avatar a1 is considered

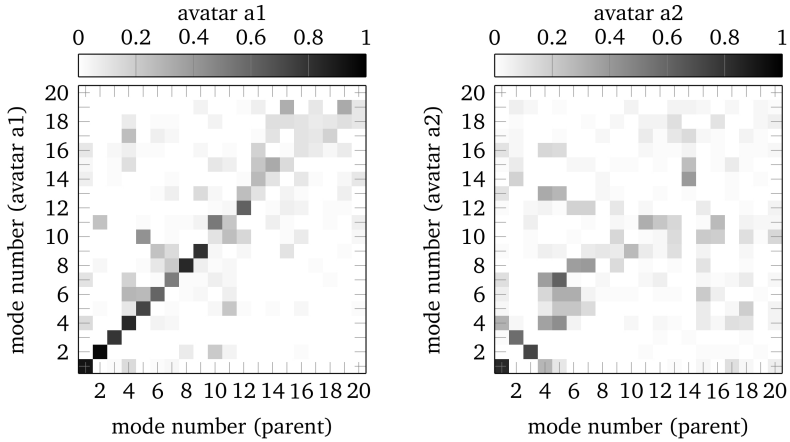

Figure 5.15: MAC matrices of the avatars a1 and a2, MAC values are illustrated by the grayscale

in similitude to that of the parent up to the 9th mode since the MAC values on the main diagonal are higher than those on the off-diagonals. In contrast, the MAC values on the main diagonal at the modes 10 through 20 tend to be similar to the MAC values on the off-diagonals. Thus, the mode shape order of the modes 10 through 20 is not in similitude to that of the parent. For avatar a2, only the first mode is in similitude to the parent mode, while the mode shape

order changes at higher modes. Thus, the higher modes are not in similitude to those of the parent. As shown in Section 5.1.5, scaling laws still replicate the natural frequencies of rectangular plates sufficiently well, although the mode shape order is not in similitude. Thus, it is assumed that a scaling law for the natural frequencies of the size range of gear boxes is still applicable as well.

5.2.2 Derivation of a scaling law for the natural frequencies

The scaling law for the natural frequencies is derived from the approach proposed in Section 5.1.1, i.e., the natural frequencies of the avatars a1 and a2 are approximated by those of gear boxes that are in complete geometrical similitude. Performing an LSA of the parent gear box with all geometrical dimensions simultaneously altered by ±2% yields

$$\frac{f_n^{(\mathrm{a})}}{f_n^{(\mathrm{p})}} = \phi_f = \overline{\phi}_l^{-1}. \tag{5.7}$$

Again, a variation of ±2% during the LSA is found suitable to derive the scaling law. The scaling factor of the natural frequencies ϕ_f is inversely proportional to the scaling factor of the geometrical dimensions $\overline{\phi}_l$. This agrees with the scaling laws for the natural frequencies of the rectangular plates and the GCU if all geometrical dimensions are scaled by the same factor, see Eqs. (4.16) and (4.25), respectively. In order to apply the scaling law given by Eq. (5.7) to the avatars a1 and a2, the scaling factor $\overline{\phi}_l$ must be determined for each avatar. Recall that only scaling factors of such design parameters are used to calculate the scaling factor $\overline{\phi}_l$ that are in geometrically incomplete similitude. As can be seen from Table C.4 on page 174, most of the design parameters of the avatars a1 and a2 are scaled by factors 0.70 and 1.40, respectively. These design parameters are considered in complete similitude, whereas the remaining design parameters are considered in incomplete similitude. The latter are hereafter referred to as *distorted design parameters* and the corresponding scaling factors are hereafter referred to as *distorted scaling factors*. Table 5.4 lists the geometrical distortions $\varkappa_{X_j}$ of the distorted design parameters, which are calculated according to Eq. (5.2). Note that the distorted design parameter $l_{y,\mathrm{bottom}}$ is in incomplete similitude for avatar a1 only, i.e., the geometrical distortion of $l_{y,\mathrm{bottom}}$ equals zero for avatar a2. The distorted design parameters of the avatars a1 and a2 are scaled in a different manner, e.g., the geometrical distortion of the thickness t is different for the avatars a1 and a2. The geometrical distortions do not exceed

Table 5.4: geometrical distortion x_{X_j} of the distorted design parameters, refer to Table C.4 and Figure C.14 on page 174 et seq. for a description of the distorted design parameters

avatar	$h_{z,\mathrm{f}}$	$l_{y,\mathrm{fl}}$	$d_{\mathrm{fl,i}}$	$d_{\mathrm{fl,o}}$	$l_{z,\mathrm{top}}$	$l_{y,\mathrm{top},2}$
a1	0.116	0.340	−0.107	−0.107	−0.107	0.005
a2	−0.323	−0.222	0.015	0.015	0.015	0.151
avatar	$l_{x,\mathrm{bottom}}$	$l_{y,\mathrm{bottom}}$	t	$l_{y,\mathrm{wall}}$	$l_{z,\mathrm{plate}}$	t_{plate}
a1	−0.107	−0.107	0.005	0.116	−0.163	0.116
a2	0.083	0.000	−0.188	0.557	0.218	−0.323

±0.4, which is found the maximum permissible geometrical distortion for rectangular plates in Section 5.1.4. Thus, it is expected that the developed scaling method can be used to replicate the natural frequencies of the gear boxes with a sufficient accuracy as well.

As proposed in Section 5.1.1 the scaling factor $\overline{\phi}_l$ of the avatars a1 and a2 can be determined from the mean of the distorted scaling factors. Taking the mean of all distorted scaling factors yields

$$\overline{\phi}_l^{(\mathrm{a1})} = 0.90 \quad \text{and} \quad \overline{\phi}_l^{(\mathrm{a2})} = 1.48, \tag{5.8}$$

for the avatars a1 and a2, respectively. The natural frequencies can then be replicated by inserting the scaling factors of Eq. (5.8) into Eq. (5.7). This approach assumes that all natural frequencies scale with the mean distorted scaling factor. However, it can be expected that not all distorted scaling factors affect each natural frequency (and mode shape) in the same manner. For example, Figure 5.16 illustrates the displacement of avatar a1 at the modes 3 and 11. Note that the lower part of the input flange and the truncated cone vibrate at the modes 3 and 11, respectively, while other parts of the avatar a1 vibrate to a much lesser extent. As a consequence, the input flange geometry and the truncated cone geometry mainly affect the vibration behavior at the modes 3 and 11, respectively. It can be expected that the geometrical distortion of the input flange geometry, e.g., due to the distorted design parameter $l_{y,\mathrm{fl}}$ (see Table 5.4), affects mode 3 to a higher extent than mode 11. In other words, mode 3 is more *sensitive* to geometrical distortions of the input flange

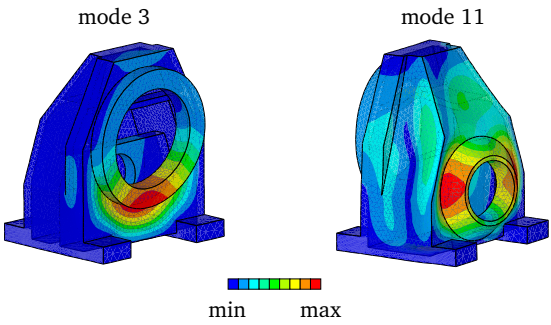

Figure 5.16: displacements of avatar a1 at modes 3 and 11, each mode shape is scaled with respect to its maximum

geometry than mode 11. This implies that the scaling factor $\overline{\phi}_l$ should rather be determined from the one distorted design parameter that causes the highest variation of each natural frequency, i.e., the distorted design parameter with the highest sensitivity magnitude. Thus, it is assumed that the scaling behavior of each natural frequency (and mode shape) depends mainly on the most sensitive distorted design parameter, while the other distorted design parameters affect the scaling behavior to a much lesser extent.

In order to prove the previous hypothesis, an LSA of the parent gear box is performed and the scaling factor $\overline{\phi}_l$ is determined. Each distorted design parameter is altered separately by ±2% during the LSA. The sensitivities are calculated from Eq. (4.13). Table C.5 on page 176 lists the sensitivities α_{X_j,f_n} of the distorted design parameters and Figure 5.17 shows them as a bar plot, where the mode number is illustrated by the grayscale. Three conclusions can be drawn from Figure 5.17:

- Each distorted design parameter affects the natural frequencies in a different manner, e.g., the effect of the length $l_{y,\mathrm{top},2}$ on the natural frequencies is much smaller than that of the length $l_{x,\mathrm{bottom}}$.
- One distorted design parameter can affect each natural frequency in a different manner, e.g., the inner flange diameter $d_{\mathrm{fl,i}}$ has a much higher effect on natural frequency f_7 than on the other natural frequencies.
- One distorted design parameter can affect the natural frequencies in a different direction of influence, e.g., increasing the length $l_{x,\mathrm{bottom}}$ causes

the natural frequency f_2 to increase, while it causes all other natural frequencies to decrease.

Taking the most sensitive distorted design parameter at each natural frequency, i.e., the distorted design parameter with maximum sensitivity magnitude $|\alpha_{X_j,f_n}|$, yields one distorted scaling factor for each natural frequency. Calculating their mean values yields

$$\overline{\phi}_l^{(\mathrm{a1})} = 0.80 \quad \text{and} \quad \overline{\phi}_l^{(\mathrm{a2})} = 1.59 \tag{5.9}$$

for the avatars a1 and a2, respectively. The mean values $\overline{\phi}_l^{(\mathrm{a1})}$ and $\overline{\phi}_l^{(\mathrm{a2})}$ are taken instead of the scaling factor at each natural frequency since one common scaling factor has always been considered for all natural frequencies so far and, furthermore, the frequency dependence of the powers of the scaling laws has been neglected as well, see Section 4.2.2. The underlying assumption is that the scaling behavior is independent from frequency, which is validated in the following section.

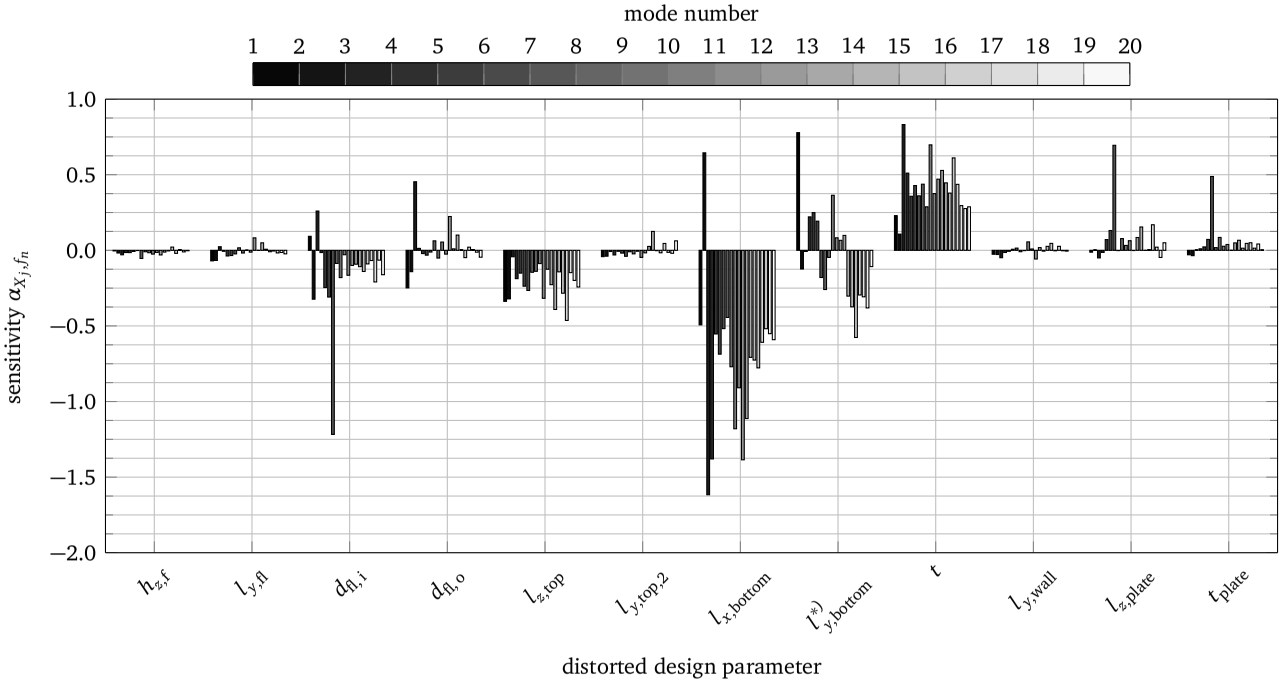

Figure 5.17: sensitivities of the natural frequencies of the parent gear box with respect to the distorted design parameters, $^{*)}$: design parameter $l_{y,\text{bottom}}$ is a distorted design parameter for avatar a1 only

5.2.3 Validation of the scaling law by virtual simulations

Figure 5.18 shows the natural frequencies replicated from Eqs. (5.7) and (5.8) as well as from Eqs. (5.7) and (5.9) versus the calculated natural frequencies of the avatars a1 and a2. The replicated natural frequencies of the avatars a1 and a2 tend to be underestimated and overestimated, respectively, by both scaling laws given by Eqs. (5.7) and (5.8) as well as given by Eqs. (5.7) and (5.9). Using the most sensitive distorted design parameters, i.e., using the scaling factors of Eq. (5.9), improves the accuracy of the replicated natural frequencies compared to those obtained from the scaling factors of Eq. (5.8). This can be seen by the fact that the black diamonds in Figure 5.18 are closer to the main diagonal (plotted as a solid line) than the gray circles.

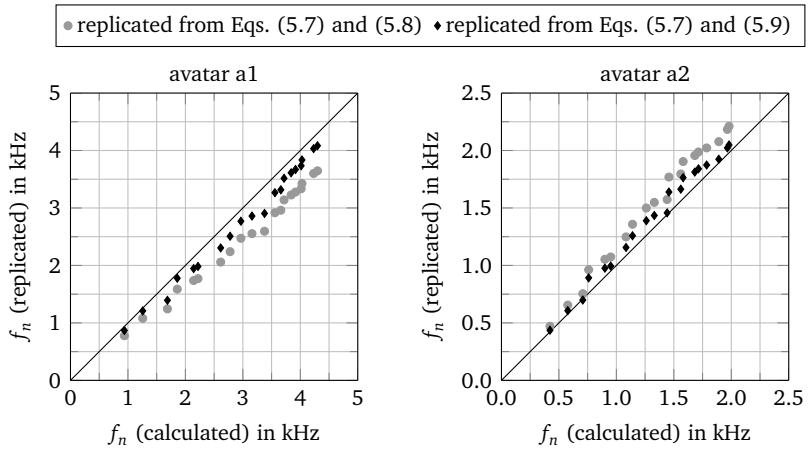

Figure 5.18: replicated natural frequencies versus calculated natural frequencies of the avatars a1 and a2

The error ε_f of the replicated natural frequencies is calculated from Eq. (4.20) on page 69 and the mean and maximum values are listed in Table 5.5. Taking the most sensitive distorted design parameter to calculate the scaling factor $\overline{\phi}_l$ instead of all distorted design parameters causes the error ε_f to decrease. The maximum error decreases from more than 26% to approximately 17.5%. The latter is smaller than 20%, which has been proposed as the permissible error of the natural frequencies at the beginning of this section, see page 116. The

mean error is smaller than 10%. Thus, the natural frequencies of the avatars a1 and a2 can be replicated sufficiently well by the scaling law of Eq. (5.7) and the scaling factors of Eq. (5.9).

Table 5.5: mean and maximum values of the error ε_f in %

	all distorted scaling factors		most sensitive distorted scaling factors	
avatar	mean	max.	mean	max.
a1	17.9	26.28	8.1	17.4
a2	15.1	26.84	6.7	17.5

5.2.4 Validation of the scaling law by experimental simulations

The natural frequencies of the three gear boxes of the size range illustrated in Figure 1.1 on page 15 are obtained from experimental modal analyses. Again, the gear boxes are considered without attached assemblies, gears, shafts, and bearings. The aim of this section is to validate whether a mean scaling factor suffices to replicate measured natural frequencies of the gear boxes within the permissible error of 20%, which has been proposed at the beginning of this section, see page 116. First, the similitude of the mode shape order is validated using MAC analyses. The similitude of the modal damping is analyzed by an ANOVA in analogy to the analyses in Section 4.2.4. Second, appropriate scaling factors need to be defined. Determining a geometrical scaling factor of the gear boxes, e.g., based on the most sensitive distorted design parameter like in Section 5.2.2, is considered too time-consuming due to the complex geometry of the gear boxes. Instead, the actual scaling factor of each natural frequency ϕ_{f_i} is calculated and the mean value of these scaling factors $\overline{\phi}_f$ is used to replicate *all* natural frequencies of the avatars from those of the parent

$$f_n^{(\mathrm{a})} = \overline{\phi}_f f_n^{(\mathrm{p})}. \tag{5.10}$$

Figure 5.19 shows the test stand. The gear boxes are mounted on four pneumatic springs to achieve free boundary conditions. The pneumatic springs are screwed to a foundation. A roving hammer test is performed to measure transfer functions between 22 excitation points and one response point in all three global coordinate directions. Details of the experimental setup are described in Appendix B.4 on page 159 et seqq.

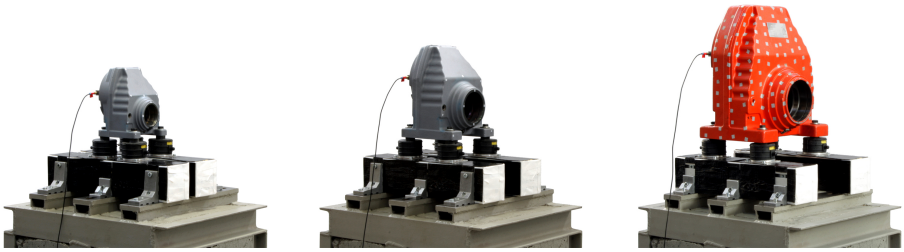

Figure 5.19: gear boxes mounted on the test stand by four pneumatic springs, left: avatar a1, middle: parent, right: avatar a2

Nine mode shapes of the parent gear box are identified and matched to those of the avatars by a visual inspection of the mode shapes. However, the parent mode shapes 6 and 7 cannot be matched to mode shapes of avatar a1, and the parent mode shapes 3 and 5 cannot be matched to mode shapes of avatar a2. These mode shapes are omitted during further analyses of the corresponding avatars. Figure 5.20 illustrates the MAC matrices of the avatars a1 and a2. The MAC values on the main diagonal tend to be higher than the MAC values on the off-diagonals. Thus, the mode shape order of the avatars a1 and a2 are considered in similitude to that of the parent. However, some MAC values on the off-diagonals are increased, e.g., the MAC value of the parent mode shape 2 and the avatar a2 mode shape 4 equals 0.54. Such increased MAC values are caused by the fact that mode shapes might hardly be distinguishable. For example, the vibration responses are not measured on the inner plate and the inner wall. Mode shapes with significant vibrations of the inner plate or the inner wall are poorly sampled and, thus, can hardly be distinguished. The natural frequencies of rectangular plates can be replicated sufficiently well, although the mode shapes are not in similitude, see Section 5.1.5. Thus, it is expected that the natural frequencies of the gear boxes can be replicated with sufficient accuracy as well despite the fact that the mode shapes are not perfectly in similitude. The ANOVA of the modal damping is performed in analogy to that in Section 4.2.4. It can be concluded that the modal damping is in similitude, unless more than the first two modes are taken into account. Figure C.16 on page 177 shows the $1-p$ value versus the cumulative mode number.

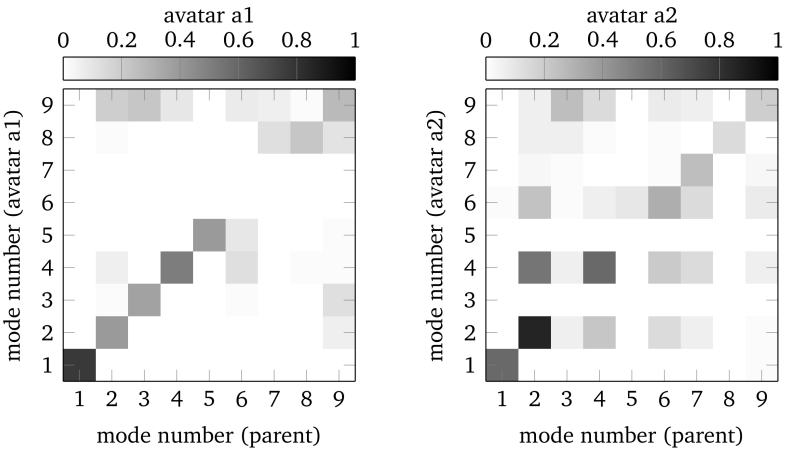

Figure 5.20: MAC matrices of the measured mode shapes of the avatars a1 and a2, MAC values are illustrated by the grayscale

Calculating the actual scaling factors of the measured natural frequencies and taking their mean values yields

$$\overline{\phi}_f^{(\mathrm{a1})} = 1.38 \quad \text{and} \quad \overline{\phi}_f^{(\mathrm{a2})} = 0.64 \tag{5.11}$$

for the avatars a1 and a2, respectively. The actual scaling factors of each natural frequency are listed in Table C.6 on page 178. The natural frequencies of the avatars are replicated from those of the parent using Eq. (5.10) and the scaling factors of Eq. (5.11). Figure 5.21 illustrates the replicated natural frequencies of both avatars versus the measured natural frequencies, where the numbers indicate the mode numbers. The error ε_f is calculated from Eq. (4.20). The natural frequencies of the avatars a1 and a2 can be replicated with a mean error of approximately 4% and 6%, respectively, and with a maximum error of 8.7% and 15.9%, respectively. These values are approximately equal to those of the replicated natural frequencies of the virtual models, see Section 5.2.3, and lower than the permissible error of 20% proposed at the beginning of this section, see page 116. Thus, the measured natural frequencies can be replicated by a mean scaling factor sufficiently well.

In order to apply the proposed scaling method in practice, the scaling factor $\overline{\phi}_f$ must be appropriately determined. If the scaling factor $\overline{\phi}_f$ is determined from an analysis of the geometry, e.g., by computer aided design, or from a sensitivity analysis of the actual gear boxes in analogy to Section 5.2.3, it is expected that Eq. (5.7) can be used to replicate the natural frequencies. However, an experimental validation of Eq. (5.7) for the size range of gear boxes will be subject to future research.

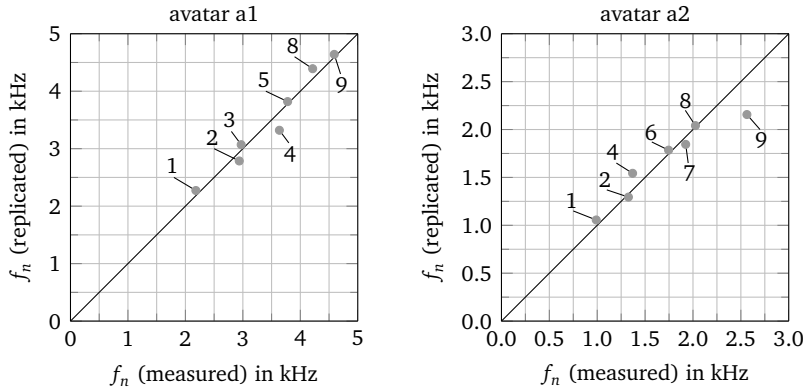

Figure 5.21: replicated natural frequencies versus measured natural frequencies of the avatars a1 and a2, numbers refer to mode numbers

5.2.5 Enhancing the scaling laws to kits

Finally, it is outlined how the natural frequencies can be scaled depending on different assemblies attached to the input flange. In order to show the principle, an assembly such as the electrical machine shown in Figure 5.11 on page 116 is considered attached to the input flange of the parent gear box. It is assumed that only the additional mass due to the attached assembly affects the natural frequencies, while the additional stiffness and any vibrations of the assembly itself are neglected. Such a simplified scaling approach can be useful during early stages of the product design process to roughly estimate how the natural frequencies of the parent gear box changes for different assemblies attached to the input flange. In practice, it is necessary to investigate the vibration behavior of the gear box including the attached assembly in more detail, but this is out of the scope of this thesis.

The attached assembly of the parent gear box is considered a lumped mass m, which is located at the distance l_m (with respect to the global y-direction), see Figure 5.22. The parent gear box is again fixed at the four feet in agreement to Section 5.2.1. A MASS21 element is placed at the distance l_m in the FE model. It is connected to the input flange by defining a *multipoint constraint*, which is the recommended modeling approach for this purpose [87]. Appendix B.3 (see pages 158 et seq.) describes the FE model setup in more detail. The mass $m = 6\,\mathrm{kg}$ and the distance $l_m = 80\,\mathrm{mm}$ are obtained from a technical report of SEW-EURODRIVE GMBH & CO KG. The MASS21 takes rotational inertias into account as well. They are set to $I_x = I_z = ml_m^2 = 6 \cdot 0.08\,\mathrm{kg\,m^2} = 0.48\,\mathrm{kg\,m^2}$ and $I_y = 0$.

According to Eq. (4.3) the scaling law for the natural frequencies of the parent gear box with a lumped mass attached can be proposed

$$\frac{f_n^{(\mathrm{a})}}{f_n^{(\mathrm{p})}} = \phi_f = \phi_m^{\alpha_{m,f}}. \tag{5.12}$$

An LSA of the parent gear box is performed, where the mass m is altered by ±2%. Again, a variation of ±2% is found sufficient to derive the scaling law.

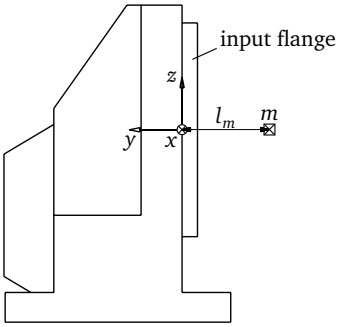

Figure 5.22: sketch of the parent gear box with mass m at distance l_m

Figure 5.23 illustrates the power $\alpha_{m,f}$ versus the natural frequencies of the parent. At the natural frequencies 1 through 3 the power is between −0.21 and −0.17, whereas it is between approximately −0.05 and 0.00 at the natural

frequencies 4 through 20. Such a behavior of the power $\alpha_{m,f}$ differs from that of the powers derived for the geometrical design parameters, see Section 4.2.2. The mean powers at the natural frequencies 1 through 3 and 4 through 20 equal -0.18 and -0.01, respectively. Thus, only the natural frequencies 1 through 3 tend to be sensitive to the mass m, while the natural frequencies 4 through 20 are hardly affected by the mass m. The mode shapes 1 through 3 are *global* mode shapes, i.e., the entire gear box vibrates, while the mode shapes 4 through 20 are rather *local* mode shapes, i.e., only certain parts of the gear box vibrate such as the inner plate. Only the global mode shapes are affected by the mass m and, thus, their scaling behavior differs from that of the local mode shapes, which are hardly affected by the mass m. In other words, the mass impedance increases with an increasing frequency [9], which causes the natural frequencies 1 through 3 to be more sensitive to the mass m than the natural frequencies 4 through 20. As a consequence, the scaling behavior of the natural frequencies depends on frequency as well, which is seen by the fact that the power $\alpha_{m,f}$ depends on frequency. A frequency-dependent scaling law is also proposed by PETRONE [58], where scaling laws of stiffened cylinders under incomplete similitude conditions are investigated.

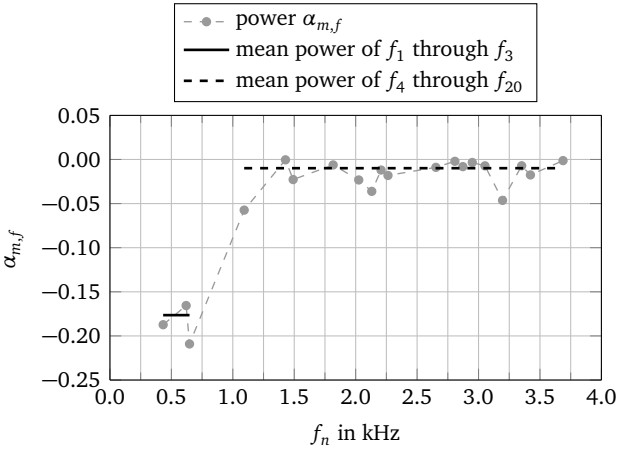

Figure 5.23: power $\alpha_{m,f}$ and mean values versus the natural frequencies of the parent gear box

Thus, the scaling law for the natural frequencies 1 through 3 reads

$$\frac{f_{1\ldots3}^{(\mathrm{a})}}{f_{1\ldots3}^{(\mathrm{p})}} = \phi_{f_{1\ldots3}} = \phi_m^{-0.18}, \tag{5.13}$$

whereas the scaling law for the natural frequencies 4 through 20 becomes

$$\frac{f_{4\ldots20}^{(\mathrm{a})}}{f_{4\ldots20}^{(\mathrm{p})}} = \phi_{f_{4\ldots20}} = \phi_m^{-0.01} \approx 1. \tag{5.14}$$

In order to validate Eqs. (5.13) and (5.14), two avatar gear boxes a1-m and a2-m are defined, where the mass is scaled by factors of 0.5 and 2.0, respectively. The similitude of the mode shape order is again assessed using MAC analyses. Figure 5.24 illustrates the MAC matrices. The mode shape order of the avatar a1-m is in similitude to that of the parent. The mode shape order of avatar a2-m is in similitude to that of the parent as well, except for the modes 2 and 3, which are interchanged. However, not all MAC values on the main diagonal equal 1 and some MAC values on the off-diagonals are increased, e.g., at the parent mode 17 and avatar a1-m mode 18. Recall again that the natural frequencies can be replicated sufficiently well, although the mode shape order is not in similitude (see Sections 5.1.5 and 5.2.3). Thus, it is expected again that the scaling laws are still applicable.

Figure 5.25 shows the replicated natural frequencies versus the calculated natural frequencies of the avatars. The error ε_f is calculated according to Eq. (4.20). The mean values of the error ε_f yield 3.5% and 4.5% for the avatars a1-m and a2-m, respectively, and the maximum values are 13.5% and 18.3%, respectively. The error of the replicated natural frequencies is again smaller than the permissible error of 20%, which has been proposed at the beginning of this section, see page 116. Thus, the proposed scaling method can be used to replicate the natural frequencies of the parent gear box with different masses attached to the input flange. However, a more precise analysis of gear boxes with assemblies attached to the input flange requires improved scaling methods, which will be subject to future research.

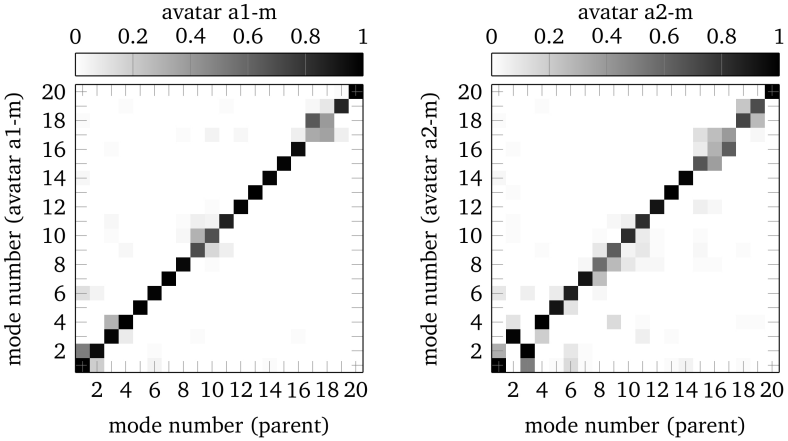

Figure 5.24: MAC matrices of the avatars a1-m and a2-m, MAC values are illustrated by the grayscale

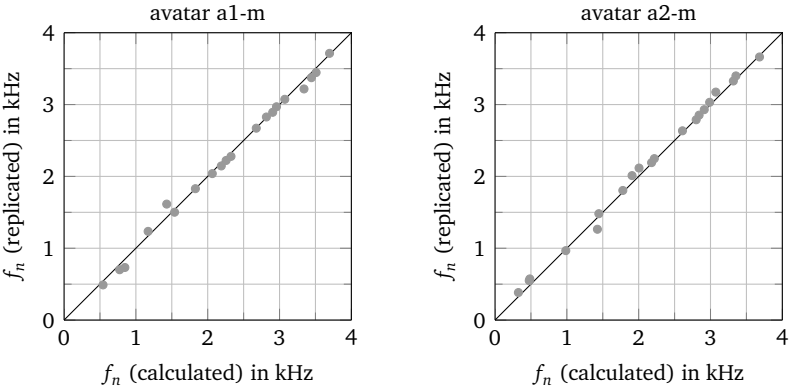

Figure 5.25: replicated natural frequencies versus calculated natural frequencies of the avatars a1-m and a2-m

5.3 Summary of similitudes and sensitivities for incomplete similitude conditions

The scaling method proposed in Chapter 4 is enhanced to geometrically incomplete similitude conditions in this chapter. An approximation method is developed that uses the closest replica to replicate the vibration responses of an avatar. The scaling factor of the closest replica equals the mean scaling factor of such design parameters that cause geometrically incomplete similitude conditions. Virtual simulations show that the enhanced scaling method replicates the vibration responses of rectangular plates up to geometrical distortions of ±0.4 sufficiently well. Comparing the replicated vibration responses of the developed scaling method with those of the scaling method SAMSARA shows that the scaling method SAMSARA replicates the vibration responses of rectangular plates up to the same geometrical distortion of ±0.4 with sufficient accuracy as well. In order to assess the accuracy of the replicated vibration responses, the MAHALANOBIS distance is introduced. It is validated that the MAHALANOBIS distance appropriately assesses the accuracy of replicated vibration responses in a-posteriori analyses, while other distance measures such as the HAUSDORFF distance can be misleading. The enhanced scaling method is validated in an experimental simulation, where simply supported rectangular plates in geometrically incomplete similitude are investigated. It is found that the natural frequencies of the simply supported rectangular plates can still be replicated sufficiently well, although the mode shape order of the avatars differs from that of the parent.

A scaling law is derived for the natural frequencies of a size range of gear boxes. The scaling behavior of the natural frequencies is found to depend mainly on the one distorted design parameter that causes the highest variation of the natural frequencies. The scaling law incorporates a mean scaling factor, which is calculated from the distorted design parameters with a maximum sensitivity magnitude of each natural frequency. Virtual and experimental simulations validate that the natural frequencies can be replicated with a mean error of approximately 4–8% using the mean scaling factor, which is considered sufficiently accurate. However, an appropriate method to determine the mean scaling factor from the experimental models of the gear boxes needs to be developed. Various lumped masses are attached to the input flange of the gear boxes, which represent additional assemblies such as electrical machines. It is

demonstrated that the natural frequencies can be replicated by the developed scaling method depending on the mass attached to the input flange. However, the scaling law becomes frequency-dependent, but the natural frequencies are still replicated sufficiently well. Thus, the developed scaling method can be enhanced towards kits.

6 Summary and conclusions

Noise and vibration engineering requires efficient methods to derive scaling laws from virtual simulations in order to efficiently design size ranges and kits, or to reliably replicate the vibration responses of a structure from those of a scaled prototype. Thus, a new scaling method is developed in this thesis that efficiently derives scaling laws, particularly, for incomplete similitude conditions. Section 6.1 summarizes the main results of this thesis and Section 6.2 outlines future research.

6.1 Summary and concluding remarks

The new scaling method is developed in four consecutive steps as shown in Figure 1.2 on page 18. In analogy to Figure 1.2, Figure 6.1 summarizes the main results of each step.

The *potential analysis* step shows that similitude analysis and SA can actually be combined and three application scenarios are deduced, where both methods benefit from each other (see Figure 6.1). In the *method development* step, the new scaling method is proposed, which combines similitude analysis with SA. A scaling law for complete similitude conditions is considered a power law and its powers are directly calculated from an SA of a virtual model. Due to the combination of similitude analysis and SA, scaling laws can be derived without manual derivations and without choosing an appropriate regression model. Thus, the developed scaling method is considered more efficient than scaling methods from literature. The scaling laws of rectangular plates equal those from literature, which verifies the new scaling method. Local and global vibration responses of replica rectangular plates and of replica GCU are accurately replicated from those of the parent structures provided that complete similitude conditions persist. Even if a replica is not in perfectly geometrical similitude to the parent, its vibration responses can still be replicated sufficiently well unless the thickness ratio of the replica is smaller than 50. However, complete similitude of the damping is found to be essential to replicate vibration responses with a sufficient accuracy, particularly, vibration response functions such as the MSTA obtained from experimental simulations. In order to determine whether

step	main results	main conclusions
I. potential analysis	Aplication scenarios for the new scaling method: 1) directly derive scaling laws from virtual models 2) prioritize design parameters to be used for scaling laws 3) combination of 1) and 2)	- similitude analysis and sensitivity analysis can actually be combined
II. method development	- The proposed scaling method uses a power law, and the powers are calculated from a sensitivity analysis. - Scaling laws of rectangular plates equal those from literature. - Scaling laws can be used to replicate global and local vibration responses of rectangular plates and of a generic car undercarriage. - Complete similitude conditions persist unless the thickness ratio ξ is smaller than 50 or the mode shape order or the dampings differs.	- proposed scaling method is verified and validated - proposed scaling method is more efficient than those from literature
III. method enhancement	- The proposed scaling method is enhanced to geometrically incomplete similitude conditions by using a closest replica to replicate the vibration responses of an avatar. - Scaling laws of rectangular plates are not exact, but sufficiently accurate unless a geometrical distortion of ±0.4 is exceeded. - The MAHALANOBIS distance appropriately assesses the accuracy of replicated vibration responses.	- proposed scaling method applies to incomplete similitude conditions - proposed scaling method is sufficiently accurate
IV. method application	- The proposed scaling method replicates the natural frequencies of the gear boxes sufficiently well. - The scaling behavior of the natural frequencies is mainly determined by the most sensitive distorted design parameter. - The proposed scaling method replicates the natural frequencies for a gear box with various masses attached as well.	- proposed scaling method is sufficiently accurate - proposed scaling method can be enhanced towards kits

Figure 6.1: overview of the main results and main conclusions of this thesis

structures are in complete similitude, MAC analyses and ANOVA of the damping are used in a-posteriori analyses, which is particularly relevant for replicating vibration responses obtained from experimental simulations.

In the third step, see Figure 6.1, the proposed scaling method is enhanced towards incomplete similitude conditions. The enhanced scaling method replicates the vibration responses of a structure in geometrically incomplete similitude (*avatar*) from those of the closest replica. Experimental simulations show that the natural frequencies of simply supported avatar rectangular plates can be replicated with a sufficient accuracy by the enhanced scaling method, although some mode shapes are interchanged. Virtual simulations of simply supported rectangular plates and cantilever plates validate that local and global vibration responses of avatars can be replicated sufficiently well from the closest replica unless a geometrical distortion of ±0.4 is exceeded. The accuracy of the replicated vibration responses can be appropriately assessed by the MAHALANOBIS distance in a-posteriori analyses, whereas the HAUSDORFF distance can be mis-

leading. Benchmarking the enhanced scaling method with respect to the scaling method SAMSARA [21, 22, 51–55] shows that both scaling methods replicate global and local vibration responses with the same accuracy in terms of the MAHALANOBIS distance up to a geometrical distortion of ±0.4. Thus, a geometrical distortion of ±0.4 is considered the permissible geometrical distortion not only for the scaling method developed in this thesis but also for the scaling method SAMSARA.

In the fourth step, see Figure 6.1, a scaling law for the natural frequencies of a size range of gear boxes is derived and validated by virtual and experimental simulations. The scaling behavior of the natural frequencies depends mainly on the one distorted design parameter that has the highest sensitivity magnitude with respect to the natural frequencies. Therefore, the natural frequencies can be replicated sufficiently well compared to calculated or measured natural frequencies. The scaling method is enhanced towards kits by deriving a scaling law for the natural frequencies of gear boxes with various lumped masses attached, which represent additional assemblies such as electrical machines. The scaling law depends on the frequency in this case, but the natural frequencies can still be replicated sufficiently well by the developed scaling method. Table C.7 on page 178 lists all structures including their boundary conditions, scaling factors, and vibration responses that are investigated in this thesis. In summary, the three research hypotheses proposed in Section 1.1 on page 18 et seq. can be confirmed as follows:

1. A power law, whose powers are calculated by means of SA, allows for directly deriving scaling laws from virtual simulations without any prior knowledge of the scaling behavior of the investigated structure.

2. The scaling laws accurately replicate local and global vibration responses provided that complete similitude conditions persist. In case of incomplete similitude conditions the vibration responses can be replicated from a closest replica up to a geometrical distortion of ±0.4 sufficiently well.

3. The following a-posteriori measures assess the accuracy of replicated vibration responses:

    - Complete geometrical similitude conditions can be (approximately) considered provided that the thickness ratio of plates or plate-like structures exceeds a minimum value of 50. The similitude of the

mode shape order and of the damping can be assessed by MAC analyses and ANOVA in a-posteriori analyses, respectively.

- The MAHALANOBIS distance is an appropriate measure to assess the accuracy of measured (or calculated) and replicated vibration responses.

6.2 Outline for future research

Further investigations of the scaling laws, particularly, under incomplete similitude conditions should be performed in order to further validate the scaling method developed in this thesis. For example, the GCU needs to be investigated under geometrically incomplete similitude conditions and by means of experimental simulations. The accuracy of replicated vibration responses can yet be assessed in a-posteriori analyses only, but a-priori accuracy measures need to be developed for practical applications of the developed scaling method. The replicated vibration responses are obtained in practice from the proposed scaling method only, and a comparison to calculated or measured vibration responses is not intended since the scaling laws would be redundant in this case.

The scaling method proposed in this thesis needs to be validated for other noise and vibration responses, particularly, for the radiated sound power in order to further develop the scaling method towards noise and vibration engineering. Based on the fundamental equation of machine acoustics, see Eq. (2.12), and the scaling law for the MSTA derived in this thesis, a scaling law of the radiation efficiency σ suffices to obtain a scaling law for the radiated sound power. ROBIN [59, 60] directly scales the radiation resistance matrix, while KOLLMANN [9] proposes scaling laws for the radiation efficiency of rectangular plates calculated from a method proposed by MAIDANIK [100]. Combining these scaling methods for the radiation efficiency with an SA could enhance the proposed scaling method to replicate the radiated sound power of structures. Besides noise and vibrations, the proposed scaling method can also be applied to other fields of engineering. For example, the size range of gear boxes investigated in Section 5.2 needs to fulfill other requirements such as torque or stability. Scaling these responses can be useful for future product development processes, where the scaling method serves as an engineering tool for the design and the analysis of size ranges as a whole.

Although the vibration responses obtained from experimental simulations can be scaled with a sufficient accuracy by the proposed scaling method, the scaling laws themselves can be derived from an SA of a virtual model only. *Evidence-based modeling* aims at finding virtual models from (measured) data [101]. It comprises several methods such as nonlinear time series analysis [102], symbolic regression [103], sparse linear regression [104], or deep learning [101]. Combining evidence-based modeling with the proposed scaling method can lead to a scaling method that directly derives scaling laws from data acquired in experimental simulations.

A Derivations

A.1 Derivation of the Π-products of the 2-DoF oscillator

The Π-products are derived from the dimension matrix given by Eq. (3.3), which reads

$$\begin{array}{c} \\ \mathsf{M} \\ \mathsf{L} \\ \mathsf{T} \end{array} \begin{array}{c} \begin{array}{cccccccccc} m_1 & u_1 & k_1 & m_2 & u_2 & k_2 & d_1 & d_2 & F & \tau \end{array} \\ \begin{pmatrix} 1 & 0 & 1 & 1 & 0 & 1 & 1 & 1 & 1 & 0 \\ 0 & 1 & 0 & 0 & 1 & 0 & 0 & 0 & 1 & 0 \\ 0 & 0 & -2 & 0 & 0 & -2 & -1 & -1 & -2 & 1 \end{pmatrix} \end{array}. \tag{A.1}$$

In order to obtain an identity matrix and a sub-matrix according to Eq. (2.21), GAUSSIAN elimination is performed as follows: The third row of the dimension matrix of Eq. (A.1) is divided by a factor of −2, which leads to

$$\begin{array}{c} \\ \mathsf{M} \\ \mathsf{L} \\ \mathsf{T} \end{array} \begin{array}{c} \begin{array}{cccccccccc} m_1 & u_1 & k_1 & m_2 & u_2 & k_2 & d_1 & d_2 & F & \tau \end{array} \\ \begin{pmatrix} 1 & 0 & 1 & 1 & 0 & 1 & 1 & 1 & 1 & 0 \\ 0 & 1 & 0 & 0 & 1 & 0 & 0 & 0 & 1 & 0 \\ 0 & 0 & 1 & 0 & 0 & 1 & 0.5 & 0.5 & 1 & -0.5 \end{pmatrix} \end{array}. \tag{A.2}$$

Subtracting the third row from the first row yields

$$\begin{array}{c} \\ \mathsf{M} \\ \mathsf{L} \\ \mathsf{T} \end{array} \begin{array}{c} \begin{array}{cccccccccc} m_1 & u_1 & k_1 & m_2 & u_2 & k_2 & d_1 & d_2 & F & \tau \end{array} \\ \begin{pmatrix} 1 & 0 & 0 & 1 & 0 & 0 & 0.5 & 0.5 & 0 & 0.5 \\ 0 & 1 & 0 & 0 & 1 & 0 & 0 & 0 & 1 & 0 \\ 0 & 0 & 1 & 0 & 0 & 1 & 0.5 & 0.5 & 1 & -0.5 \end{pmatrix} \end{array}. \tag{A.3}$$

The Π-products are obtained from Eq. (2.22) [23], which reads

$$\Pi_j = \frac{Q'_{j,\mathrm{b}}}{\prod_{i=1}^{K} \left(Q'_{i,\mathrm{f}}\right)^{\alpha'_{i,j}}}. \tag{A.4}$$

The free quantities (subscript f) are m_1, u_1, and k_1, while the other quantities are bounded quantities (subscript b). For example, Π_4 of Eq. (3.4) yields

$$\Pi_4 = \frac{d_1}{m_1^{0.5} u_1^0 k_1^{0.5}} = \frac{d_1}{(m_1 k_1)^{0.5}}. \tag{A.5}$$

The remaining Π-products of Eq. (3.4) can be obtained in analogy.

A.2 Modal approach for solving the governing equations of the 2-DoF oscillator

The governing equations (3.7) and (3.8) of the 2-DoF oscillator can be written in a matrix format

$$\begin{pmatrix} m_1 & 0 \\ 0 & m_2 \end{pmatrix} \begin{pmatrix} \ddot{u}_1 \\ \ddot{u}_2 \end{pmatrix} + \begin{pmatrix} d_1 & -d_1 \\ -d_1 & d_1 + d_2 \end{pmatrix} \begin{pmatrix} \dot{u}_1 \\ \dot{u}_2 \end{pmatrix} + \begin{pmatrix} k_1 & -k_1 \\ -k_1 & k_1 + k_2 \end{pmatrix} \begin{pmatrix} u_1 \\ u_2 \end{pmatrix} = \begin{pmatrix} F(\tau) \\ 0 \end{pmatrix}. \tag{A.6}$$

The short form of Eq. (A.6) reads

$$\mathbf{M}\ddot{\mathbf{u}} + \mathbf{D}\dot{\mathbf{u}} + \mathbf{K}\mathbf{u} = \mathbf{F}. \tag{A.7}$$

The following derivations are made based on [105]. Considering that the 2-DoF oscillator is weakly damped, the free vibrations can be obtained from

$$\mathbf{M}\ddot{\mathbf{u}} + \mathbf{K}\mathbf{u} = \mathbf{0}. \tag{A.8}$$

A harmonic response

$$\mathbf{u} = \hat{\mathbf{u}} \mathrm{e}^{\mathrm{i}\omega\tau} \tag{A.9}$$

is assumed, where $\hat{\mathbf{u}} = (\hat{u}_1,\ \hat{u}_2)^{\mathrm{T}}$ denotes the vector of displacement amplitudes. Inserting Eq. (A.9) into Eq. (A.8) yields

$$\left(\mathbf{K} - \omega^2 \mathbf{M}\right) \hat{\mathbf{u}} = \mathbf{0}. \tag{A.10}$$

Nontrivial solutions, i.e., $\hat{\mathbf{u}} \neq \mathbf{0}$, exist for

$$\det\left(\mathbf{K} - \omega^2 \mathbf{M}\right) = 0. \tag{A.11}$$

Equation (A.11) leads to the eigenvalues with their roots being the natural angular frequencies ω_1 and ω_2 of the 2-DoF oscillator

$$\begin{aligned}\omega_{1,2}^2 = &\frac{(k_2 m_1 + k_1 (m_1 + m_2))}{2 m_1 m_2} \\ &\pm \frac{\sqrt{(-k_2 m_1 - k_1 (m_1 + m_2))^2 - 4 k_1 k_2 m_1 m_2}}{2 m_1 m_2},\end{aligned} \tag{A.12}$$

which are calculated using WolframAlpha.[1] The corresponding eigenvectors $\mathbf{u}_1$ and $\mathbf{u}_2$ are obtained by inserting ω_1 and ω_2 into Eq. (A.10). They describe the free vibration displacements of the degrees of freedom. The eigenvectors are written into the matrix of eigenvectors

$$\mathbf{Q} = (\mathbf{u}_1, \mathbf{u}_2). \tag{A.13}$$

Applying the transformations

$$\mathbf{M}_{\text{modal}} = \mathbf{Q}^{\mathrm{T}} \mathbf{M} \mathbf{Q}, \quad \mathbf{D}_{\text{modal}} = \mathbf{Q}^{\mathrm{T}} \mathbf{D} \mathbf{Q}, \quad \mathbf{K}_{\text{modal}} = \mathbf{Q}^{\mathrm{T}} \mathbf{K} \mathbf{Q}, \tag{A.14}$$

$$\mathbf{F}_{\text{modal}} = \mathbf{Q}^{\mathrm{T}} \mathbf{F}, \tag{A.15}$$

and

$$\mathbf{u} = \mathbf{Q} \mathbf{u}_{\text{modal}}, \tag{A.16}$$

and inserting Eqs. (A.14), (A.15), and (A.16) into Eq. (A.7) yields

$$\mathbf{M}_{\text{modal}} \ddot{\mathbf{u}}_{\text{modal}} + \mathbf{D}_{\text{modal}} \dot{\mathbf{u}}_{\text{modal}} + \mathbf{K}_{\text{modal}} \mathbf{u}_{\text{modal}} = \mathbf{F}_{\text{modal}}. \tag{A.17}$$

The displacements of the 2-DoF oscillator due to the excitation force $\mathbf{F}$ yield

$$\mathbf{u} = \mathbf{Q} \mathbf{H}_{\text{modal}} \mathbf{Q}^{\mathrm{T}} \hat{\mathbf{F}} \mathrm{e}^{\mathrm{i}\Omega\tau}, \tag{A.18}$$

[1] see: https://www.wolframalpha.com

where $\hat{\mathbf{F}} = \left(\hat{F},\ 0\right)^{\mathrm{T}}$ and Ω are the vector of excitation force magnitudes and the angular excitation frequency, respectively. $\mathbf{H}_{\mathrm{modal}}$ denotes the diagonal matrix of modal transfer functions. For the j-th modal coordinate, the modal transfer function reads

$$H_{j,\mathrm{modal}} = \frac{1}{k_{j,\mathrm{modal}}} \frac{\omega_N^2}{\omega_N^2 - \Omega^2 + \mathrm{i}\delta\omega_N^2\Omega}, \tag{A.19}$$

where δ is the stiffness proportional multiplier of the damping.

A.3 Scaling factor of the closest replica

The scaling factor of the closest replica $\overline{\phi}_l$ is derived by minimizing the EUCLIDEAN distance between an avatar with the geometrical scaling factors $\phi_{X_1}^{(\mathrm{a})}, \phi_{X_2}^{(\mathrm{a})}, \ldots, \phi_{X_N}^{(\mathrm{a})}$ and the closest replica with the geometrical scaling factors $\phi_{X_1}^{(\mathrm{r})}, \phi_{X_2}^{(\mathrm{r})}, \ldots, \phi_{X_N}^{(\mathrm{r})}$. The EUCLIDEAN distance of the avatar and the closest replica reads

$$d_{\mathrm{E}} = \sqrt{\sum_{j=1}^{N} \left(\phi_{X_j}^{(\mathrm{r})} - \phi_{X_j}^{(\mathrm{a})}\right)^2}. \tag{A.20}$$

All geometrical scaling factors of a replica are equal, i.e., $\phi_{X_1}^{(\mathrm{r})} = \phi_{X_2}^{(\mathrm{r})} = \ldots = \phi_{X_N}^{(\mathrm{r})} = \overline{\phi}_l$, thus,

$$d_{\mathrm{E}}\left(\overline{\phi}_l\right) = \sqrt{\sum_{j=1}^{N} \left(\overline{\phi}_l - \phi_{X_j}^{(\mathrm{a})}\right)^2}. \tag{A.21}$$

The minimum distance is derived by setting

$$\frac{\mathrm{d}}{\mathrm{d}\,\overline{\phi}_l} d_{\mathrm{E}}\left(\overline{\phi}_l\right) \stackrel{!}{=} 0 = \frac{\sum_{j=1}^{N} \left(\overline{\phi}_l - \phi_{X_j}^{(\mathrm{a})}\right)}{\sqrt{\sum_{j=1}^{N} \left(\overline{\phi}_l - \phi_{X_j}^{(\mathrm{a})}\right)^2}}. \tag{A.22}$$

The denominator equals Eq. (A.21), where $d_{\mathrm{E}} > 0$. Setting the numerator to zero yields

$$\sum_{j=1}^{N} \overline{\phi}_l - \sum_{j=1}^{N} \phi_{X_j}^{(\mathrm{a})} = 0. \tag{A.23}$$

Thus,

$$N\overline{\phi}_l = \sum_{j=1}^{N} \phi_{X_j}^{(\mathrm{a})} \tag{A.24}$$

and finally

$$\overline{\phi}_l = \frac{1}{N} \sum_{j=1}^{N} \phi_{X_j}^{(\mathrm{a})}. \tag{A.25}$$

A.4 Scaling laws of rectangular plates from SAMSARA

This section derives the scaling laws of rectangular plates from SAMSARA. The scaling law for the natural frequencies is obtained from reference [22]. In the notation of this thesis, the scaling law of the natural frequencies reads

$$f_{m,n}^{(\mathrm{a})} = \frac{\phi_t}{\phi_l^2} f_{m,n}^{(\mathrm{p})}. \tag{A.26}$$

Setting $\phi_l = \overline{\phi}_l$ according to Eq. (5.1) yields

$$\frac{f_{m,n}^{(\mathrm{a})}}{f_{m,n}^{(\mathrm{p})}} = \phi_f = \phi_t \overline{\phi}_l^{\,-2}. \tag{A.27}$$

Equation (A.27) equals the scaling law for the natural frequencies that is derived from the proposed scaling method. The scaling law for the mean squared vibration velocities of the cantilever plate is derived from [57]. In the notation of this thesis the scaling law reads

$$v^{(\mathrm{p})} = \frac{\phi_{\mathrm{mass}} \phi_f}{\phi_F} v^{(\mathrm{a})}, \tag{A.28}$$

where ϕ_{mass} denotes the scaling factor of the mass. Rearranging Eq. (A.28) and taking the mean squared RMS velocities yields

$$\frac{\overline{\tilde{v}^2}^{(\mathrm{a})}}{\overline{\tilde{v}^2}^{(\mathrm{p})}} = \left(\frac{\phi_F}{\phi_{\mathrm{mass}} \phi_f} \right)^2. \tag{A.29}$$

The scaling factor of the mass equals $\phi_{\text{mass}} = \phi_a \phi_b \phi_t$ since the material properties remain unchanged ($\phi_\rho = 1$). Thus, Eq. (A.29) yields

$$\frac{\overline{\tilde{v}^2}^{(\text{a})}}{\overline{\tilde{v}^2}^{(\text{p})}} = \phi_{\overline{v}} = \left(\phi_a \phi_b \phi_t \phi_f\right)^{-2} \phi_F^2. \tag{A.30}$$

Equation (A.30) is used to replicate the mean squared RMS velocity of the cantilever plate in Section 5.1.2. Taking Eq. (4.24) into account yields the scaling law for the driving point admittance

$$\frac{h_{\text{F}}^{2\,(\text{a})}}{h_{\text{F}}^{2\,(\text{p})}} = \phi_{h_{\text{F}}} = \left(\phi_a \phi_b \phi_t \phi_f\right)^{-2}, \tag{A.31}$$

which is used to replicate the driving point admittance of simply supported rectangular plates. The results are given in Appendix C on pages 170 et seqq. Recall that the scaling laws tend to be independent from the rectangular plate's support, see Section 4.2.2. The MSTA reads $Sh_{\text{T}}^2 = S\overline{\tilde{v}^2}/\tilde{F}^2$, where $S = ab$ and $\phi_S = \phi_a \phi_b$ for rectangular plates. Thus, Eq. (A.30) yields

$$\frac{Sh_{\text{T}}^{2\,(\text{a})}}{Sh_{\text{T}}^{2\,(\text{p})}} = \phi_{Sh} = \left(\phi_a \phi_b\right)^{-1} \left(\phi_t \phi_f\right)^{-2}, \tag{A.32}$$

which is used to replicate the MSTA of simply supported rectangular plates in Section 5.1.4.

A.5 Distance measures to assess the accuracy of replicated vibration responses

This section introduces the HAUSDORFF distance [61], which is used in literature to assess the accuracy of replicated vibration responses [57, 58], and the MAHALANOBIS distance [98], which is exemplified for an arbitrary data set and compared with the EUCLIDEAN distance.

Considering two data sets $\mathbf{A} = \{a_1, a_2, \ldots, a_N\}$ and $\mathbf{B} = \{b_1, b_2, \ldots, b_M\}$, their bidirectional HAUSDORFF distance is defined as

$$d_{\text{H}} = \max\left(d'_{\text{H}}(\mathbf{A}, \mathbf{B}), d'_{\text{H}}(\mathbf{B}, \mathbf{A})\right), \tag{A.33}$$

where $d'_{\mathrm{H}}(\mathbf{A},\mathbf{B})$ and $d'_{\mathrm{H}}(\mathbf{B},\mathbf{A})$ are the unidirectional HAUSDORFF distances

$$d'_{\mathrm{H}}(\mathbf{A},\mathbf{B}) = \max_{a\in\mathbf{A}} \min_{b\in\mathbf{B}} \|a-b\|_2\,, \quad d'_{\mathrm{H}}(\mathbf{B},\mathbf{A}) = \max_{b\in\mathbf{B}} \min_{a\in\mathbf{A}} \|a-b\|_2\,, \tag{A.34}$$

and $\|\cdot\|_2$ denotes the EUCLIDEAN norm [61]. The HAUSDORFF distance first takes the minimum EUCLIDEAN distances between each value in **A** and **B** (and vice versa) and then takes the maximum of these minimum distances. It can be seen as the maximum mismatch of the data sets **A** and **B** [61].

EUCLIDEAN distances (including the HAUSDORFF distance) neglect correlations between the data sets **A** and **B**. The following principle example is taken from [106] to illustrate that a EUCLIDEAN distance can be misleading in case of correlated data sets. The left part of Figure A.1 illustrates two correlated data sets **A** and **B** (plotted as gray points). Data points with a constant EUCLIDEAN distance are located on a circle around the center in this example. Due to the

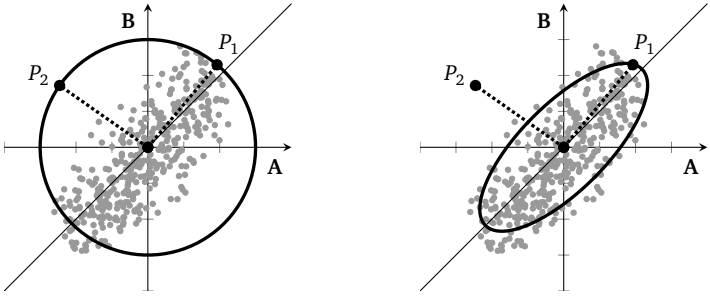

Figure A.1: distances of correlated data sets **A** and **B**, left: EUCLIDEAN distance, right: MAHALANOBIS distance

correlation between the data sets **A** and **B** the data points are more densely distributed in the vicinity of point P_1 than in the vicinity of point P_2, i.e., data points are located in the vicinity of P_1 with higher probability. Thus, P_1 is closer to the center than P_2 in terms of standard deviations. Data points with equal distance in terms of standard deviations are located on an ellipse around the center, see right part of Figure A.1. The ellipse refers to data points with constant MAHALANOBIS distance

$$d_{\mathrm{M}}(\mathbf{A},\mathbf{B}) = \sqrt{(\mathbf{A}-\mathbf{B})^T\,\boldsymbol{\Sigma}^{-1}\,(\mathbf{A}-\mathbf{B})}. \tag{A.35}$$

$\mathbf{\Sigma}^{-1}$ denotes the inverse of the covariance matrix [98]. The distance between the data sets **A** and **B** is weighted by the inverse of the covariance matrix, and different standard deviations are considered for the distance. Thus, a misleading distance due to correlated data sets is avoided.

The MAHALANOBIS distance is calculated bidirectionally as well, i.e., $d_{\mathrm{M}}(\mathbf{A},\mathbf{B})$ and $d_{\mathrm{M}}(\mathbf{B},\mathbf{A})$ are obtained. In order to assess the accuracy of the replicated vibration responses the mean MAHALANOBIS distance

$$\overline{d}_{\mathrm{M}} = \frac{1}{2N}\sum_{i=1}^{N} d_{\mathrm{M}}(\mathbf{A},\mathbf{B}) + \frac{1}{2M}\sum_{i=1}^{M} d_{\mathrm{M}}(\mathbf{B},\mathbf{A}) \tag{A.36}$$

and the maximum MAHALANOBIS distance

$$d_{\mathrm{M,\,max}} = \max\left(d_{\mathrm{M}}(\mathbf{A},\mathbf{B}), d_{\mathrm{M}}(\mathbf{B},\mathbf{A})\right) \tag{A.37}$$

are taken into account.

B Model setups

This appendix describes the setup of virtual and experimental models. The Tables B.1 through B.3 list hardware and software that is used in this thesis.

Table B.1: properties of the hardware platform for virtual simulations

property	description
processor	Intel® Xeon® CPU E3-1200 V2 3.10 GHz
architecture	64 Bit
number of cores	4
random access memory (RAM)	32.0 GB
operating system	Windows 7 Professional

Table B.2: software used for virtual simulations

virtual simulation model	software package	release
analytical model	MATLAB	R2013b
FE model	ANSYS	15.0
FE model (verification purposes only)	ABAQUS	6.13-2

Table B.3: hardware and software used for experimental simulations

data acquisition	manufacturer	hardware	software
SLDV	POLYTEC	PSV-500-3D	9.2
transfer functions	SINUS MESSTECHNIK	Soundbook	Samurai 2.6
data analysis	**manufacturer**	**hardware**	**software**
general purpose	MATHWORKS	see Table B.1	MATLAB R2017a
modal analysis (plates)	MATHWORKS	see Table B.1	MATLAB R2017a
modal analysis (gear boxes)	VIBRANT TECHNOLOGY	see Table B.1	ME'SCOPE 18.0

B.1 FE models of the rectangular plates and of the GCU

This section describes the FE model setup for the rectangular plates, the validation, and the calculation workflow. The simply supported rectangular plate (see Section 4.2) is used to exemplify the procedure, but it applies in analogy to the GCU as well (see Section 4.3). The natural frequencies are obtained from a numerical modal analysis and the vibration velocities are obtained from a harmonic analysis using the direct solution of the full system matrices [87]. The MSTA of the rectangular plates is then calculated from Eqs. (2.9) and (2.10), and the driving point admittance of the GCU is calculated from Eq. (4.24).

The FE models are set up in the FE software ANSYS, whereas the FE software ABAQUS is used for verification purposes only. The FE models of the rectangular plates and of the GCU use structured meshes of 8-node SHELL281 elements with quadratic shape functions [87]. The modal analysis uses a BLOCK-LANCZOS algorithm [86] to obtain the natural frequencies of the undamped structures. During the harmonic analysis the damping is considered a constant material loss factor. The dynamic excitation force is modeled as a pressure applied to four elements located at (a_F, b_F). The frequency spacing is narrowed around the natural frequencies, whereas it is widened between the natural frequencies in order to reduce the calculation time [87]. The FE model is validated by

1. *a mesh study*, i.e., the elements' sizes are reduced step by step and the vibration responses are compared to those of a reference FE model. The elements' sizes of the reference FE model are one order of magnitude smaller than those of the actual FE model. The mesh study aims at determining appropriate elements' sizes.

2. *an element study*, i.e., SOLID186 elements are used instead of SHELL281 and the natural frequencies are compared to each other. The element study aims at determining the difference of the natural frequencies between shell elements and solid elements.

3. *an FE software study*, i.e., the vibration responses obtained from the FE model built in ANSYS are compared to those obtained from an FE model built in ABAQUS. The FE model built in ABAQUS uses 8-node shell elements (S8R). The FE software study aims at determining the effect of different solvers on the vibration responses.

During the model validation, the MSTA is only obtained at the natural frequencies in order to reduce the calculation time. The initial elements' sizes are set to 20 mm for the mesh study, which corresponds to the common rule of 6 elements per flexural wavelength. The elements' sizes of the reference FE model are set to 1 mm, which is smaller by a factor of 20. The elements' sizes of the FE model are reduced to 10 mm and 5 mm leading to 12 and 24 elements per flexural wavelength, respectively. For elements' sizes of 10 mm the natural frequencies and the MSTA levels differ less than 1% and 0.4 dB, respectively, compared to the reference FE model. Elements' sizes of 5 mm hardly reduce the deviations between the FE model and the reference FE model. Elements' sizes of 20 mm cause the deviations to increase. Figure B.1 shows the MSTA obtained at the natural frequencies (indicated by markers) of the reference FE model and of the FE model with 10 mm elements' sizes. Note that the plotted lines are only for visualization purposes. They have no physical meaning. The curves agree well, thus, elements' sizes of 10 mm (or 12 elements per flexural wavelength) are considered sufficient for the purpose of this thesis. Note that the common rule of 6 elements per flexural wavelength is insufficient for the purpose of this thesis. This agrees with investigations by LANGER [107], where the accuracy of finite element models is investigated with respect to number of elements per flexural wavelength, element type, and experimental results.

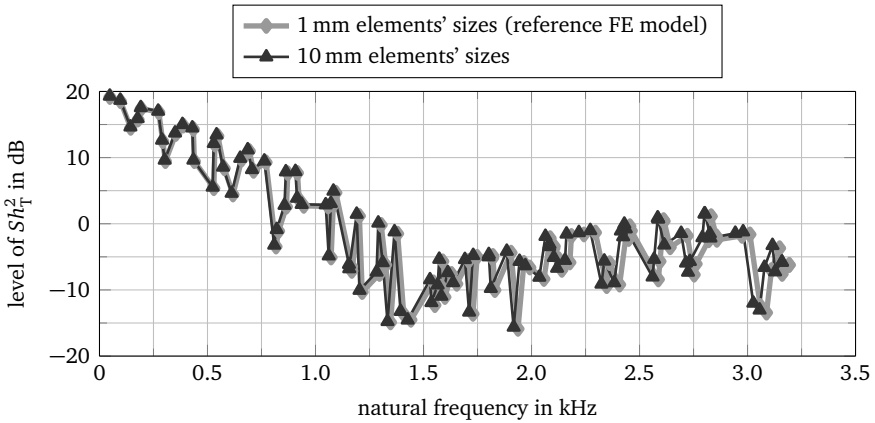

Figure B.1: MSTA level of the simply supported rectangular plate versus frequency for different element sizes (re $6.25 \cdot 10^{-6}\,\mathrm{m^4\,N^{-2}\,s^{-2}}$)

Within the element study the natural frequencies obtained from the FE model with SHELL281 elements are compared to those of an FE model with SOLID186 elements. The elements' sizes are set to 10 mm (obtained from the mesh study) and approximately 2.5 mm, respectively. The latter corresponds to 4 elements in thickness direction, which is chosen to obtain properly shaped SOLID186 elements. Figure B.2 shows the natural frequencies obtained from the FE model with SHELL281 elements versus those obtained from the FE model with SOLID186 elements. The data are located on the main diagonal of the plot, thus, the natural frequencies agree well. The maximum difference is less than 0.04%, which is considered sufficiently low. Thus, SHELL281 elements are sufficient for the purpose of this thesis.

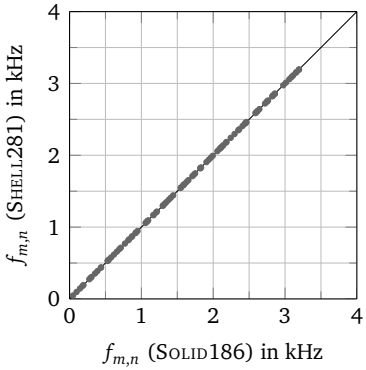

Figure B.2: natural frequencies of the simply supported rectangular plate obtained from FE models with SOLID186 and SHELL281 elements

Figure B.3 shows the MSTA levels versus the natural frequencies for the FE models built in ANSYS and ABAQUS. The elements' sizes are set to 10 mm based on the mesh study. The natural frequencies and the MSTA levels differ by 0.2% and 0.6 dB, respectively. Thus, the solver hardly affects the vibration responses. Consequently, the FE model built in ANSYS with SHELL281 elements and elements' sizes of 10 mm is considered validated.

The FE models are part of a workflow for virtual simulations that is shown in Figure B.4. The design parameters of the virtual models are defined in MATLAB. An input file for ANSYS is generated and ANSYS is executed in batch mode by

MATLAB. ANSYS runs the FE calculation, while additional macros are used to build the FE model, post-process the results, and export the result files. The result files are read by MATLAB for further processing and analysis. The analytical model of the simply supported rectangular plate given by Eqs. (2.6) and (2.11) is implemented as a MATLAB function and can be executed within this workflow as well.

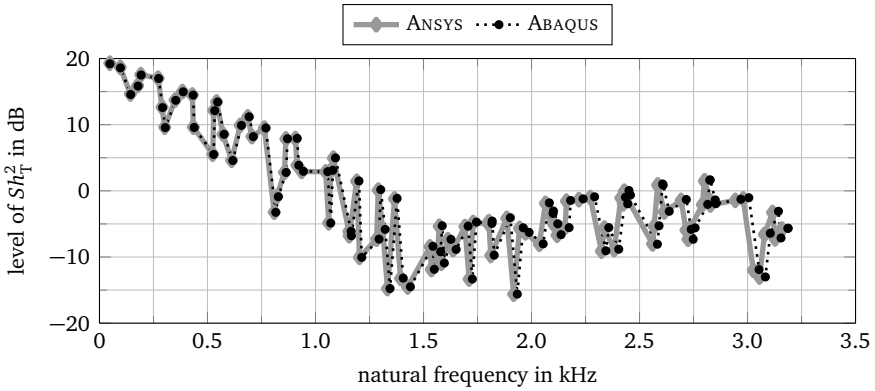

Figure B.3: MSTA level of the simply supported rectangular plate versus frequency obtained from ANSYS and ABAQUS (re $6.25 \cdot 10^{-6}\,\mathrm{m^4\,N^{-2}\,s^{-2}}$)

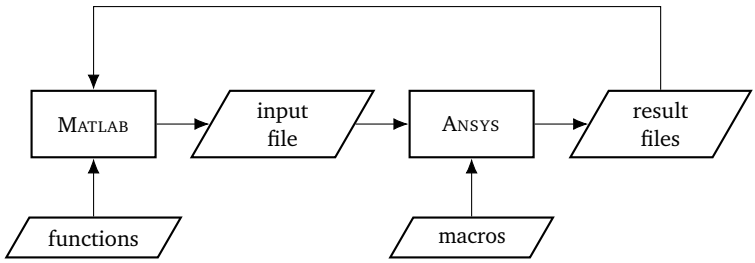

Figure B.4: workflow of an FE calculation including MATLAB and ANSYS

B.2 Experimental model of the rectangular plates

All measurements are performed at a corporate test stand of the research group SAM at Technische Universität Darmstadt (hereafter referred to as *SAMple test stand* – System reliability, Adaptive structures, and Machine acoustics test stand for primary laboratory experiments). The following paragraphs have been published in [91, 108], where an identical experimental setup is used.

Figure 4.14 illustrates the SAMple test stand for investigating simply supported rectangular plates. The vibration responses are obtained from an SLDV, which is mounted at the surrounding truss structure. The simply supported rectangular plates are mounted to the acoustic box. The setups of the specimens are shown in Figure B.5. Circumferential brackets are screwed to the acoustic box. They

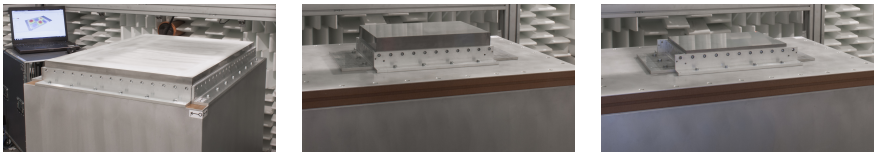

(a) parent **(b)** replica **(c)** avatar

Figure B.5: setups of the SAMple test stand for the different specimens

allow for assembling the specimens. The brackets for the scaled rectangular plates (r1, r2, a1, a2) have slots to adjust the length to that of the replicas (investigated in Section 4.2.4) or to that of the avatars (investigated in Section 5.1.5). Cylindrical pins that connect the brackets themselves and the brackets with the acoustic box ensure an accurate positioning of the brackets on the acoustic box. The simply supported boundary conditions are implemented as described in [92]. Figure B.6(a) illustrates an ideal simple support, where the transverse stiffness $k_l = \infty$ and the rotational stiffness $k_\varphi = 0$. Such a support stiffness can be approximated in practice by choosing appropriate support stiffness values, which allow for measuring the fundamental frequency with a desired accuracy with respect to an ideal simply supported rectangular plate. Higher natural frequencies are assumed to be affected by the boundary conditions to a lesser extent than the fundamental frequency. Thus, it is sufficient to consider the fundamental frequency only [92]. In order to build a simply supported rectangular plate, thin blades are bonded to the plates' edges. The blades are slotted to allow for screwing the blades on the brackets, see Figure B.6(b). The

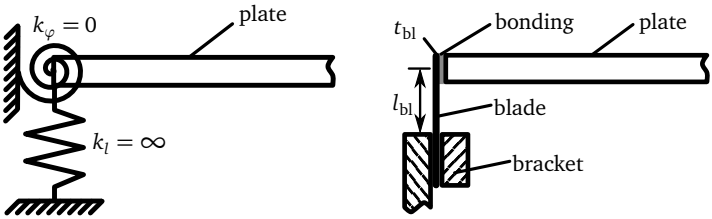

(a) ideal simple support

(b) principle of the simple support

Figure B.6: schematic view of simple supported plates

blades have a thickness of $t_{bl} = 0.5\,\text{mm}$ and the lengths l_{bl} are determined from FE calculations as described in [92]. Their values are listed in Tables 4.5 and 5.3. The natural frequencies, the mode shapes, and the modal damping of the simply supported rectangular plates are obtained from experimental modal analyses. The specimens are excited by an impact of an electrodynamic shaker (LDS V101) equipped with an impedance head (PCB 288D01) and a brass tip, see Figure B.7(a). The time-decaying vibration velocities and the excitation forces are recorded by the SLDV and fed into MATLAB, where the modal analysis functions of the MATLAB 2017a signal processing toolbox are used. The modal fit uses the least squares complex exponential method [94].

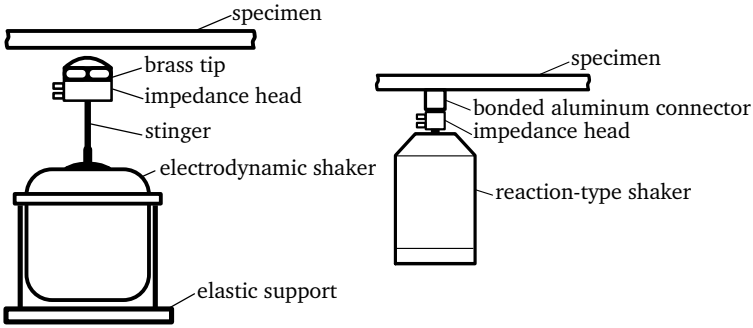

(a) impulse excitation for modal analyses

(b) sweep signal excitation for frequency response analyses

Figure B.7: illustration of the setups for the excitation of the specimens

The MSTA is obtained from a frequency response analysis using a sine sweep excitation. A reaction-type shaker with a pre-mounted impedance head (WILCOXON RESEARCH F5B/Z11) is screwed to an aluminum cube bonded to the specimen, see Figure B.7(b). The frequency of the sine sweep signal ranges from half of the specimen's fundamental frequency to 5 kHz, which is found to be the maximum possible excitation frequency of the reaction-type shaker. The vibration velocities are surface-averaged using Eq. (2.9) and the MSTA is obtained from Eq. (2.10).

B.3 FE model of the gear boxes

Three individual FE models are built to model the size range of gear boxes. The workflow for the virtual simulations of the gear boxes agrees with the workflow that is used for the rectangular plates, see Figure B.4. However, the geometrical design parameters of the gear boxes (see Table C.4) are read from an EXCEL spreadsheet by MATLAB. It is found in a mesh study that SOLID186 elements with initial sizes of 15 mm, 11.5 mm, and 20 mm are appropriate to mesh the parent, the avatar a1, and the avatar a2, respectively. After the gear box is meshed using the initial elements' sizes, the mesh is improved in two steps using the APDL commands shown in Listing B.1. First, the mesh of the gear box outer surface is refined except at the feet. It is expected that the feet hardly vibrate due to the clamped boundary conditions, which is applied to them. The elements sizes' can then be higher at the feet in order to reduce the number of FE nodes and, thus, calculation time. Second, the tetrahedral elements of the gear box are improved using the APDL command given by the second line in Listing B.1. Further details on the APDL commands can be found in [87].

Listing B.1: APDL commands for mesh refinement and mesh improvement

```
AREFINE, ALL, , , 1, 1, CLEAN    ! refine the mesh on selected areas
VIMP, ALL, 1, 3                  ! improve the mesh of the volume
```

The FE model used in Section 5.2.5 comprises a lumped mass m that is attached to the input flange of the parent gear box at a distance l_m, see Figure 5.22. A MASS21 element is defined and added to a TARGE170 element using a pilot node [87], see line one of Listing B.2. The TARGE170 element is then connected to the FE nodes of the input flange using CONTA174 elements, see lines two and three of Listing B.2. The contact between the TARGE170 element and the CONTA174 element is considered a *multipoint constraint*, which is recommended to model a

lumped mass [87]. Listing B.3 shows the keyoptions of the elements that define the multipoint constraint. Further details can be found in the ANSYS input file in Appendix D as well as in [87].

Listing B.2: APDL commands used to define a pilot node and add CONTA174 elements

```
TSHAP,PILO   ! define pilot node
NSLE,A,CT2   ! add contact elements
ESURF
```

Listing B.3: APDL commands used to define the keyoptions of the elements

```
! keyoptions of the MASS21 element
ET,10,MASS21     ! define element
KEYOPT,10,1,0    ! real constants are masses and rotational inertia
KEYOPT,10,2,0    ! element coordinate system parallel to global
                   coordinate system
KEYOPT,10,3,0    ! 3-D mass and rotational inertia

! keyoptions of the TARGE170 element
ET,20,170            ! define element
KEYOPT,20,2,1        ! user defined boundary conditions
KEYOPT,20,4,111111   ! multipoint constraints for all
                       degrees of freedom

! keyoptions of the CONTA174 elements
ET,30,174          ! define element
KEYOPT,30,12,5     ! contact surface always bonded
KEYOPT,30,4,2      ! rigid surface constraint
KEYOPT,30,2,2      ! multipoint constraint
```

B.4 Experimental model of the gear boxes

The gear boxes are mounted on four pneumatic springs, see Figure B.8. Each pneumatic spring is filled with air of ambient pressure, i.e., approximately $1 \cdot 10^5\,\mathrm{N\,m^{-2}}$. According to [109] the resonance frequency of the pneumatic springs yields a value $< 10\,\mathrm{Hz}$ in this case. This is much smaller than the first natural frequency of each gear box and it can be expected that the pneumatic springs hardly affect the vibration behavior of the gear boxes. Thus, the gear boxes can be considered freely suspended. The pneumatic springs are screwed to aluminum profiles that are filled with sand and that are covered with damping layers in order to reduce their vibrations. The aluminum profiles are screwed to a foundation.

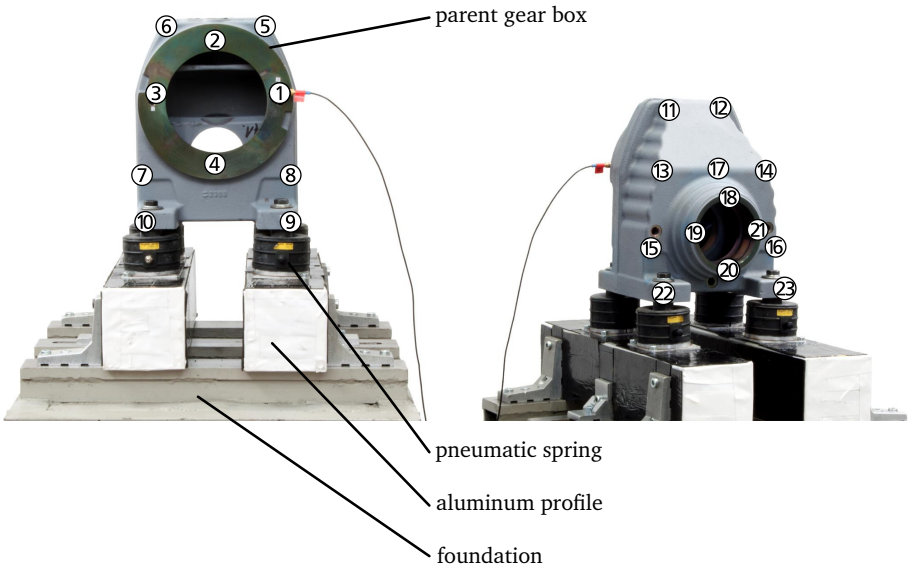

Figure B.8: test stand of the parent gear box, numbered labels refer to the measurement points listed in Table B.4

The gear boxes are excited by an impact hammer (DYTRAN 5850B) and the responses are measured by a triaxial accelerometer (DYTRAN 3093B1). Table B.4 lists the spatial locations of all measurement points, which are illustrated by the labels in Figure B.8. Note that the origin is placed in analogy to the virtual model of the gear box, see Figure 5.12. The accelerometer is placed at measurement point 1. A hammer excitation at the same spatial location of measurement point 1 is not possible. Thus, the gear boxes are excited closely above measurement point 1. However, it is not possible to excite the gear boxes at all measurement points in all three coordinate directions. Possible measurement directions are listed in Table B.4 for each measurement point. Each transfer function is measured three times and the average of these three measurements is taken. The transfer functions are sampled with 12801 samples, which leads to a frequency resolution of 1.56 Hz. The analyzed frequency ranges of the parent, avatar a1, and avatar a2 are limited to 1.5 ... 5.0 kHz, 1.9 ... 5.0 kHz, and 0.9 ... 3.6 kHz, respectively. The gear boxes are not vibrating significantly at frequencies smaller than the lower limits, while the data are noisy at frequencies higher than the upper limits due to a poor excitation by

the impact hammer. Several modal analysis algorithms are tested with different adjustments in the modal analysis software ME'SCOPE. The results are obtained from a stability diagram using an *alias free polynomial method* and a maximum model size of 80 [110].

Table B.4: spatial coordinates of the measurement points of each gear box shown in Figure B.8, all dimensions in mm

	avatar a1			parent			avatar a2			measurement
label	x	y	z	x	y	z	x	y	z	**directions**
1	62	−15	0	62	−15	0	62	−15	0	x, y
2	0	−15	62	0	−15	62	0	−15	62	y, z
3	−62	−15	0	−62	−15	0	−62	−15	0	x, y
4	0	−15	−62	0	−15	−62	0	−15	−62	y, z
5	41	0	84	41	0	84	41	0	84	x, y, z
6	−41	0	84	−41	0	84	−41	0	84	x, y, z
7	−84	0	−70	−84	0	−70	−84	0	−70	x, y
8	84	0	−70	84	0	−70	84	0	−70	x, y
9	84	−29	−96	84	−29	−96	84	−29	−96	x, y, z
10	−84	−29	−96	−84	−29	−96	−84	−29	−96	x, y, z
11	41	42	84	41	42	84	41	42	84	x, y, z
12	−41	42	84	−41	42	84	−41	42	84	x, y, z
13	61	87	13	61	87	13	61	87	13	x, y
14	−61	87	13	−61	87	13	−61	87	13	x, y
15	84	87	−70	84	87	−70	84	87	−70	x, y
16	−84	87	−70	−84	87	−70	−84	87	−70	x, y
17	0	87	13	0	87	13	0	87	13	y
18	0	105	−17	0	105	−17	0	105	−17	y, z
19	34	105	−50	34	105	−50	34	105	−50	x, y
20	0	105	−84	0	105	−84	0	105	−84	y, z
21	−34	105	−50	−34	105	−50	−34	105	−50	x, y
22	84	115	−96	84	115	−96	84	115	−96	x, y, z
23	−84	115	−96	−84	115	−96	−84	115	−96	x, y, z

C Supplemental figures and tables

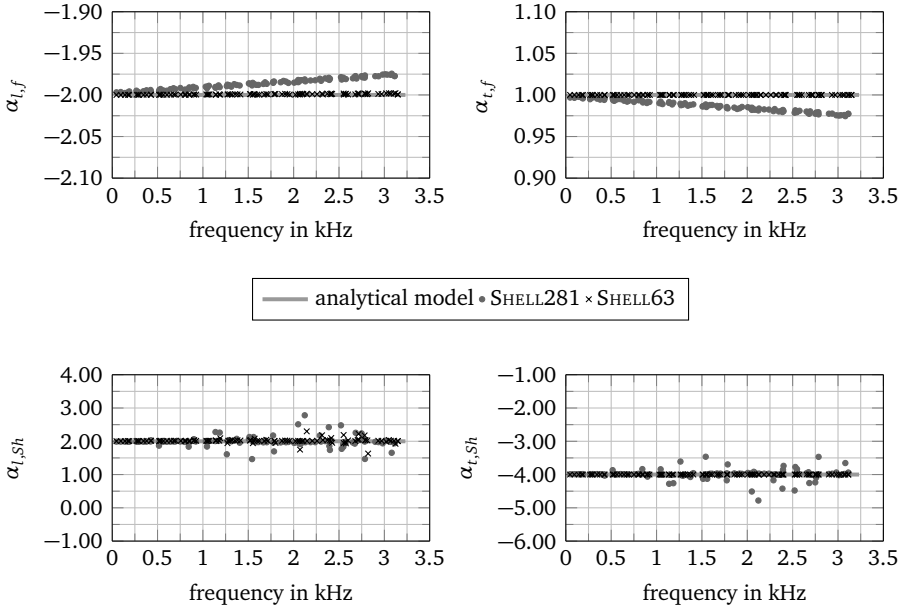

Figure C.1: powers for the scaling laws obtained from an LSA of an FE model with SHELL63 elements

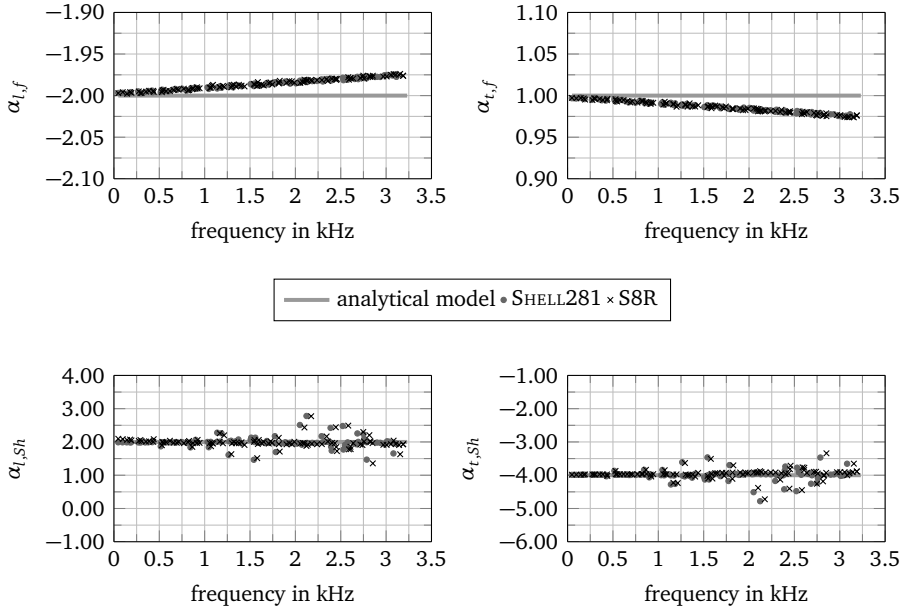

Figure C.2: powers for the scaling laws obtained from an LSA of an FE model with S8R elements

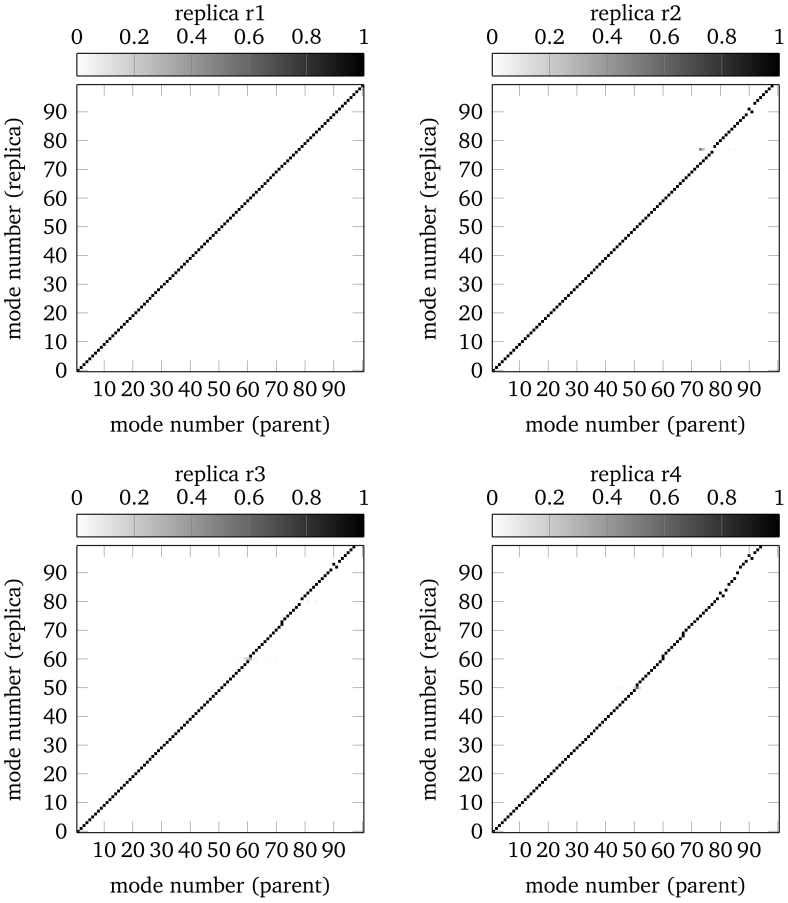

Figure C.3: MAC matrices of the replicas r1 through r4 of the rectangular plate

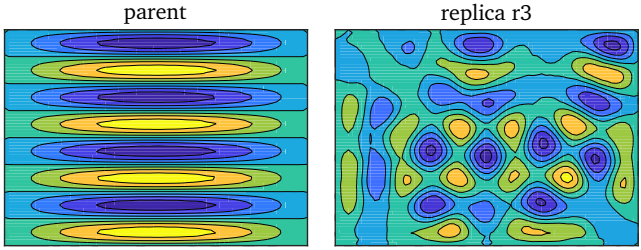

Figure C.4: 61st mode shapes of the parent and of the replica r3 (both plates are plotted in equal size for visualization purposes only)

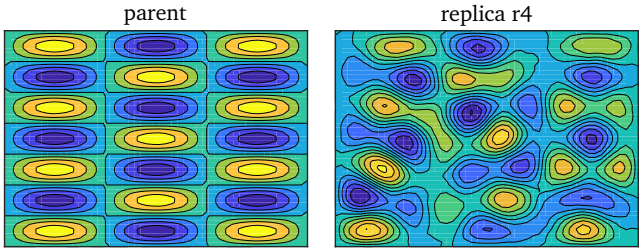

Figure C.5: 51st mode shapes of the parent and of the replica r4 (both plates are plotted in equal size for visualization purposes only)

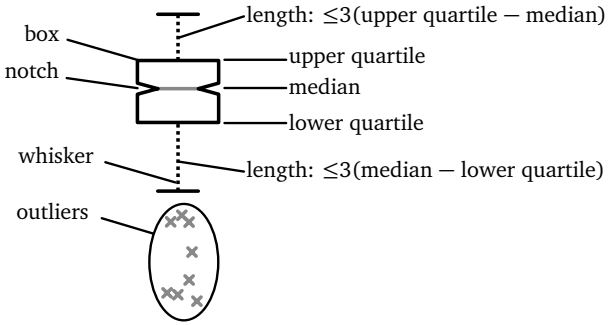

Figure C.6: description of a boxplot

Table C.1: design parameters of the replica GCU

parameter	r1	r2	r3	r4	unit
a	675.0	675.0	675.0	675.0	mm
b	735.0	735.0	735.0	735.0	mm
h	65.0	65.0	65.0	65.0	mm
t	2.0	2.0	1.0	1.0	mm
a_{1m}	85.0	85.0	85.0	85.0	mm
a_R	117.5	117.5	117.5	117.5	mm
a_{2m}	220.0	220.0	220.0	220.0	mm
a_1	273.0	273.0	273.0	273.0	mm
a_2	305.0	305.0	305.0	305.0	mm
a_3	370.0	370.0	370.0	370.0	mm
a_4	404.0	404.0	404.0	404.0	mm
a_F	587.5	587.5	587.5	587.5	mm
b_F	250.0	250.0	250.0	250.0	mm
b_R	415.0	415.0	415.0	415.0	mm
b_{1m}	540.0	540.0	540.0	540.0	mm
b_{2m}	625.0	625.0	625.0	625.0	mm
E_x	$9.76 \cdot 10^{10}$	$4.88 \cdot 10^{10}$	$9.76 \cdot 10^{10}$	$4.88 \cdot 10^{10}$	$\mathrm{N\,m^{-2}}$
E_y	$7.45 \cdot 10^{9}$	$3.73 \cdot 10^{9}$	$7.45 \cdot 10^{9}$	$3.73 \cdot 10^{9}$	$\mathrm{N\,m^{-2}}$
G_{xy}	$3.60 \cdot 10^{9}$	$1.80 \cdot 10^{9}$	$3.60 \cdot 10^{9}$	$1.80 \cdot 10^{9}$	$\mathrm{N\,m^{-2}}$
μ	0.28	0.28	0.28	0.28	–
ρ	1 372	1 981	1 372	1 981	$\mathrm{kg\,m^{-3}}$
η	0.005	0.005	0.005	0.005	–

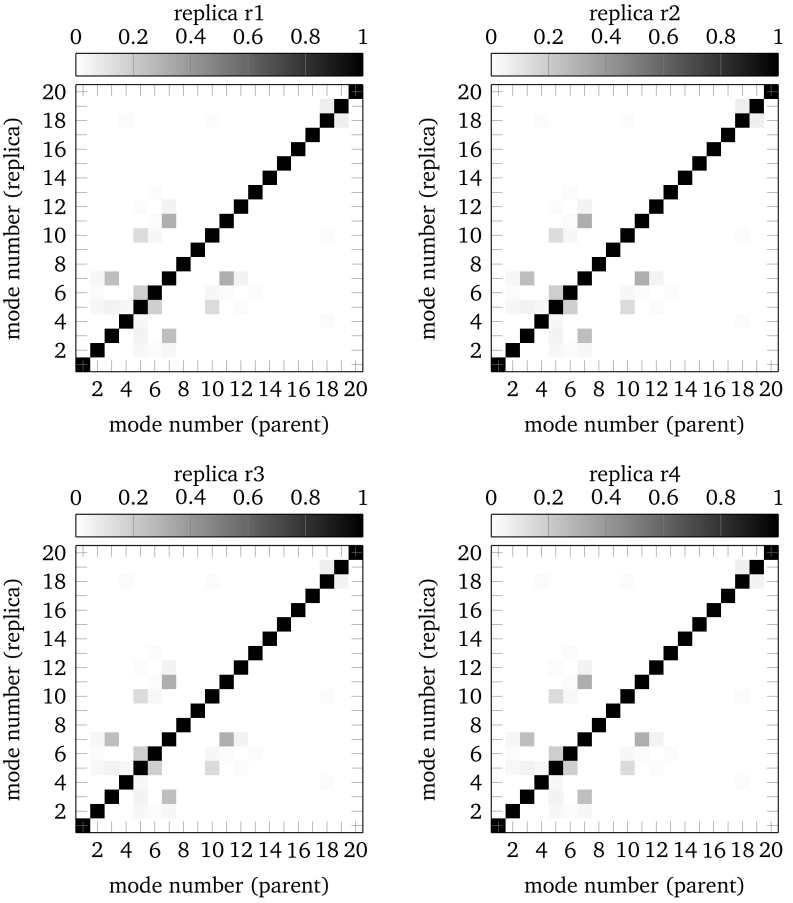

Figure C.7: MAC matrices of the replicas r1 through r4 of the GCU

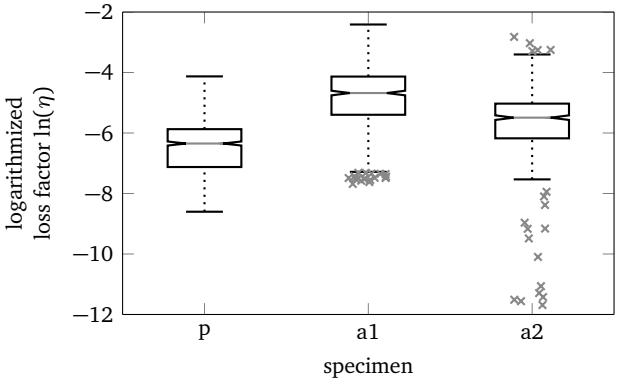

Figure C.8: boxplot of logarithmized loss factors for the parent rectangular plate as well as the avatars a1 and a2

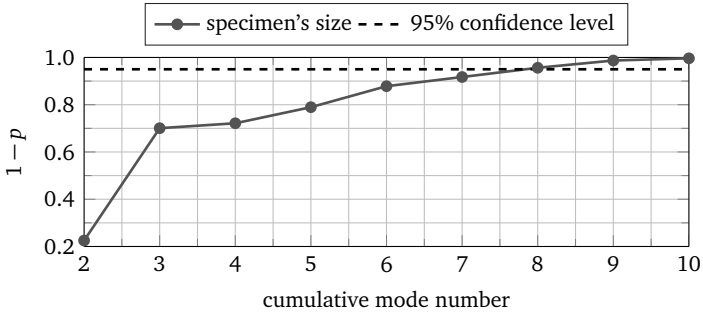

Figure C.9: $1-p$ value of the ANOVA of the modal damping versus the cumulative mode number for the avatars a1 and a2

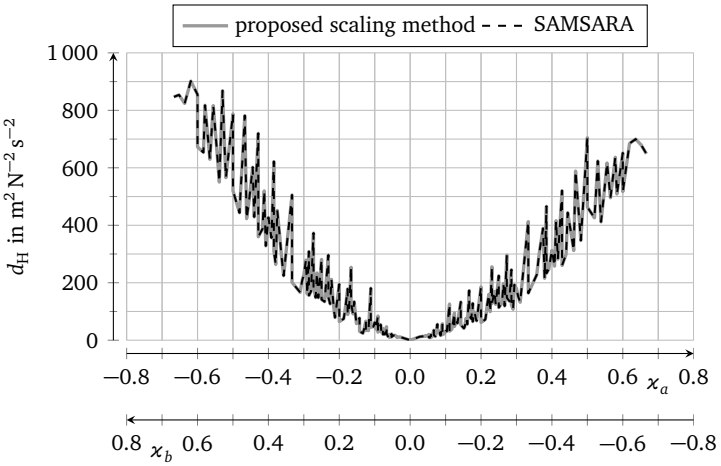

Figure C.10: HAUSDORFF distance of the driving point admittance versus the geometrical distortion

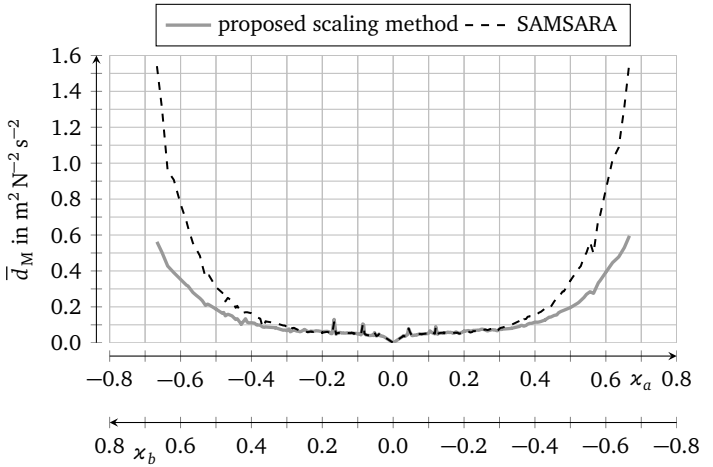

Figure C.11: mean MAHALANOBIS distance of the driving point admittance versus the geometrical distortion

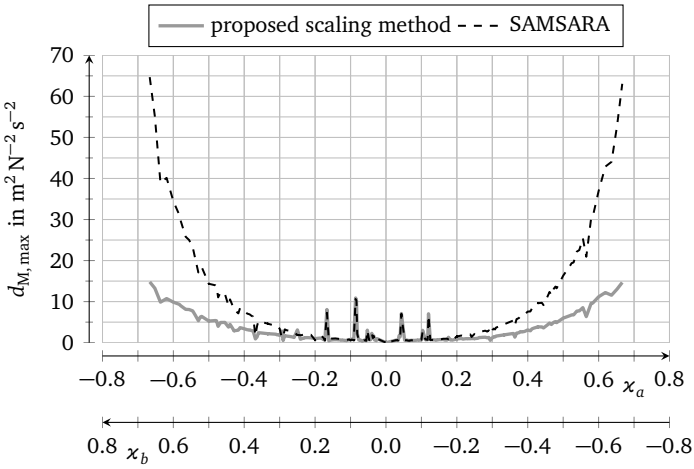

Figure C.12: maximum MAHALANOBIS distance of the driving point admittance versus the geometrical distortion

Table C.2: geometrical distortion and distance measures (in $\mathrm{m^2\,N^{-2}\,s^{-2}}$) of the driving point admittance of the avatars a1 and a2

	geometrical distortion		**proposed scaling method**			**SAMSARA**		
avatar	x_a	x_b	d_{H}	$\max(d_{\mathrm{M}})$	$\overline{d}_{\mathrm{M}}$	d_{H}	$\max(d_{\mathrm{M}})$	$\overline{d}_{\mathrm{M}}$
a1	−0.273	+0.273	372.9	1.04	0.05	372.9	0.83	0.05
a2	+0.482	−0.482	347.2	6.66	0.16	347.2	11.21	0.20

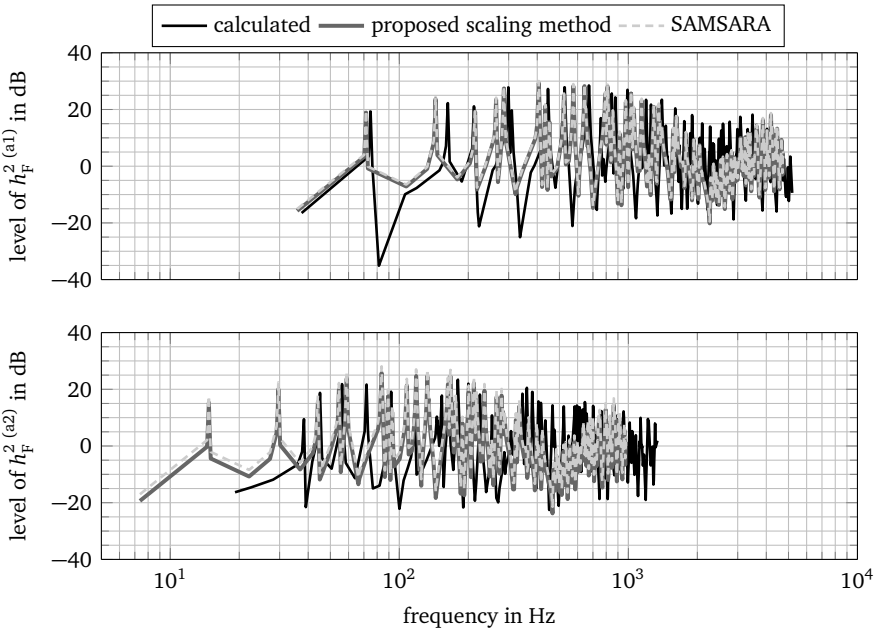

Figure C.13: level of the driving point admittance versus frequency (re $6.25 \cdot 10^{-6}\,m^2\,N^{-2}\,s^{-2}$), top: avatar a1, bottom: avatar a2

Table C.3: material properties of the rectangular plates for experimental simulations, prefix Δ denotes the measurement uncertainty, c_{long} and c_{trans} denote the speed of sound in longitudinal and transverse direction, respectively

specimen		ρ in kg m^{-3}	$\Delta\rho$ in kg m^{-3}	E in N m^{-2}	ΔE in N m^{-2}	μ	$\Delta\mu$	c_{long} in m s^{-1}	c_{trans} in m s^{-1}
parent	1	2680.36	0.32	$71.19 \cdot 10^9$	$1.66 \cdot 10^9$	0.3299	0.0081	6272	3160
	2	2671.71	0.32	$71.19 \cdot 10^9$	$1.67 \cdot 10^9$	0.3275	0.0083	6255	3168
	3	2671.76	0.32	$70.95 \cdot 10^9$	$1.65 \cdot 10^9$	0.3280	0.0082	6250	3162
replica r1	1	2672.33	0.32	$70.45 \cdot 10^9$	$1.67 \cdot 10^9$	0.3251	0.0085	6195	3154
	2	2672.32	0.32	$70.45 \cdot 10^9$	$1.67 \cdot 10^9$	0.3259	0.0085	6204	3153
	3	2673.18	0.32	$70.55 \cdot 10^9$	$1.67 \cdot 10^9$	0.3257	0.0085	6206	3155
replica r2	1	2678.50	0.45	$70.33 \cdot 10^9$	$1.66 \cdot 10^9$	0.3470	0.0071	6450	3122
	2	2678.73	0.45	$70.35 \cdot 10^9$	$1.66 \cdot 10^9$	0.3473	0.0071	6454	3122
	3	2679.29	0.45	$70.46 \cdot 10^9$	$1.67 \cdot 10^9$	0.3464	0.0072	6446	3125
avatar a1	1	2672.30	0.32	$70.26 \cdot 10^9$	$1.66 \cdot 10^9$	0.3256	0.0085	6193	3149
	2	2672.43	0.32	$70.46 \cdot 10^9$	$1.67 \cdot 10^9$	0.3251	0.0086	6196	3154
	3	2672.40	0.32	$70.73 \cdot 10^9$	$1.67 \cdot 10^9$	0.3245	0.0086	6201	3161
avatar a2	1	2678.83	0.45	$70.73 \cdot 10^9$	$1.66 \cdot 10^9$	0.3467	0.0071	6464	3131
	2	2678.85	0.45	$70.34 \cdot 10^9$	$1.66 \cdot 10^9$	0.3470	0.0071	6449	3122
	3	2678.82	0.45	$70.35 \cdot 10^9$	$1.66 \cdot 10^9$	0.3471	0.0071	6452	3122

Table C.4: geometrical design parameters (in mm) of the size range of gear boxes and scaling factors of the avatars a1 and a2, symbols of the design parameters are illustrated in Figure C.14

design parameter	**symbol**	**avatar a1**	**parent**	**avatar a2**	$\phi_j^{(a1)}$	$\phi_j^{(a2)}$
foot width	$l_{x,\mathrm{f}}$	38.50	55.00	77.00	0.70	1.40
foot length	$l_{y,\mathrm{f}}$	28.70	41.00	57.40	0.70	1.40
foot height	$l_{z,\mathrm{f}}$	17.50	25.00	35.00	0.70	1.40
foot room	$h_{z,\mathrm{f}}$	5.00	5.00	5.00	1.00	1.00
foot support length	$l_{\mathrm{f,\,supp}}$	28.00	40.00	56.00	0.70	1.40
flange length	$l_{y,\mathrm{fl}}$	15.60	13.00	14.95	1.20	1.15
flange inner diameter	$d_{\mathrm{fl,\,i}}$	104.00	130.00	195.00	0.80	1.50
flange outer diameter	$d_{\mathrm{fl,\,o}}$	144.00	180.00	270.00	0.80	1.50
top width 1	$l_{x,\mathrm{top},1}$	82.60	118.00	165.20	0.70	1.40
top width 2	$l_{x,\mathrm{top},2}$	70.00	100.00	140.00	0.70	1.40
top length 1	$l_{y,\mathrm{top},1}$	24.15	34.50	48.30	0.70	1.40
top length 2	$l_{y,\mathrm{top},2}$	41.76	46.40	78.88	0.90	1.70
top height	$l_{z,\mathrm{top}}$	84.00	105.00	157.50	0.80	1.50
bottom width	$l_{x,\mathrm{bottom}}$	168.00	210.00	336.00	0.80	1.60
bottom length	$l_{y,\mathrm{bottom}}$	86.40	108.00	151.20	0.80	1.40
bottom height	$l_{z,\mathrm{bottom}}$	113.40	162.00	226.80	0.70	1.40
length	l_y	105.00	150.00	210.00	0.70	1.40
wall thickness	t	5.40	6.00	7.20	0.90	1.20
inner wall offset	$l_{y,\mathrm{wall}}$	40.00	40.00	92.00	1.00	2.30
inner wall height	$l_{z,\mathrm{wall}}$	98.00	140.00	196.00	0.70	1.40
inner wall thickness	t_{wall}	14.00	20.00	28.00	0.70	1.40
inner wall gap height	$l_{z,\mathrm{wall,\,gap}}$	15.75	22.50	31.50	0.70	1.40
inner wall diameter	d_{wall}	50.40	72.00	100.80	0.70	1.40
inner plate length	$l_{y,\mathrm{plate}}$	21.00	30.00	42.00	0.70	1.40
inner plate height	$l_{z,\mathrm{plate}}$	32.25	43.00	77.40	0.75	1.80
inner plate thickness	t_{plate}	6.00	6.00	6.00	1.00	1.00
shaft height	$l_{z,\mathrm{shaft}}$	63.00	90.00	126.00	0.70	1.40
cone diameter 1	$d_{\mathrm{cone},1}$	107.10	153.00	214.20	0.70	1.40
cone diameter 2	$d_{\mathrm{cone},2}$	72.10	103.00	144.20	0.70	1.40
cone diameter 3	$d_{\mathrm{cone},3}$	63.00	90.00	126.00	0.70	1.40

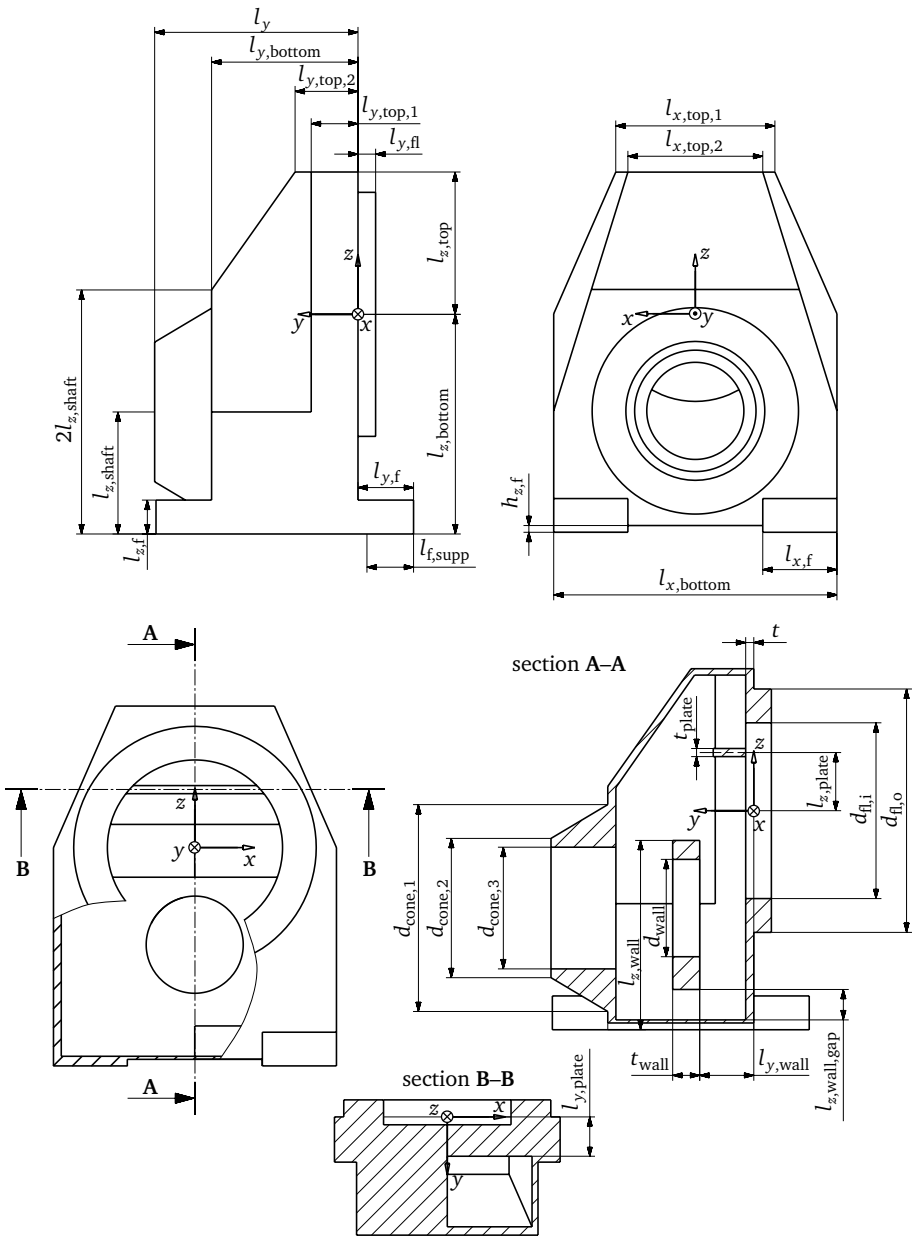

Figure C.14: sketches of the parent gear box, symbols according to Table C.4

Table C.5: sensitivities α_{X_j,f_n} of the distorted design parameters of the parent gear box

f_n	$h_{z,\mathrm{f}}$	$l_{y,\mathrm{fl}}$	$d_{\mathrm{fl,i}}$	$d_{\mathrm{fl,o}}$	$l_{z,\mathrm{top}}$	$l_{y,\mathrm{top},2}$
f_1	−0.0041	−0.0699	0.0929	−0.2485	−0.3374	−0.0419
f_2	−0.0177	−0.0669	−0.3232	−0.1413	−0.3212	−0.0388
f_3	−0.0297	0.0237	0.2599	0.4534	−0.0428	−0.0079
f_4	−0.0148	−0.0062	−0.0148	0.0130	−0.1874	−0.0308
f_5	−0.0153	−0.0375	−0.2463	−0.0217	−0.1508	−0.0063
f_6	−0.0070	−0.0346	−0.3091	−0.0321	−0.2372	−0.0186
f_7	−0.0016	−0.0238	−1.2175	−0.0116	−0.2656	−0.0395
f_8	−0.0539	0.0167	−0.0867	0.0628	−0.1452	−0.0096
f_9	−0.0095	−0.0180	−0.1805	−0.0513	−0.1388	−0.0236
f_{10}	−0.0160	0.0018	−0.0293	0.0548	−0.0877	−0.0061
f_{11}	−0.0251	−0.0121	−0.1650	−0.0253	−0.3173	−0.0467
f_{12}	−0.0140	0.0826	−0.0999	0.2237	−0.1252	−0.0169
f_{13}	−0.0307	−0.0005	−0.0919	0.0098	−0.2273	0.0259
f_{14}	−0.0118	0.0497	−0.1082	0.1010	−0.3913	0.1250
f_{15}	−0.0039	0.0072	−0.1400	0.0036	−0.1425	−0.0025
f_{16}	0.0215	−0.0095	−0.0900	−0.0483	−0.2838	−0.0164
f_{17}	−0.0200	−0.0046	−0.0677	0.0209	−0.4638	0.0455
f_{18}	0.0046	−0.0174	−0.2093	0.0047	−0.1476	−0.0134
f_{19}	−0.0106	−0.0145	−0.0651	−0.0123	−0.1991	−0.0196
f_{20}	−0.0029	−0.0235	−0.1615	−0.0458	−0.2428	0.0629

f_n	$l_{x,\mathrm{bottom}}$	$l_{y,\mathrm{bottom}}$	t	$l_{y,\mathrm{wall}}$	$l_{z,\mathrm{plate}}$	t_{plate}
f_1	−0.4930	0.7781	0.2293	−0.0259	−0.0123	−0.0297
f_2	0.6447	−0.1235	0.1073	−0.0278	0.0030	−0.0355
f_3	−1.6165	−0.0074	0.8316	−0.0489	−0.0504	0.0032
f_4	−1.3797	0.2212	0.5108	−0.0144	−0.0136	0.0100
f_5	−0.5533	0.2491	0.3577	−0.0064	0.0709	0.0227
f_6	−0.6868	0.1928	0.4284	0.0072	0.1311	0.0722
f_7	−0.5180	−0.1799	0.3603	0.0148	0.6947	0.4884
f_8	−0.4440	−0.2594	0.4374	−0.0092	−0.0019	0.0177
f_9	−0.7702	−0.0467	0.2878	−0.0022	0.0776	0.0853
f_{10}	−1.1802	0.3641	0.6975	0.0559	0.0325	0.0271
f_{11}	−0.9091	0.0829	0.3751	0.0089	0.0636	0.0386
f_{12}	−1.3856	0.0663	0.4707	−0.0576	−0.0017	0.0000
f_{13}	−1.1127	0.0987	0.5284	0.0179	0.0849	0.0492
f_{14}	−0.7079	−0.3029	0.4462	−0.0055	0.1545	0.0667
f_{15}	−0.7260	−0.3738	0.3786	0.0264	−0.0007	0.0142
f_{16}	−0.7776	−0.5764	0.6114	0.0460	0.0039	0.0459
f_{17}	−0.6083	−0.2955	0.4364	−0.0032	0.1691	0.0502
f_{18}	−0.5187	−0.3076	0.2957	0.0266	0.0210	0.0144
f_{19}	−0.5514	−0.3810	0.2762	−0.0030	−0.0471	0.0419
f_{20}	−0.5912	−0.1078	0.2878	−0.0053	0.0501	0.0032

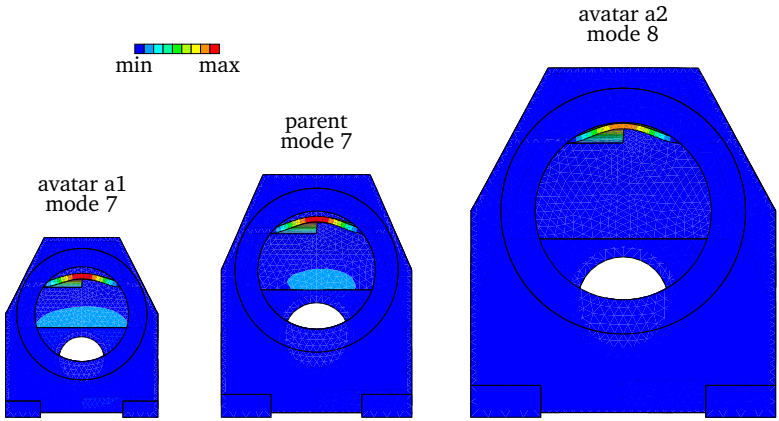

Figure C.15: mode shapes 7 of the parent and of the avatar a1 gear box as well as mode shape 8 of the avatar a2 gear box. Each mode shape is scaled with respect to its maximum.

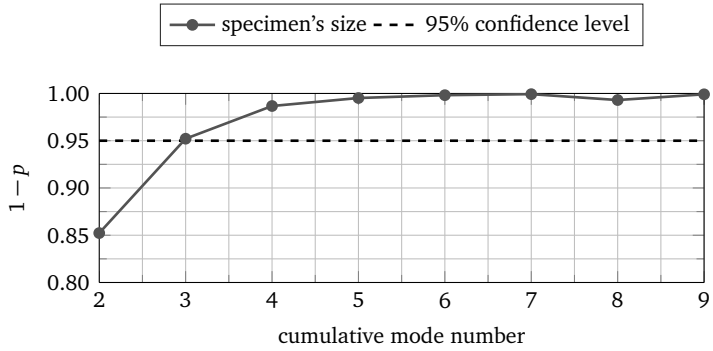

Figure C.16: $1 - p$ value of the ANOVA of the modal damping versus the cumulative mode number for the avatar gear boxes a1 and a2

Table C.6: actual scaling factors ϕ_{f_i} of the measured natural frequencies and their mean value $\overline{\phi}_f$

	ϕ_{f_i}									
avatar	1	2	3	4	5	6	7	8	9	$\overline{\phi}_f$
a1	1.32	1.45	1.33	1.51	1.36	–	–	1.32	1.36	1.38
a2	0.60	0.66	–	0.57	–	0.63	0.67	0.64	0.76	0.64

Table C.7: summary of scaling laws derived, verified, and validated in this thesis

structure	**model**	**boundary condition**	**scaling factor**	**vibration response**
rectangular plate	analytical	*SSSS*	ϕ_a, ϕ_b, ϕ_t	$f_{m,n}$, Sh_{T}^2
	FE	*SSSS*, *FFFF*, *CFFF*, *CCCC*	ϕ_a, ϕ_b, ϕ_t, ϕ_F	$f_{m,n}$, Sh_{T}^2, $\overline{\tilde{v}^2}$, h_{F}^2
	experimental	*SSSS*	ϕ_a, ϕ_b, ϕ_t	$f_{m,n}$, Sh_{T}^2
GCU	FE	*FFFF*	ϕ_l, ϕ_t, ϕ_E, ϕ_ρ	f_n, h_{F}^2, v_{R}
size range of gear boxes	FE	feet clamped	ϕ_l, ϕ_m	f_n
	experimental	feet free	ϕ_l	f_n

D Digital appendix

This appendix provides scripts and macros of the virtual models used in this thesis as well as animated mode shapes of the size range of gear boxes. All scripts and macros have been exclusively used with the hardware platform and software listed in Tables B.1 through B.3. Operation on other hardware platforms and/or software releases cannot be guaranteed. The digital appendix contains:

- virtual models
  - rectangular plate, analytical model and FE model
  - generic car undercarriage, FE model
  - parent gear box, FE model
- mode shapes of the size range of gear boxes
  - mode shapes of the avatar a1
  - mode shapes of the parent
  - mode shapes of the avatar a2

Download the digital appendix from:
`https://tuprints.ulb.tu-darmstadt.de/id/eprint/8726`

List of figures

List of tables

List of abbreviations

ANOVA	analysis of variance
ASMA	asymptotic scaled modal analysis
CCCC	clamped boundary conditions
CFFF	cantilevered boundary conditions
DA	dimensional analysis
EDA	energy distribution approach
FE	finite elements
FEM	finite element method
FFFF	free boundary conditions
GCU	generic car undercarriage
GSA	global sensitivity analysis
LSA	local sensitivity analysis
MAC	modal assurance criterion
MSTA	mean squared transfer admittance
RMS	root mean square
SA	sensitivity analysis
SAMple	System reliability, Adaptive structures, and Machine acoustics test stand for primary laboratory experiments
SAMSARA	similitude and asymptotic models for structural-acoustic research and applications
SI	International System of Units
SLDV	scanning laser DOPPLER vibrometer
SSSS	simply supported boundary conditions
STAGE	similitude theory applied to governing equations
2-DoF	two degrees of freedom
a1, a2, ...	avatar 1, avatar 2, ...
p	parent
r1, r2, ...	replica 1, replica 2, ...

List of symbols

Each symbol is explained, its unit is given based on the International System of Units (SI), and its dimension is given in terms of the fundamental dimensions mass, length, and time, i.e., as a linear combination of M, L, and T. Dimensionless quantities are denoted by "1" and "–" denotes an unspecified unit or dimension.

Latin letters

$\mathbf{A}$	data set A	–	–
B	flexural stiffness of a plate	N m	$\mathsf{ML}^2\mathsf{T}^{-2}$
$\mathbf{B}$	data set B	–	–
$\mathbf{D}$	damping matrix	$\mathrm{kg\,s^{-1}}$	MT^{-1}
E	YOUNG'S modulus	$\mathrm{N\,m^{-2}}$	$\mathsf{ML}^{-1}\mathsf{T}^{-2}$
F	dynamic force	N	MLT^{-2}
$\hat{F}$	force magnitude	N	MLT^{-2}
$\mathbf{F}$	load vector	N	MLT^{-2}
$\hat{\mathbf{F}}$	vector of force magnitudes	N	MLT^{-2}
G_{xy}	shear modulus	$\mathrm{N\,m^{-2}}$	$\mathsf{ML}^{-1}\mathsf{T}^{-2}$
$H_{j,\mathrm{modal}}$	j-th modal transfer function	$\mathrm{N^{-1}\,m^{-1}}$	$\mathsf{M}^{-1}\mathsf{L}^{-2}\mathsf{T}^{2}$
$\mathbf{H}_{\mathrm{modal}}$	matrix of modal transfer functions	$\mathrm{N^{-1}\,m^{-1}}$	$\mathsf{M}^{-1}\mathsf{L}^{-2}\mathsf{T}^{2}$
I	rotational inertia	$\mathrm{kg\,m^2}$	ML^2
K	number of fundamental dimensions	1	1
$\mathbf{K}$	stiffness matrix	$\mathrm{N\,m^{-1}}$	MT^{-2}
ΔL	level difference in dB	–	–
M	number of responses	1	1
MAC	modal assurance criterion	1	1
$\mathbf{M}$	mass matrix	kg	M
N	number (in general), number of design parameters	1	1
N_{sample}	number of samples	1	1
P	sound power	W	$\mathsf{ML}^2\mathsf{T}^{-3}$
Q	physical quantity	–	–

$\mathbf{Q}$	matrix of eigenvectors	m	L
R^2_{adj}	adjusted coefficient of determination	1	1
S	surface area	m^2	L^2
SS	sum of squares	–	–
$S_{j,k}$	first order sensitivity	–	–
Sh^2_{T}	mean squared transfer admittance	$\text{m}^4\,\text{N}^{-2}\,\text{s}^{-2}$	$\text{M}^{-2}\text{L}^2\text{T}^2$
U	eigenvector of displacements	m	L
X	design parameter	–	–
$\mathbf{X}$	set of design parameters	–	–
Y	response	–	–
$\mathbf{Y}$	set of responses	–	–
a	length in x-direction	m	L
b	length in y-direction	m	L
c	wave propagation speed	$\text{m}\,\text{s}^{-1}$	LT^{-1}
d	damping	$\text{kg}\,\text{s}^{-1}$	MT^{-1}
d	diameter	m	L
d_{E}	EUCLIDEAN distance	–	–
d_{H}	HAUSDORFF distance	–	–
d_{M}	MAHALANOBIS distance	–	–
e	2.71828…, EULER'S number	1	1
f	(natural) frequency	Hz	T^{-1}
$\mathbf{f}$	external load vector	$\text{N}\,\text{kg}^{-1}$	LT^{-2}
$\mathfrak{f}$	general functional	–	–
Δf	3-dB bandwidth	Hz	T^{-1}
h	length in z-direction	m	L
h^2_{F}	driving point admittance	$\text{m}^2\,\text{N}^{-2}\,\text{s}^{-2}$	M^{-2}T^2
i	imaginary unit, $\text{i}^2 = -1$	1	1
k	stiffness	$\text{N}\,\text{m}^{-1}$	MT^{-2}
l	length	m	L
m	mass	kg	M
m_{A}	additional mass	kg	M
p	probability	1	1
r	PEARSON'S correlation coefficient	1	1
s	standard deviation	–	–
t	thickness	m	L
u	displacement	m	L
$\hat{u}$	amplitude coefficient of displacement	m	L

$\mathbf{u}$	vector of displacements	m	L
$\hat{\mathbf{u}}$	vector of displacement amplitudes	m	L
v	velocity	$\mathrm{m\,s^{-1}}$	LT^{-1}
$\overline{\tilde{v}^2}$	surface-averaged squared RMS velocity	$\mathrm{m^2\,s^{-2}}$	$\mathsf{L}^2\mathsf{T}^{-2}$
x	spatial coordinate	m	L
y	spatial coordinate	m	L
z	spatial coordinate	m	L

Greek letters

Δ	LAPLACE operator	1	1
Π	dimensionless product	1	1
$\mathbf{\Sigma}$	covariance matrix	1	1
Ω	angular excitation frequency	$\mathrm{s^{-1}}$	T^{-1}
α	power (exponent)	1	1
β	regression coefficient	–	–
δ	stiffness multiplier of the damping	s	T
ε	error of the regression model	–	–
ε_f	error of the natural frequencies	1	1
η	material loss factor	1	1
$\varkappa$	geometrical distortion	1	1
μ	POISSON's ratio	1	1
ξ	thickness ratio	1	1
π	3.14159…, ARCHIMEDES' number	1	1
ρ	mass density	$\mathrm{kg\,m^{-3}}$	ML^{-3}
σ	radiation efficiency	1	1
τ	time	s	T
ϕ	scaling factor	1	1
ψ	mode shape	m	L
ω	(natural) angular frequency	$\mathrm{s^{-1}}$	T^{-1}

Subscripts

F	force
FE	calculated by means of FE
R	receiver point
Sh	mean squared transfer admittance
SL	replicated by means of scaling laws
a	air
b	bounded quantity
bl	blade
bottom	bottom side of the gear box
cone	truncated cone of the gear box
f	free quantity, foot of the gear box
f	(fundamental) frequency
fl	flange of the gear box
gap	gap of the inner wall of the gear box
i	inner
i	integer index
j	integer index, index of design parameters
k	integer index, index of responses
l	length or transverse, integer index
long	longitudinal
m	number of half-waves in x-direction, mass
max	maximum
min	minimum
modal	modal quantity
n	number of half-waves in y-direction, mode number
o	outer
plate	inner plate of the gear box
res	residual
shaft	shaft of the gear box
supp	support of the gear box
top	top side of the gear box
tot	total
trans	transverse
wall	inner wall of the gear box
x	x-direction
y	y-direction

z	z-direction
0	interception, level reference value
φ	rotational direction

Superscripts

H	HERMITIAN
T	transpose
(a)	avatar
(p)	parent
(r)	replica
$(+)$	scale up (during LSA)
$(-)$	scale down (during LSA)
$(\cdot)'$	transformed quantity

Bibliography

English translations of titles in German language are given in parentheses. They have been translated by the author of this thesis.

[1] G. Pahl and W. Beitz. Baureihenentwicklung (Development of size ranges). *Konstruktion*, 26:71–79, 1974.

[2] G. Pahl and W. Beitz. Baureihenentwicklung (Fortsetzung) (Development of size ranges (continued)). *Konstruktion*, 26:113–118, 1974.

[3] G. Pahl, W. Beitz, J. Feldhusen, and K.H. Grote. Size Ranges and Modular Products. In K. Wallace and L. Blessing, editors, *Engineering Design – A Systematic Approach*, chapter 9. Springer, London, 2007.

[4] W.E. Baker, P.S. Westine, and F.T. Dodge. *Similarity Methods in Engineering Dynamics: Theory and Practice of Scale Modeling*. Elsevier, Amsterdam, rev. edition, 1991.

[5] A. Saltelli, K. Chan, and E.M. Scott. *Sensitivity Analysis*. John Wiley & Sons, Chichester, 2008.

[6] G. Murphy. *Similitude in Engineering*. Ronald Press, New York, 1950.

[7] R. Rosen. *Life Itself – A Comprehensive Inquiry into the Nature, Origin, and Fabrication of Life*. Columbia University Press, New York, 1991.

[8] L. Cremer, M. Heckl, and B.A.T. Petersson. *Structure-Borne Sound: Structural Vibrations and Sound Radiation at Audio Frequencies*. Springer, Berlin, 3rd edition, 2005.

[9] F.G. Kollmann, T.F. Schösser, and R. Angert. *Praktische Maschinenakustik (Applied Machine Acoustics)*. Springer, Berlin, 2006.

[10] O.C. Zienkiewicz, R.L. Taylor, and J.Z. Zhu. *The Finite Element Method: Its Basis and Fundamentals*. Elsevier, Oxford, 7th edition, 2013.

[11] G. Kirchhoff. Über das Gleichgewicht und die Bewegung einer elastischen Scheibe (On the equilibrium and the motion of an elastic plate). *Journal für die reine und angewandte Mathematik*, 40:51–88, 1850.

[12] A.E.H. Love. XVI. The small free vibrations and deformation of a thin elastic shell. *Philosophical Transactions of the Royal Society of London A: Mathematical, Physical and Engineering Sciences*, 179:491–546, 1888.

[13] R.D. Mindlin. Influence of rotary inertia and shear on flexural motions of isotropic, elastic plates. *Journal of Applied Mechanics*, 18(1):31–38, 1951.

[14] E. Reissner. The effect of transverse shear deformation on the bending of elastic plates. *Journal of Applied Mechanics*, 12(2):A69–A77, 1945.

[15] A.W. Leissa. *Vibration of Plates*. National Aeronautics and Space Administration, Washington, D.C., 1969.

[16] H. Hanselka and J. Bös. Maschinenakustik (Machine Acoustics). In K.H. Grote and J. Feldhusen, editors, *Dubbel – Taschenbuch für den Maschinenbau (Dubbel – Handbook of Mechanical Engineering)*, chapter O3, pages O30–O41. Springer, Berlin, 24th edition, 2014.

[17] D.A. Bies, C.H. Hansen, and C.Q. Howard. *Engineering Noise Control*. Taylor & Francis Group, Boca Raton, 5th edition, 2018.

[18] S.J. Elliott. Radiation modes and the active control of sound power. *The Journal of the Acoustical Society of America*, 94(4):2194–2204, 1993.

[19] E. Buckingham. On physically similar systems; Illustrations of the use of dimensional equations. *Physical Review*, 4(4):345–376, 1914.

[20] H.L. Langhaar. *Dimensional Analysis and Theory of Models*. John Wiley & Sons, New York, 1951.

[21] S. De Rosa, F. Franco, and T. Polito. Structural similitudes for the dynamic response of plates and assemblies of plates. *Mechanical Systems and Signal Processing*, 25(3):969–980, 2011.

[22] S. De Rosa, F. Franco, and V. Meruane. Similitudes for the structural response of flexural plates. *Proceedings of the Institution of Mechanical Engineers, Part C: Journal of Mechanical Engineering Science*, 230(2): 174–188, 2016.

[23] J. Pawlowski. *Die Ähnlichkeitstheorie in der physikalisch-technischen Forschung – Grundlagen und Anwendungen (The Similitude Theory in Physical-Technical Research – Fundamentals and Applications)*. Springer, Berlin, 1971.

[24] B. Zohuri. *Dimensional Analysis and Self-Similarity Methods for Engineers and Scientists*. Springer, New York, 2017.

[25] S.J. Kline. *Similitude and Approximation Theory*. Springer, Berlin, 1986.

[26] C.P. Coutinho, A.J. Baptista, and J. Dias Rodrigues. Reduced scale models based on similitude theory: A review up to 2015. *Engineering Structures*, 119:81–94, 2016.

[27] J.W. Wissmann. Dynamic stability of space vehicles – Structural dynamics model testing. Technical Report CR-1195, National Aeronautics and Space Administration, Washington, D.C., 1968.

[28] J.J. Wu, M.P. Cartmell, and A.R. Whittaker. Prediction of the vibration characteristics of a full-size structure from those of a scale model. *Computers & Structures*, 80:1461–1472, 2002.

[29] M.S. Williams and A. Blakeborough. Laboratory testing of structures under dynamic loads: An introductory review. *Philosophical Transactions of the Royal Society A: Mathematical, Physical and Engineering Sciences*, 359(1786):1651–1669, 2001.

[30] B. Kittirungsi, H.K. Fathy, and J.L. Stein. An efficient scaling methodology for dynamic models using dimensional and activity analyses. In *Proceedings of IMECE 2006 – ASME International Mechanical Engineering Congress and Exposition*, Chicago, Illinois, USA, November 5–10, 2006.

[31] W. Soedel. Similitude approximations for vibrating thin shells. *The Journal of the Acoustical Society of America*, 49(5):1535–1541, 1971.

[32] J.J. Wu. The complete-similitude scale models for predicting the vibration characteristics of the elastically restrained flat plates subjected to dynamic loads. *Journal of Sound and Vibration*, 268(5):1041–1053, 2003.

[33] J.J. Wu. Dynamic analysis of a rectangular plate under a moving line load using scale beams and scaling laws. *Computers & Structures*, 83 (19–20):1646–1658, 2005.

[34] J.J. Wu. Prediction of the dynamic characteristics of an elastically supported full-size flat plate from those of its complete-similitude scale model. *Computers & Structures*, 84(3–4):102–114, 2006.

[35] G.J. Simitses and J. Rezaeepazhand. Structural similitude for laminated structures. *Composites Engineering*, 3(7–8):751–765, 1993.

[36] J. Rezaeepazhand and G.J. Simitses. Use of scaled-down models for predicting vibration response of laminated plates. *Composite Structures*, 30(4):419–426, 1995.

[37] J. Rezaeepazhand and G.J. Simitses. Design of scaled down models for predicting shell vibration response. *Journal of Sound and Vibration*, 195 (2):301–311, 1996.

[38] L. Cheng and C. Lesueur. Preliminary study on vibroacoustic model scaling of a structure coupled to an acoustic cavity. *Journal d'Acoustique*, 3:349–359, 1990.

[39] S. Torkamani, H.M. Navazi, A.A. Jafari, and M. Bagheri. Structural similitude in free vibration of orthogonally stiffened cylindrical shells. *Thin-Walled Structures*, 47(11):1316–1330, 2009.

[40] P. Singhatanadgid and A.N. Songkhla. An experimental investigation into the use of scaling laws for predicting vibration responses of rectangular thin plates. *Journal of Sound and Vibration*, 311(1–2):314–327, 2008.

[41] Z. Xiaojian, A. Bangcheng, L. Ziqiang, and L. Dun. A scaling procedure for panel vibro-acoustic response induced by turbulent boundary layer. *Journal of Sound and Vibration*, 380:165–179, 2016.

[42] W. Weber. *Akustische Modellgesetze für die Schalleistung von Getriebebaureihen (Scaling Laws for the Sound Power of a Size Range of Gear Boxes)*. PhD thesis, Technische Hochschule Darmstadt, 1987.

[43] K.G. Heyne. Akustische Ähnlichkeit hydrostatischer Axialkolbenpumpen der Schrägachsenbauart (Acoustic similitude of hydrostatic axial piston pumps of bent axis design). *ölhydraulik und pneumatik*, 23(8):572–577, 1979.

[44] K.G. Heyne. Neuere Ergebnisse zur akustischen Ähnlichkeit von Axialkolbenpumpen (Newer results of acoustic similitude of axial piston pumps). *ölhydraulik und pneumatik*, 24(5):376–380, 1980.

[45] T. Sueki and T. Kitagawa. Evaluation of rolling and impact noise due to rail joints using the scale-model testing. In *Inter-Noise 2017*, Hong Kong, China, August 27–30, 2017.

[46] D.W. Herrin, G. Cheng, S.C. Campbell, and J.M. Stencel. Noise reduction on a jumbo drill using panel contribution analysis and scale modeling. In *Inter-Noise 2017*, Hong Kong, China, August 27–30, 2017.

[47] F.J. Fahy. Some applications of the reciprocity principle in experimental vibroacoustics. *Acoustical Physics*, 49(2):217–229, 2003.

[48] J. Guo, X. Yan, Y. Chen, S. Lu, G. Ma, and X. Hu. A scale model test of high-speed railway channel girder for noise reduction. In *Inter-Noise 2017*, Hong Kong, China, August 27–30, 2017.

[49] Y. Chen, X. Yan, X. Hu, G. Ma, J. Guo, W. Hu, and S. Lu. Experimental study of airborne noise reduction of concrete channel girder bridge sections compared with box girder for high-speed trains. *Acta Acustica united with Acustica*, 104(6):970–983, 2018.

[50] K. Ruan and D.W. Herrin. Using scale modeling to assess heating and air conditioning duct attenuation. In *Inter-Noise 2017*, Hong Kong, China, August 27–30, 2017.

[51] S. De Rosa and F. Franco. A scaling procedure for the response of an isolated system with high modal overlap factor. *Mechanical Systems and Signal Processing*, 22(7):1549–1565, 2008.

[52] S. De Rosa and F. Franco. On the use of the asymptotic scaled modal analysis for time-harmonic structural analysis and for the prediction of coupling loss factors for similar systems. *Mechanical Systems and Signal Processing*, 24(2):455–480, 2010.

[53] S. De Rosa, F. Franco, X. Li, and T. Polito. A similitude for structural acoustic enclosures. *Mechanical Systems and Signal Processing*, 30:330–342, 2012.

[54] S. De Rosa and F. Franco. Analytical similitudes applied to thin cylindrical shells. *Advances in Aircraft and Spacecraft Science*, 2(4):403–425, 2015.

[55] S. De Rosa, F. Franco, and T. Polito. Partial scaling of finite element models for the analysis of the coupling between short and long structural wavelengths. *Mechanical Systems and Signal Processing*, 52–53:722–740, 2015.

[56] B. Mace. Statistical energy analysis, energy distribution models and system modes. *Journal of Sound and Vibration*, 264(2):391–409, 2003.

[57] V. Meruane, S. De Rosa, and F. Franco. Numerical and experimental results for the frequency response of plates in similitude. *Proceedings of the Institution of Mechanical Engineers, Part C: Journal of Mechanical Engineering Science*, 230(18):3212–3221, 2016.

[58] G. Petrone, M. Manfredonia, S. De Rosa, and F. Franco. Structural similitudes of stiffened cylinders. *Mathematics and Mechanics of Solids (OnlineFirst)*, 2017.

[59] O. Robin, S. De Rosa, and A. Berry. Similitudes for the structural response and radiated power from plates. In *Inter-Noise 2016*, Hamburg, Germany, August 21–24, 2016.

[60] O. Robin, F. Franco, S. De Rosa, E. Ciappi, and A. Berry. Scaling laws for flat plate vibroacoustic response induced by deterministic and random excitations. In *6th NOVEM – Noise and Vibration Emerging Methods*, Ibiza, Spain, May 07–09, 2018.

[61] D.P. Huttenlocher, G.A. Klanderman, and W.J. Rucklidge. Comparing images using the Hausdorff distance. *IEEE Transactions on Pattern Analysis and Machine Intelligence*, 15(9):850–863, 1993.

[62] K.K. Choi and N.H. Kim. *Structural Sensitivity Analysis and Optimization 1: Linear Systems*. Springer, New York, 2005.

[63] D.C. Montgomery. *Design and Analysis of Experiments*. John Wiley & Sons, Hoboken, 7th edition, 2009.

[64] K.K. Choi and N.H. Kim. *Structural Sensitivity Analysis and Optimization 2: Nonlinear Systems and Applications*. Springer, New York, 2005.

[65] F. van Keulen, R.T. Haftka, and N.H. Kim. Review of options for structural design sensitivity analysis. Part 1: Linear systems. *Computer Methods in Applied Mechanics and Engineering*, 194(30–33):3213–3243, 2005.

[66] H.M. Adelman and R.T. Haftka. Sensitivity analysis of discrete structural systems. *AIAA Journal*, 24(5):823–832, 1986.

[67] K.K. Choi, I. Shim, and S. Wang. Design sensitivity analysis of structure-induced noise and vibration. *Journal of Vibration and Acoustics*, 119(2): 173–179, 1997.

[68] N.H. Kim, J. Dong, K.K. Choi, N. Vlahopoulos, Z.D. Ma, M.P. Castanier, and C. Pierre. Design sensitivity analysis for sequential structural-acoustic problems. *Journal of Sound and Vibration*, 263(3):569–591, 2003.

[69] C. Yang and D.E. Adams. Predicting changes in vibration behavior with respect to multiple variables using empirical sensitivity functions. *Journal of Vibration and Acoustics*, 132(6):061004, 2010.

[70] M.A. Kramer, H. Rabitz, and J.M. Calo. Parametric scaling of mathematical models. *Applied Mathematical Modelling*, 8(5):341–350, 1984.

[71] L.A. Eslava, L. Eno, and H. Rabitz. Further developments and applications of sensitivity analysis to collisional energy transfer. *The Journal of Chemical Physics*, 73(10):4998–5012, 1980.

[72] J.H. Halton. On the efficiency of certain quasi-random sequences of points in evaluating multi-dimensional integrals. *Numerische Mathematik*, 2:84–90, 1960.

[73] I.M. Sobol'. On the distribution of points in a cube and the approximate evaluation of integrals. *USSR Computational Mathematics and Mathematical Physics*, 7(4):86–112, 1967.

[74] Soong-Oh Han. *Varianzbasierte Sensitivitätsanalyse als Beitrag zur Bewertung der Zuverlässigkeit adaptronischer Struktursysteme (Variance-based Sensitivity Analysis as Contribution to the Assessment of the Reliability of Smart Structural Systems)*. PhD thesis, Technische Universität Darmstadt, 2011.

[75] C. Adams, J. Bös, E.M. Slomski, and T. Melz. Comparison of sampling techniques for global sensitivity analyses of scaled vibrating structures. In *Inter-Noise 2017*, Hong Kong, China, August 27–30, 2017.

[76] T. Most and J. Will. Sensitivity analysis using the metamodel of optimal prognosis. In *Weimar Optimization and Stochastic Days 2011*, Weimar, Germany, November 24–25, 2011.

[77] N. Kleinfeller. *Entwicklung von Maßnahmen zur Verringerung des Körperschalltransfers von Maschinenstrukturen (Development of measures to reduce the structure-borne sound transfer of machine structures)*. Master's thesis, Technische Universität Darmstadt, Darmstadt, Germany, 2017.

[78] C. Adams, J. Bös, and T. Melz. A scaling method for vibrating structures using global sensitivity analysis. In *Inter-Noise 2016*, Hamburg, Germany, August 21–24, 2016.

[79] Y. Zhu, Y. Wang, Z. Luo, Q. Han, and D. Wang. Similitude design for the vibration problems of plates and shells: A review. *Frontiers of Mechanical Engineering*, 12(2):253–264, 2017.

[80] Z. Luo, Y. Zhu, X. Zhao, and D. Wang. Determination method of dynamic distorted scaling laws and applicable structure size intervals of a rotating thin-wall short cylindrical shell. *Proceedings of the Institution of Mechanical Engineers, Part C: Journal of Mechanical Engineering Science*, 229(5): 806–817, 2015.

[81] Z. Luo, Y. Zhu, X. Zhao, and D. Wang. Determining dynamic scaling laws of geometrically distorted scaled models of a cantilever plate. *Journal of Engineering Mechanics*, 142(4):04015108, 2016.

[82] D.J. Inman. *Engineering Vibration*. Pearson, London, 4th edition, 2014.

[83] P. Bratley and B.L. Fox. Algorithm 659: Implementing Sobol's quasirandom sequence generator. *ACM Transactions on Mathematical Software*, 14(1):88–100, 1988.

[84] S. Joe and F.Y. Kuo. Remark on algorithm 659: Implementing Sobol's quasirandom sequence generator. *ACM Transactions on Mathematical Software*, 29(1):49–57, 2003.

[85] C. Adams, J. Bös, E.M. Slomski, and T. Melz. Scaling laws obtained from a sensitivity analysis and applied to thin vibrating structures. *Mechanical Systems and Signal Processing*, 110:590–610, 2018.

[86] R.G. Grimes, J.G. Lewis, and H.D. Simon. A shifted Block Lanczos algorithm for solving sparse symmetric generalized eigenproblems. *SIAM Journal on Matrix Analysis and Applications*, 15(1):228–272, 1996.

[87] ANSYS 15.0 Documentation, Mechanical APDL, 2013.

[88] DIN 45630 Physical and Subjective Magnitudes of Sound, 1971. Standard.

[89] ABAQUS 6.13 – Documentation, 2013.

[90] R.J. Allemang. The modal assurance criterion – twenty years of use and abuse. *Sound and Vibration*, 1(August):14–21, 2003.

[91] C. Adams, J. Bös, and T. Melz. An experimental investigation of vibrating plates in similitude and the possibility to replicate the responses using sensitivity-based scaling laws. In *6th NOVEM – Noise and Vibration Emerging Methods*, Ibiza, Spain, May 07–09, 2018.

[92] O. Robin, J.D. Chazot, R. Boulandet, M. Michau, A. Berry, and N. Atalla. A plane and thin panel with representative simply supported boundary conditions for laboratory vibroacoustic tests. *Acta Acustica united with Acustica*, 102(1):170–182, 2016.

[93] P. Langer, K. Sepahvand, C. Guist, J. Bär, A. Peplow, and S. Marburg. Matching experimental and three dimensional numerical models for structural vibration problems with uncertainties. *Journal of Sound and Vibration*, 417:294–305, 2018.

[94] D.J. Ewins. *Modal Testing: Theory, Practice and Application*. Research Studies Press, Baldock, 2nd edition, 2000.

[95] C. Adams, J. Bös, and T. Melz. A benchmark case for structural intensity calculations. In *DAGA 2017 – 43rd annual Conference on Acoustics*, Kiel, Germany, March 06–09, 2017.

[96] H. Schürmann. *Konstruieren mit Faser-Kunststoff-Verbunden (Designing with Fiber Reinforced Plastics)*. Springer, Berlin, 2005.

[97] K.K.U. Stellbrink. *Micromechanics of Composites*. Hanser Publishers, Munich, 1996.

[98] P.C. Mahalanobis. On the generalized distance in statistics. *Proceedings of the National Institute of Sciences of India*, 2(1):49–55, 1936.

[99] SEW-EURODRIVE GmbH & Co KG. Gearmotors, Frequency Inverters, Drive Automation, 2019. URL `https://www.sew-eurodrive.de`. Last accessed on June 05, 2019.

[100] G. Maidanik. Response of ribbed panels to reverberant acoustic fields. *The Journal of the Acoustical Society of America*, 34(6):809–826, 1962.

[101] S. Oberst. Nonlinear dynamics: Towards a paradigm change via evidence-based complex dynamics modelling. In *6th NOVEM – Noise and Vibration Emerging Methods*, Ibiza, Spain, May 07–09, 2018.

[102] H. Kantz and T. Schreiber. *Nonlinear Time Series Analysis*. Cambridge University Press, Cambridge, 2nd edition, 2003.

[103] M. Schmidt and H. Lipson. Distilling free-form natural laws from experimental data. *Science*, 324(5923):81–85, 2009.

[104] S.L. Brunton, J.L. Proctor, and J.N. Kutz. Discovering governing equations from data by sparse identification of nonlinear dynamical systems. *Proceedings of the National Academy of Sciences of the United States of America*, 113(15):3932–3937, 2016.

[105] R. Markert. *Strukturdynamik (Structural Dynamics)*. Technische Universität Darmstadt, Darmstadt, 2010.

[106] H. Lohninger. Grundlagen der Statistik, Mahalanobis-Distanz (Fundamentals of Statistics, Mahalanobis Distance), 2019. URL http://www.statistics4u.info. Last accessed on June 05, 2019.

[107] P. Langer, M. Maeder, C. Guist, M. Krause, and S. Marburg. More than six elements per wavelength: The practical use of structural finite element models and their accuracy in comparison with experimental results. *Journal of Computational Acoustics*, 25:1750025, 2017.

[108] C. Adams, J. Bös, and T. Melz. Experimentelle Untersuchung der Ähnlichkeit skalierter Plattenstrukturen (Experimental investigation of the similitude of plates). In *DAGA 2018 – 44th annual Conference on Acoustics*, Munich, Germany, March 19–22, 2018.

[109] Effbe Levelmount Machine Supports, SLM Series, 2019. URL https://www.effbe.de. Last accessed on June 05, 2019.

[110] ME'scope VES Help, 2018.